Technische Universität München
TUM School of Natural Sciences

Photonic graph state generation from individual atoms in an optical cavity

René Philip Thomas

Vollständiger Abdruck der von der TUM School of Natural Sciences der Technischen Universität München zur Erlangung eines

Doktors der Naturwissenschaften (Dr. rer. nat.)

genehmigten Dissertation.

Vorsitz:		Prof. Dr. Michael Knap
Prüfende der Dissertation :	1.	Hon.-Prof. Dr. Gerhard Rempe
	2.	Prof. Dr. Andreas Reiserer

Die Dissertation wurde am 10.07.2024 bei der Technischen Universität München eingereicht und durch die TUM School of Natural Sciences am 30.10.2024 angenommen.

Abstract

Graph states are a class of multipartite entangled states that can be expressed using a concise graphical notation. They serve as an essential resource for measurement-based quantum information processing. Due to the extensive arsenal of experimental tools available for manipulating and measuring light, optical photons are ideally suited for measurement-based protocols. However, the absence of interaction between photons poses a challenge in entangling photons experimentally. The traditional approach, relying on spontaneous parametric down-conversion, is inherently probabilistic and therefore highly inefficient in practice. This imposes severe constraints on scalability, even for moderate numbers of qubits.

Here, we circumvent this limitation by using individual rubidium atoms trapped in an optical cavity as efficient single-photon sources. In a first experiment, we implement a protocol for graph-state generation employing a single atom. We combine the photon emission mechanism with the internal degrees of freedom of the atom to realise atom-photon entanglement. An alternating sequence of photon emissions and atomic qubit rotations results in long strings of entangled photons. We are able to produce Greenberger-Horne-Zeilinger states of up to 14 photons and linear cluster states of up to 12 photons, while demonstrating genuine multipartite entanglement. Thanks to a source-to-detection efficiency approaching 50%, our generation scheme shows a clear scaling advantage over the probabilistic schemes based on nonlinear optics.

In a second step, we show that these states can be merged into larger states with more complex topologies. By exploiting two-photon interference in the cavity mode, we implement a heralded atom-atom gate operation, which we call 'cavity-assisted fusion gate'. We then combine the previously developed single-emitter protocols with this fusion gate to fuse graph states generated independently by two different atoms. This allows us to generate ring and tree graph states consisting of up to eight qubits. The fusion of photonic graph states represents a crucial step towards the creation of graph states with arbitrary connectivity. These would provide access to a wide spectrum of measurement-based quantum computation and communication protocols, including one-way quantum computation or the one-way quantum repeater.

List of publications

- A Quantum-Logic Gate Between Distant Quantum-Network Modules
  S. Daiss, S. Langenfeld, S. Welte, E. Distante, P. Thomas, L. Hartung, O. Morin, G. Rempe
  Science **371**, 614-617 (2021)

- Quantum Teleportation between Remote Qubit Memories with Only a Single Photon as a Resource
  S. Langenfeld, S. Welte, L. Hartung, S. Daiss, P. Thomas, O. Morin, E. Distante, G. Rempe
  Phys. Rev. Lett. **126**, 130502 (2021)

- Quantum Repeater Node Demonstrating Unconditionally Secure Key Distribution
  S. Langenfeld, P. Thomas, O. Morin, G. Rempe
  Phys. Rev. Lett. **126**, 230506 (2021)

- Detecting an Itinerant Optical Photon Twice without Destroying It
  E. Distante, S. Daiss, S. Langenfeld, L. Hartung, P. Thomas, O. Morin, G. Rempe, S. Welte
  Phys. Rev. Lett. **126**, 253603 (2021)

- A Nondestructive Bell-State Measurement on Two Distant Atomic Qubits
  S. Welte, P. Thomas, L. Hartung, S. Daiss, S. Langenfeld, O. Morin, G. Rempe, E. Distante
  Nature Photonics **15**, 504-509 (2021)

- Efficient Generation of Entangled Multiphoton Graph States from a Single Atom
  P. Thomas, L. Ruscio, O. Morin, G. Rempe
  Nature **608**, 677–681 (2022)

- Fusion of Deterministically Generated Photonic Graph States
  P. Thomas, L. Ruscio, O. Morin, G. Rempe
  Nature **629**, 567–572 (2024)

Contents

1. Introduction

The early days of quantum physics

The development of quantum mechanics revolutionised the understanding of nature, but also gave rise to a plethora of technologies still in use today. Its discovery began in the early part of the 20th century at a time in which prominent figures such as Max Planck, Albert Einstein, Niels Bohr, Werner Heisenberg, and Erwin Schrödinger played pivotal roles within and beyond the physics community. The foundations of this theory were laid in 1900 by Planck's groundbreaking work on black-body radiation [1]. He proposed that the walls of a black body absorb and emit radiation in small portions of energy, which he simply referred to as 'energy elements'. This radically new idea arose more out of necessity within the mathematical framework rather than from physical intuition. However, Einstein expanded upon this concept and employed it to explain the photoelectric effect [2], an experimental observation that defied explanation within Maxwell's theory of electromagnetic radiation. He suggested that electromagnetic radiation itself consists of discrete 'light quanta'. Both Planck and Einstein later received the Nobel prize in physics for what can be regarded as the discovery of the photon.

These groundbreaking works marked the onset of a paradigm shift in the physics community. Given the well-established wave-like behaviour of light, physicists were now compelled to reconcile the simultaneous existence of wave and particle-like characteristics, a concept that became known as wave-particle duality. Quantum theory also decisively influenced the understanding of the structure of matter. In 1913, Niels Bohr developed a model describing electron orbitals in atoms [3]. He proposed that electrons move around the nucleus in discrete orbitals with quantised angular momentum. The success of his model lies in the fact that it partly explains the spectral emission properties of hydrogen. In 1924, Louis de Broglie recognised that the concept of wave-particle duality also extended to matter [4], which had previously been solely associated with particle-like properties. Remarkably, his theory reproduced the condition of angular momentum quantisation in Bohr's model in terms of a periodic boundary condition for the electron wave. The wave mechanics developed by de Broglie would foreshadow the work of Erwin Schrödinger, who in 1926 published his famous wave equation for matter particles [5], known as the Schrödinger equation. It describes the behaviour of small objects in terms of their wave function and stands as one of, if not the most important equation in quantum mechanics.

The EPR paradox and Bell's theorem

From the outset, the development of quantum mechanics was marked by intense debates, whose protagonists were often reluctant to abandon the trusted beliefs of classical physics. One of the quantum phenomena that perhaps most strikingly defies classical intuition is the concept of entanglement. Quantum mechanics allows two particles, denoted as A and B, to be in a state that can only be adequately described by a shared wave function. Particles A and B are then said to be 'entangled'. Constructed around this scenario, Einstein, Podolsky and Rosen (EPR) put forward their famous *Gedankenexperiment* [6].

In their paper published in 1935 they claimed to expose an inconsistency in the wave function description of nature, thus questioning the completeness of quantum mechanics. Based on his belief in the locality principle inherent in special relativity, Einstein further argued that a measurement on particle A could not instantaneously affect the properties of particle B at a distance, an idea famously encapsulated by his quote 'spooky action at a distance'.

Other sceptics shared his concerns about the perceived incompleteness of quantum theory. Some, including Einstein himself, attempted to formulate an alternative description of nature that avoided the probabilistic predictions of quantum mechanics by introducing what came to be known as 'hidden variables'. The debate persisted until the 1960s when John Bell proved that a local hidden-variable theory is mathematically incompatible with the predictions of quantum mechanics [7]. His theorem, which included the famous Bell inequality, provided a framework that would allow to directly test the subject at hand in an experiment. However, at the time such experiments sparked, from today's perspective, surprisingly little interest in the physics community. Only a hand full of experimentalists were interested in the experiment proposed by Bell. The first so-called 'Bell test' that violated Bell's inequality was carried out by John Clauser in 1972 [8]. His efforts were followed by Alain Aspect about a decade later. His experimental results [9–11] showed a violation of Bell's inequality with a higher statistical significance while also closing some of the loopholes that were present in Clauser's experiment. In the following decades more experiments were performed that relied on even fewer assumptions than the first implementations [12–14]. Eventually, a loophole-free violation of Bell's inequality was demonstrated in several experiments between 2015 and now [15–20]. Today a local hidden-variable theory is widely considered to be ruled out by experimental observations.

The advent of quantum information processing

Beyond their implications for the fundamental understanding of nature, quantum mechanical phenomena such as entanglement were eventually recognised as a resource for potentially useful technological applications. One of the first to consider the possibility of harnessing the principles of quantum mechanics for computation was Richard Feynman, who suggested that a quantum mechanical system could be simulated more efficiently using hardware that exhibits quantum mechanical behaviour [21]. The first quantum algorithms were developed in the 1990s, for example the Deutsch algorithm [22], the Shor algorithm [23, 24] or Grover's algorithm [25]. It was shown that these algorithms exhibit a quantum advantage over classical algorithms, for instance in prime factorisation. Meanwhile, it was discovered that quantum mechanical principles could improve the security of information exchange between two parties. In 1984, Charles Bennett and Gilles Brassard developed an encryption protocol [26] based on encoding information in a single photon. They showed that their protocol would allow to establish a key in such a way that an eavesdropper could be detected thanks to the no-cloning theorem [27], marking the beginning of quantum key distribution (QKD). Artur Ekert devised a protocol in 1991 that explicitly relies on entangled pairs of particles to establish a key and Bell's theorem to ensure the absence of an eavesdropper [28].

The union of quantum mechanics and information science had emerged as a fascinating area of research, known as quantum information processing (QIP). Yet the suitable physical platform for implementing these ideas in practice was not immediately clear. The necessary hardware would need to enable precise control over individual quantum systems. The years in which the field of QIP was established saw significant advances in experimental atomic

physics. In the early 1980s, driven by the development of laser cooling, researchers were able to trap and observe single ions in free space [29, 30]. Subsequently, methods for cooling and trapping of neutral atoms were also developed [31–34]. Amongst these techniques, the magneto-optical trap (MOT), invented by Jean Dalibard, became a cornerstone of atomic physics thanks to its effectiveness and ease of operation. The toolbox of laser cooling eventually became so advanced that it enabled the preparation of a single ion in different quantum states of motion [35]. These experiments belong to the achievements that earned Dave Wineland the Nobel prize in 2012 for the manipulation of quantum systems [36].

The other half of the prize was awarded to Serge Haroche, whose experimental work shared a fascinating link with Wineland's, albeit with a twist in the roles played by light and matter [37]. Rather than controlling matter particles with classical light, he trapped single photons in a high-finesse optical resonator and probed their quantum state with a beam of Rydberg atoms [38, 39]. Related work was conducted by Herbert Walther at the Max Planck Institute of Quantum Optics (MPQ) [40, 41]. These experiments decisively shaped the field of cavity quantum electrodynamics (cavity QED), as they were the first to observe single atoms strongly interacting with single photons. At the same time, they beautifully demonstrated the existence of photons beyond the photoelectric effect. While the initial implementations of this kind were performed in the microwave domain, the concept was soon transposed to the optical regime [42]. In the first optical cavity setups, atoms traversed the resonator, similar to the microwave experiments. Several years later it became feasible to trap and cool atoms at the centre of the cavity, while maintaining strong atom-cavity coupling [43–47].

These developments took on a fresh perspective in the context of QIP. Cirac and Zoller introduced the concept of using cold ions confined in a linear trap as quantum bits (qubits) for quantum computation [48], an idea that was further developed by Møllmer and Sørensen [49]. Briegel and Raussendorf built upon earlier developments in QKD [26, 28] and proposed the quantum repeater [50]. Their idea makes use of stationary qubits connected through photons travelling along optical links, highlighting the necessity for efficient light-matter interfaces. The goal of creating such interfaces naturally drew inspiration from the methods developed in cavity QED. This laid the groundwork for the inception of quantum networks, heralding a new era of quantum-enabled communication and computation [51].

Graph state entanglement

The principles of QIP promote quantum entanglement as one of the driving forces behind the various algorithms and protocols. In many instances, two-partite entanglement in the form of the well-known Bell states is sufficient for implementing specific protocols, such as establishing a communication link between two parties. In other cases, the entanglement extends over multiple particles, in which the mathematical description becomes much more involved. A special class of entangled states known as graph states [52, 53] provides a formalism in which the quantum state of multiple qubits can be concisely represented in a graphical notation. These graph states are represented as graphs consisting of vertices and edges, where each vertex symbolises a qubit and the edges denote the entanglement relationships between them. An example, called two-dimensional (2D) cluster state, is shown in Fig. 1.1. Remarkably, this particular graph state serves as a universal resource for a special kind of quantum computation [54]. Here, the computational programme is defined by a sequence of single-qubit measurements on the constituents of the state. This protocol called one-way quantum computation or measurement-based quantum computa-

tion (MBQC) eliminates the need for two-qubit gates, instead placing greater emphasis on the preparation of the initial resource state. The principle of measurement-based processing of quantum information also extends into the realm of quantum communication, with protocols like the all-photonic quantum repeater [55, 56] or the one-way quantum repeater [57].

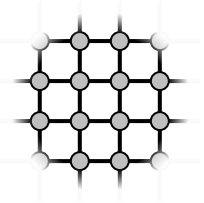

Figure 1.1: Graph states. The vertices (circles) represent individual qubits, whereas the connection between them define the entanglement topology. The specific example shown is known as a two-dimensional (2D) cluster state.

Regarding the choice of qubit carrier, several advantages speak in favour of optical photons. First, the commercially developed optics for lasers, such as waveplates and beam splitters, provide a well-established toolbox for manipulating photonic qubits. Second, single-qubit addressability, a recurring problem in most quantum computing architectures, is intrinsically guaranteed if the photons are prepared in well-separated temporal modes. Finally, optical photons are practically the only viable candidate for measurement-based quantum communication protocols. Their weak interaction with the environment and minimal decoherence make them ideal for long-distance quantum communication applications. For these reasons, a growing research community aims to develop photon sources capable of generating multi-qubit states of entangled photons.

The quest to harness entangled photons for quantum information applications began in the late 1980s [58]. Initially, the primary experimental method for generating multiphoton entanglement relied on spontaneous parametric down-conversion (SPDC). This phenomenon occurs in nonlinear crystals that are pumped with a pulsed laser. In the SPDC process, a single pump photon undergoes conversion into a pair of polarisation-entangled photons at a different wavelength. Over time, the SPDC scheme evolved into a robust and reliable source of entangled photon pairs that operates in the room temperature range. A number of important proof-of-concept experiments were conducted to showcase the power of entanglement in the context of quantum information science [59–64].

A critical drawback of SPDC lies in its probabilistic generation process. Alongside the desired pairs of single photons, the crystal also produces an unwanted vacuum contribution, double pairs and higher-order components. The proportion of these components varies with the intensity of the pump power. Lowering the intensity of the pump laser can suppress the undesired multiphoton events that degrade the entanglement fidelity. However, this also entails a lower probability to obtain the desired single-photon pairs. Consequently, a compromise between success probability and fidelity has to be found. Typically, this trade-off is chosen at a mean photon number of $\bar{n} \approx 0.1$ per output pulse. This turns out to be particularly costly for states involving many qubits, as the effective coincidence rate exponentially decays as a function of qubit number N.

Due to this fundamental limitation, a different approach has attracted increasing interest in the research community. The basic idea consists of using a matter qubit as efficient single-photon source with its spin acting as an ancillary degree-of-freedom that entangles the emitted photons [65–67]. The first experimental implementation of this concept employed quantum dots [68], but in principle any spin system with a light-matter interface, such as colour centres in diamond, trapped ions or neutral atoms, could serve as the emitter qubit. The advantage of this technique lies in the intrinsically single-photon-like emission of quantum two-level systems. Here, the generation efficiency is not subject to a trade-off

with fidelity and can be increased by engineering the light-matter coupling with optical cavities or nanostructures. In fact, experimental demonstrations have shown single-photon efficiencies exceeding 50%, while maintaining high purity and indistinguishability [69–72]. This is already at the level of loss-tolerance thresholds of certain quantum computing architectures [73–75].

Graph state generation using cavity QED

This thesis reports on a series of experiments that represent a significant contribution to the development of a universal source for arbitrary photonic graph states. We achieve this by using single rubidium atoms trapped in an optical cavity, allowing us to efficiently prepare various types of graph states. The key results can be subdivided into two parts.

In a first set of experiments, we use a single emitter to generate two elementary types of graph states, namely Greenberger-Horne-Zeilinger (GHZ) states and one-dimensional (1D) cluster states. Notably, we produce a photonic state with a record number of 14 photons, exhibiting genuine multipartite entanglement. In the second part, we add a second atom and leverage the combined capabilities of the two emitter qubits through a process known as photonic fusion. The latter is a special type of two-qubit quantum-logic operation that effectively merges the graph states emitted by the individual atoms. As a result, we are able to demonstrate more complex types of graph states with ring and tree-like topologies. The photonic fusion and the generation of graph states from the individual atoms represent the critical ingredients for tailoring graph states of arbitrary connectivity.

The text is structured as follows: Chapter 2 introduces the apparatus of our cavity QED experiment as it currently operates in the laboratory. Along with the most critical components of the setup, we introduce elementary protocols that serve as building blocks for graph state generation. In chapter 3 we explain the concept of graph states and the theory behind it. Chapter 4 describes the first set of experiments demonstrating graph state generation from a single atom. This principle is extended to two atoms in chapter 5, where we demonstrate the concept of fusion to prepare ring and tree graph states. Chapter 6 gives a summary of the experiments carried out and a projection into the future. This includes follow-up experiments and possibilities for scaling up the presented strategy.

2. An atomic cavity QED experiment

Since 1999, the 'Quantum Dynamics' division at the Max Planck Institute of Quantum Optics has been researching light-matter interaction in the context of cavity QED. Several laboratories investigate this topic using rubidium atoms that couple to a high-finesse optical cavity. This system allows to induce strong coupling between single atoms and single photons, which is difficult to achieve in free space. Within the quantum information processing (QIP) subsection of our division, our goal is to apply this principle to the field of quantum communication and computation.

The experiments described in this thesis focus on the efficient generation of multipartite entangled states of photons. The work was carried out on a setup that was built by PhD student Jörg Bochmann about 15 years ago [76]. Internally, we call it the 'Pistol' experiment since its original purpose was to 'shoot' single photons on demand, at the push of a button. Its design is strongly based on its twin setup, the 'QGate' experiment, to ensure compatibility in the context of quantum network experiments [77, 78].

This chapter describes the experimental tools required for photonic entanglement generation using our cavity QED setup. We will start with the experimental apparatus of the Pistol experiment, whose core component is the optical cavity acting as an efficient light-matter interface. In the second part we will discuss some elementary experimental techniques and sequences. These will to some extent serve as the building blocks for the protocols developed in the experimental chapters 4 and 5.

2.1. Experimental setup

The experimental setup comprises a sophisticated assembly of electronics, vacuum parts, lasers and optical components. In particular, the optical setup plays a vital role in atom trapping, cooling, optical pumping and state manipulation. We will start with an overview of the main optical table.

2.1.1. Overview

The main experiment is mounted on a 180 cm × 120 cm optical table and consists of a vacuum chamber in its centre and a complex configuration of optical components used for optical manipulation of the atoms. An overview can be seen in Fig. 2.1. Although this sketch contains the main elements of the setup, it is a simplified representation and does not reflect its full complexity.

The vacuum chamber in the centre contains the optical cavity and forms the heart of the experiment. To trap atoms, we use a two-dimensional (2D) optical lattice potential consisting of a 1064 nm and a 772 nm laser, propagating along the x- and y-directions, respectively. The 1064 nm laser traverses the vacuum chamber and is retro-reflected to form a standing wave. The 772 nm laser is coupled into the cavity mode and, in addition to providing confinement, serves as a frequency reference to stabilise the length of the cavity. A second laser at 1064 nm is used to transfer the atoms from a magneto-optical trap (MOT) to the cavity centre. We cool the atoms in the optical trapping potential via Sisyphus cooling on the D_2 line of rubidium. An imaging system comprising an optical

objective and a camera (not shown in Fig. 2.1) allows to spatially resolve the position of the atoms in the trap. Two Raman pairs operating at 790 nm and 795 nm enable coherent manipulation of the atomic state. Photons can be emitted into the cavity mode employing the vacuum-stimulated Raman adiabatic passage (vSTIRAP) mechanism. They are outcoupled predominantly through one of the two cavity mirrors. The single photons are then coupled into an optical fibre and sent to a detection setup for polarisation analysis. The different components of the setup are described in more detail in the following sections.

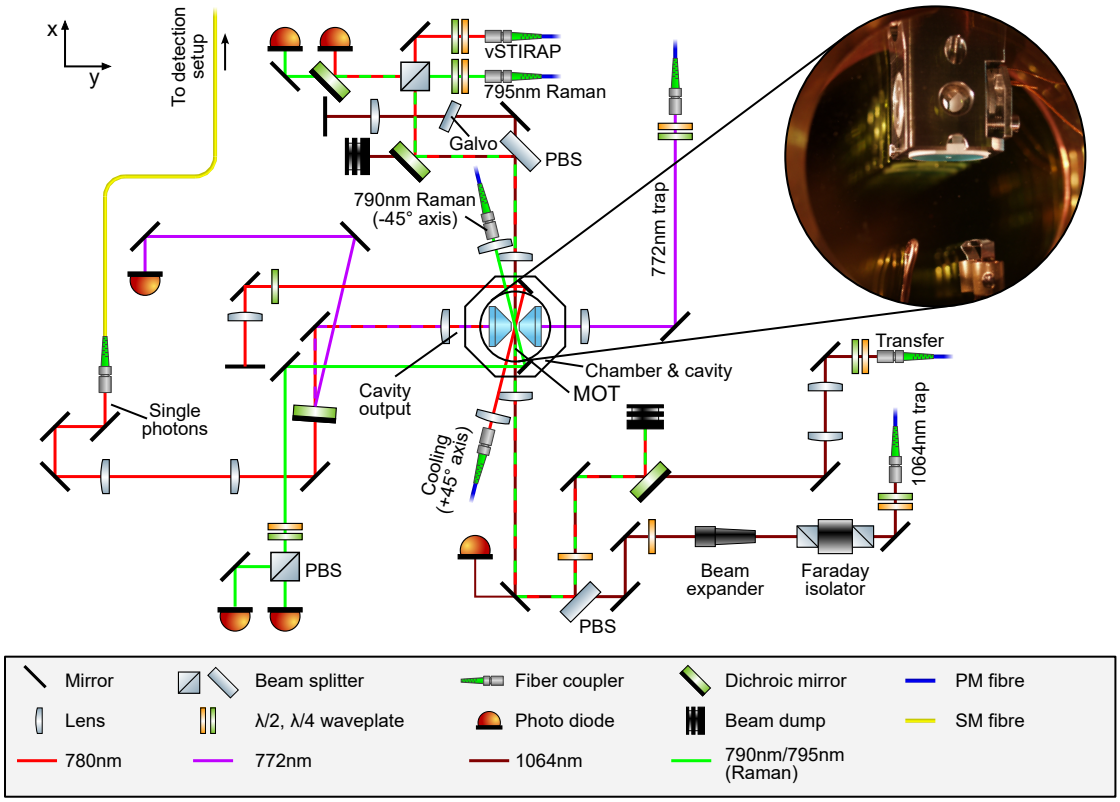

Figure 2.1.: Overview of the experimental apparatus. The vacuum chamber hosting the optical cavity is located in the centre and forms the heart of the setup. Around it several optical tracks are set up in order to manipulate the atoms with lasers. These include the optical traps at 1064 nm and 772 nm propagating along the x- and y-axis, respectively. The light for optical cooling and Raman rotations traverse the vacuum chamber at an angle of 45° from above. Another Raman laser at 795 nm and the photon generation control laser (vSTIRAP) are sent via the x-axis counterpropagating to the 1064 nm trap. Single photons are outcoupled from the left cavity mirror and coupled into a fibre leading to the detection setup. The inset shows a photograph of the cavity inside the vacuum chamber.

2.1.2. Rubidium atomic qubits

For over 15 years, our cavity experiment has employed rubidium as the atomic species of choice. Rubidium belongs to the alkaline atoms, which are located in the first column of the periodic table. Its optical transitions, in particular the D_1 and D_2 lines, fall within a spectral region that is readily accessible with commonly available laser wavelengths. The ease with which rubidium can be laser cooled renders it a popular choice for atomic physics experiments. Indeed, it was the first atomic species for which Bose-Einstein condensation was achieved experimentally [79]. Rubidium has two naturally occurring isotopes, ^{85}Rb

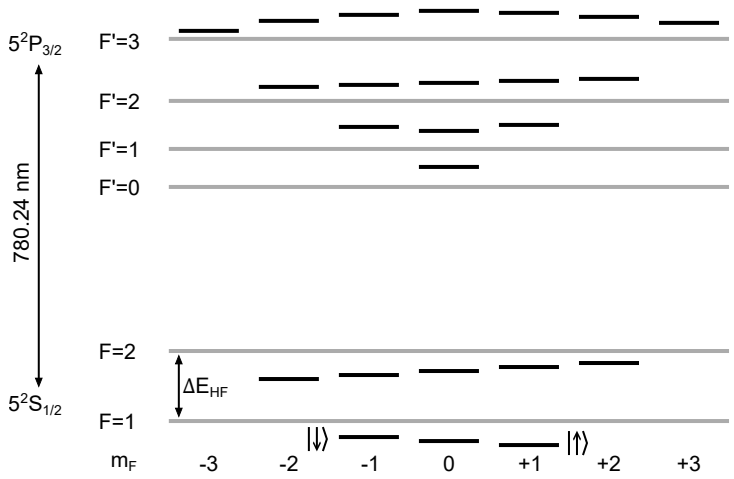

Figure 2.2.: Atomic level scheme ^{87}Rb. The diagram shows the atomic states of the D_2 transition, involving the $5^2S_{1/2}$ ground state and the $5^2P_{3/2}$ excited state. The ground state is split into two hyperfine levels with an energy splitting of $\Delta E_{\mathrm{HF}} = h \cdot 6.834\,\mathrm{GHz}$, where h is Planck's constant. A magnetic bias field parallel to the cavity axis splits each hyperfine manifold into several Zeeman sublevels. For the two ground states, this splitting is given by a Larmor frequency of $\omega_L/2\pi = 100\,\mathrm{kHz}$. Additionally, all levels experience an ac Stark shift due to the optical trapping potential. The unshifted levels are drawn in grey. The ac Stark shift and Zeeman splitting are not drawn to scale.

and ^{87}Rb, both of which are commonly employed in physics laboratories worldwide. Our group opted for ^{87}Rb as it has fewer Zeeman sublevels within its ground state manifolds, which better aligns with the requirements of our experiments.

The atomic level scheme is sketched in Fig. 2.2. More specifically, the diagram shows the atomic states involved in the D_2 transition at 780 nm, as most of the optical manipulations are performed via this transition, including single-photon generation. Due to a nuclear spin with quantum number $I = 3/2$ coupling to the angular momentum of the electron, the $5^2S_{1/2}$ ground state is split into two hyperfine manifolds. These have a total angular momentum of $F = 1$ and $F = 2$ and are separated in energy by $\Delta E_{\mathrm{HF}} = h \cdot 6.834\,\mathrm{GHz}$. The $5^2P_{3/2}$ excited state also splits up into a total of four hyperfine states. In the presence of a magnetic field, each of the hyperfine states within the ground (excited) state is again split into multiple Zeeman sublevels with quantum numbers m_F (m'_F). For the majority of experiments presented in this thesis, the energy splitting between adjacent m_F states is given by a Larmor frequency of $\omega_L/2\pi = 100\,\mathrm{kHz}$.

Throughout this thesis, we will frequently express the atomic state in the short hand notation $|F,m_F\rangle$ ($|F',m'_F\rangle$). Due to the hyperfine and Zeeman splitting, the ground state $5^2S_{1/2}$ has a total of eight sublevels. Two of these states, namely $|\uparrow\rangle \equiv |1,+1\rangle$ and $|\downarrow\rangle \equiv |1,-1\rangle$, are of particular importance, as they serve as the atomic qubit states for our experiments. Other sublevels are used as intermediate or transitional states for certain operations, such as photon generation and single-qubit Raman rotations.

2.1.3. The cavity

The optical cavity is undoubtedly the central component of the entire experimental system. It is made up of two macroscopic mirrors made from a fused silica substrate. The mirror surfaces are coated with a highly reflective dielectric coating. Their residual transmission is $T_1 = 4$ ppm and $T_2 = 101$ ppm. They are arranged in a Fabry-Pérot type geometry with

the two mirror facets facing each other at a distance of $L = 498\,\mu\text{m}$, corresponding to a free spectral range of $\text{FSR} = c/2L = 301\,\text{GHz}$. Because of the small physical dimensions of the cavity mode, the mirror substrate is radially milled down to a conical shape in order to ease optical access to the centre of the cavity mode. The mirrors have curved reflective surfaces with a radius of curvature of $r_{1,2} = r = 50\,\text{mm}$ in order to meet the stability criterion for optical cavities, which is given by the inequality

$$0 \leq (1 - L/r_1)(1 - L/r_2) \leq 1\,. \tag{2.1}$$

The cavity is mechanically mounted inside a metal housing and held by a combination of holders, spacers and a cylindrical piezo element. The setup is designed to hold the cavity mirrors in a stable position without exerting excessive mechanical stress on the mirror substrate. The electrical contacts of the piezo are connected to wires that lead to the outside of the experimental chamber via vacuum feedthroughs. The length of the cavity can then be controlled and actively stabilised by applying a voltage.

The transmissivities T_1 and T_2 are intentionally chosen to be unequal such that the decay of the cavity field occurs primarily through the mirror with the larger transmissivity. This mirror then serves as a well-defined output port for single photons that are coupled into an optical fibre and guided to a detection setup (left output port in Fig. 2.1). The decay via this out-coupling mirror is characterised by a decay rate of $\kappa_{\text{oc}}/2\pi = 2.42\,\text{MHz}$. Photons that leave the cavity via the other mirror have to be considered lost. Other loss channels are scattering and absorption due to imperfections of the mirror surfaces. The total cavity decay rate including the out-coupling channel and all loss channels is $\kappa/2\pi = 2.74\,\text{MHz}$. The ratio of κ_{oc} and κ then defines the output directionality or escape efficiency $\eta_{\text{esc}} = \kappa_{\text{oc}}/\kappa = 0.89$. Finally, the cavity finesse is $\mathcal{F} = 55059$. All characteristic quantities of the cavity are summarised in Table 2.1.

Cavity length	$L = 498\,\mu\text{m}$
Radius of curvature	$r = 50\,\text{mm}$
Optical mode waist	$29.6\,\mu\text{m}$
Mirror transmissivities	$T_1 = 4\,\text{ppm}$, $T_2 = 101\,\text{ppm}$
Free spectral range	$\text{FSR} = 301\,\text{GHz}$
Finesse	$\mathcal{F} = 55059$
Cavity decay rate	$\kappa/2\pi = 2.74\,\text{MHz}$
Escape efficiency	$\eta_{\text{esc}} = 0.89$

Table 2.1.: Cavity parameters. Summary of the most important quantities characterising the cavity. The values are taken from [76] and [80].

Cavity quantum electrodynamics

In simple terms, the cavity acts as an echo chamber for the electromagnetic field. Light that propagates within the cavity performs many roundtrips between the two mirrors, thereby enhancing the energy exchange rate between the atom and the light field within the cavity mode.

Using the atomic properties of rubidium, we can then describe the combined atom-cavity system within the framework of cavity QED [81]. In this context, an essential quantity to consider is the coherent light-matter coupling strength between the atom and the cavity

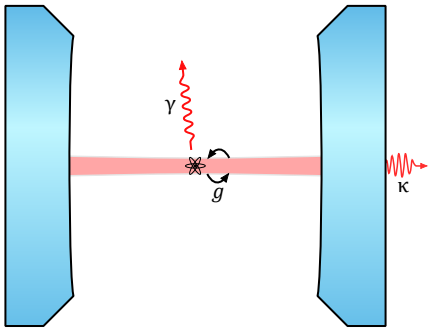

Figure 2.3: Cavity QED. The atom-cavity system is described in the framework of cavity QED. The relevant parameters are the atom-cavity coupling g, the atomic polarisation decay rate γ and the cavity field decay rate κ.

field, which is given by

$$g = \sqrt{\frac{\omega}{2\epsilon_0 V\hbar}}\mu_{ge}\,. \tag{2.2}$$

Here, ω is the resonance frequency of the cavity, ϵ_0 the vacuum permittivity, V the cavity mode volume, $\hbar$ the reduced Planck's constant and μ_{ge} the dipole matrix element of the atomic transition. The coupling constant g describes the frequency of coherent exchange of excitation between the atomic dipole and the electric field of a single photon in the cavity mode. In our cavity QED system, the coherent atom-cavity coupling described by the parameter g competes with two dissipative processes, namely the cavity field decay rate κ and the atomic polarisation decay rate γ, as illustrated in Fig. 2.3. The cooperativity C, defined as

$$C = \frac{g^2}{2\kappa\gamma}\,, \tag{2.3}$$

can be understood as the ratio between these different processes and is commonly used as a metric to characterise a cavity QED system. Note that g and C depend on the specific transition between the ground and excited state and have to be weighted with the relevant Clebsch-Gordan coefficient c_{ge} accordingly. They are largest for the cycling transition $\left|5^2S_{1/2},F=2,m_F=\pm2\right\rangle \leftrightarrow \left|5^2P_{3/2},F'=3,m'_F=\pm3\right\rangle$ for which we get $g/2\pi = 7.62\,\mathrm{MHz}$ and $C = 3.5$. As will become clear later on, the transition $\left|5^2S_{1/2},F=1,m_F=\pm1\right\rangle \leftrightarrow \left|5^2P_{3/2},F'=2,m'_F=\pm2\right\rangle$ is the one that is most relevant for the experiments conducted in this thesis. For this transition, the Clebsch-Gordan coefficient is $c_{eg} = \sqrt{1/4}$. Consequently, the coupling strength is $g/2\pi = 5.39\,\mathrm{MHz}$, which gives rise to a cooperativity of $C = 1.75$.

2.1.4. Atom loading and trapping

For the experiments described in this thesis, we require either one or two atoms at the centre of the cavity. Therefore, prior to the actual experimental protocol, we need to perform a sequence of steps in order to transfer the atom(s) to the centre of the cavity mode and trap them for as long as possible. In addition to the description that follows, the sketch shown in Fig. 2.1 may serve as a visual aid to understanding this procedure.

The sequence is initialised by preparing a MOT roughly 13 mm away from the cavity centre. After a typical MOT duration of 0.2 s-2 s the 1064 nm transfer beam is switched on for a duration of 150 ms. This beam propagates perpendicular to the cavity axis and focuses between the MOT and the cavity mode. Atoms initially at rest will be accelerated away from the MOT towards the focus of the transfer beam and start oscillating between the MOT and the cavity centre. After half of the oscillation period, when the atoms

reach the cavity mode, the 1064 nm trap is switched on. This beam is retro-reflected, thus forming a periodic standing-wave potential in which the atoms are tightly confined along the x-direction. A second trapping laser at 772 nm propagates within the cavity mode and provides tight confinement along the y-direction, as it also forms a standing wave. Since it is blue-detuned with respect to the atomic resonance, the atoms are trapped at the nodes of this standing-wave potential. However, the coupling g between the atom and the cavity undergoes a modulation along the cavity axis with a periodicity distinct from that of the trapping potential. Consequently, one must identify an optimal trapping position to maximise the atom-cavity coupling. This condition is fulfilled at positions where an anti-node of the 780 nm field aligns with a node of the 772 nm trapping potential. In addition to the purpose of providing axial confinement, the 772 nm trapping laser also serves as a frequency reference to which the resonance of the cavity is stabilised using the Pound-Drever-Hall technique [82]. Confinement along the z-direction is provided only by the Gaussian mode envelope of the 1064 nm trap.

Once the atoms reach the trapping region, they are laser cooled using Sisyphus cooling [34, 83]. To this end, a linearly polarised red-detuned laser beam is directed towards the atom via the +45° axis and then reflected back using a mirror positioned at normal incidence (see Fig. 2.1). As the beam passes through a $\lambda/4$ waveplate twice, the polarisation is rotated by 90° to be orthogonal to the input. This configuration is commonly referred to as the lin$\perp$lin configuration.

During operation of the system, consecutive experimental runs are repeated periodically interleaved with ~ 1 ms segments of cooling. The exact cooling duration depends on the specific protocol and should be adjusted to give an experimental duty cycle of about 50%. This number is a compromise between maximising the repetition rate of the experiment and increasing the amount of fluorescence light collected via the imaging system.

Atom positioning

The position of the atoms is controlled deterministically in the x-direction and quasi-deterministically in the y-direction. The x-position is controlled by adjusting the relative phase between the two counterpropagating trapping beams at 1064 nm. To this end, a transmissive glass plate is mounted in the beam path on a rotational Galvo scanner (see Fig. 2.1). By rotating the glass plate, the optical path length is changed and the standing-wave pattern shifts along the propagation direction. The electrical input that sets the rotation angle of the Galvo scanner is directly controlled by the experimental control software, which also acquires the atom images. The software automatically applies a feedback to the Galvo scanner to position the atoms to the desired location.

This method allows to precisely control a single position parameter, that is the x-coordinate of a single atom or the centre-of-mass coordinate of multiple atoms. However, this technique is not capable of controlling the relative distance between atoms. Along the y-direction such phase control is impossible, since the position of the standing-wave pattern is given by the position of the cavity mirrors. In this instance, the 772 nm trap power is modulated in order to induce a random movement of the atom. This step is repeated until the atom is found at the desired y-coordinate. The positioning procedure described above requires an imaging system that spatially resolves the atomic position, which will be introduced in the following.

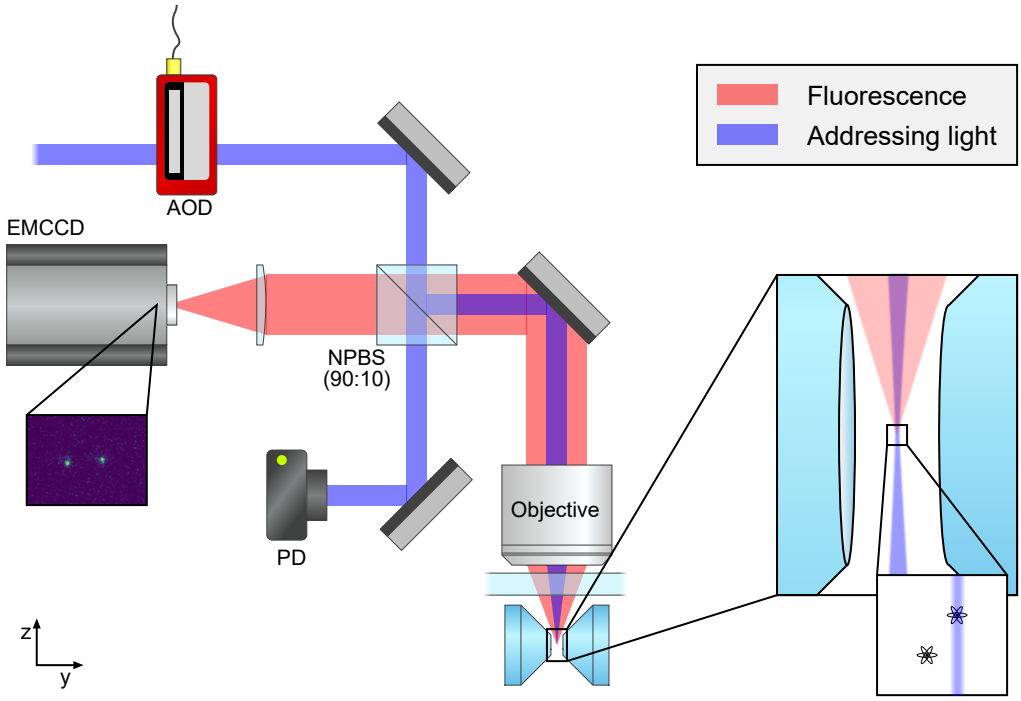

Figure 2.4.: Imaging and addressing of single atoms. The objective of $NA = 0.46$ is mounted close to the top view port of the vacuum chamber. Light scattered from the atoms is guided to the EMCCD camera. The addressing laser beam passes through an acousto-optic deflector (AOD) and is combined with the imaging path using a non-polarising beam splitter (NPBS) with a transmission:reflection ratio of 90:10. The transmitted light is picked up by a photodiode (PD) for power stabilisation. The reflected part passes through the objective to be focused on the atoms. Varying the frequency on the AOD changes the deflection angle and shifts the position of the focal spot along the x-axis (out-of-plane direction). This allows to focus the beam on one atom without affecting the other one.

2.1.5. Single atom imaging and addressing

The top view port of the vacuum chamber accommodates an optical objective which serves two functionalities at once. First, it collects fluorescence emitted by the atoms, enabling spatial resolution of their positions. Second, it allows to address individual atoms with a classical laser beam, utilising the same optical path in the opposite direction. An overview of the imaging optics and the addressing system is shown in Fig. 2.4.

Imaging system

In numerous situations, the experiment crucially depends on the ability to detect atoms in the cavity, in conjunction with knowing the exact number of atoms and their respective positions. For this purpose, the experiment is equipped with a high-resolution imaging system consisting of a high-numerical-aperture objective and an electron-multiplying charge-coupled device (EMCCD) camera. The objective was implemented as part of a Master's thesis [84]. It has a numerical aperture of $NA = 0.46$ and is mounted in close proximity to the top viewport of the vacuum chamber. During laser cooling, the atoms scatter photons into free space, which are then collected by the objective and guided to the EMCCD camera. As demonstrated in a previous PhD thesis [80], the imaging system in principle allows to resolve single lattice sites of the trapping potential. However, when working with multiple atoms, the spatial separation is typically several micrometres, which

is sufficiently above the level of accuracy achieved by the imaging system. The camera images are analysed in real time by the experimental control software. Whenever an atom moves away from its desired position, the control software applies a corrective feedback as described in chapter 2.1.4.

Single-atom addressing

While the objective collects fluorescence light for imaging of the atoms, it also serves the purpose of addressing individual atoms with a laser beam. The addressing system was set up by former PhD student Andreas Neuzner as a shoot-out system that removes undesired atoms from the trap using resonant laser light [80]. The functionality of the system was then extended to the local storage and emission of single photons by PhD student Stefan Langenfeld [85].

The addressing laser beam is simply injected into the imaging path using a 90:10 non-polarising beam splitter. It is then focused on the desired position by the objective. For switching and steering of the laser beam, we use a 1D acousto-optic deflector (AOD) controlled with a radio frequency (RF) signal. As the deflection angle is proportional to the applied RF frequency, the beam can be directed to specific positions along the x-axis. The beam profile is asymmetrically shaped with beam waists of $w_x = 2\,\mu$m and $w_y = 6\,\mu$m. Along the x-axis, the waist is sufficiently small to discriminate between atoms at μm distances without crosstalk. For the y-axis, the beam size is chosen to be larger in order to accommodate a wider range of atom positions, compensating for the fact that along this axis positioning does not occur fully deterministically.

The RF source that is fed to the AOD is generated by a direct digital synthesizer (DDS) with up to eight profiles. Each profile can store an amplitude and frequency parameter. The experimental control software automatically detects the atoms on the EMCCD camera image and assigns a profile to each atom with the frequency matching the atom position. At any given time, one of the eight profiles is selected via binary encoding of three TTL (transistor-transistor logic) inputs. This enables switching on the timescale of ($< 20\,\mu$s) between two atom positions, limited by the speed of sound inside the AOD crystal. While this is sufficiently fast for most applications, there are cases in which the switching time may become a limitation. For example, in order to make two subsequently emitted photons interfere on a beam splitter, the switching time must be as short as possible in order to avoid the use of long delay lines. For this application, the switching time of 20 µs would be too long.

Another limitation of this system is the restriction the AOD imposes on the polarisation. The AOD only functions for a single polarisation, which in our experiment is set to π polarisation. This has the consequence that Raman transitions, as described in chapter 2.2.3, cannot be performed locally using the addressing system.

2.1.6. Detection setup

Measuring the polarisation state of single photons is crucial for the experiments conducted in this thesis. Indeed, all of the experimental data presented rely on the detection of single photons that were outcoupled from the cavity mode. The detection optics, as shown in Fig. 2.5, therefore plays a central role in performing the measurements. It enables us to measure photonic polarisation qubits in the Z or X basis and switch between these two settings dynamically within a few nanoseconds.

Similar to a standard detection setup for polarisation qubits, it involves a polarising beam splitter (PBS) and two single-photon detectors. For the latter, we use two channels

of a superconducting nanowire single-photon detector (SNSPD). These feature state-of-the-art detection efficiencies of $\sim 95\%$ and low dark count rates on the 1 Hz scale. The PBS discriminates horizontal (H) from vertical (V) polarisation. A $\lambda/2$ waveplate is installed on a motorised rotation mount directly in front of the PBS. This allows us to rotate the detection basis from H/V to any other linear polarisation, e.g. diagonal (D) and anti-diagonal (A). Furthermore, the waveplate is mounted on a magnetic mount, allowing for convenient insertion and removal as required.

Any other detection basis setting can in principle be realised by an appropriate unitary rotation performed upstream from the PBS. In particular, we use an electro-optic modulator (EOM) to enable the measurement in the basis defined by right-hand (R) and left-hand (L) circular polarisation (Z basis) by rotating the polarisation in front of the PBS. A second EOM corrects for a time-dependent phase evolution of the emitted photons. The functionality of both EOMs is described in the following in more detail.

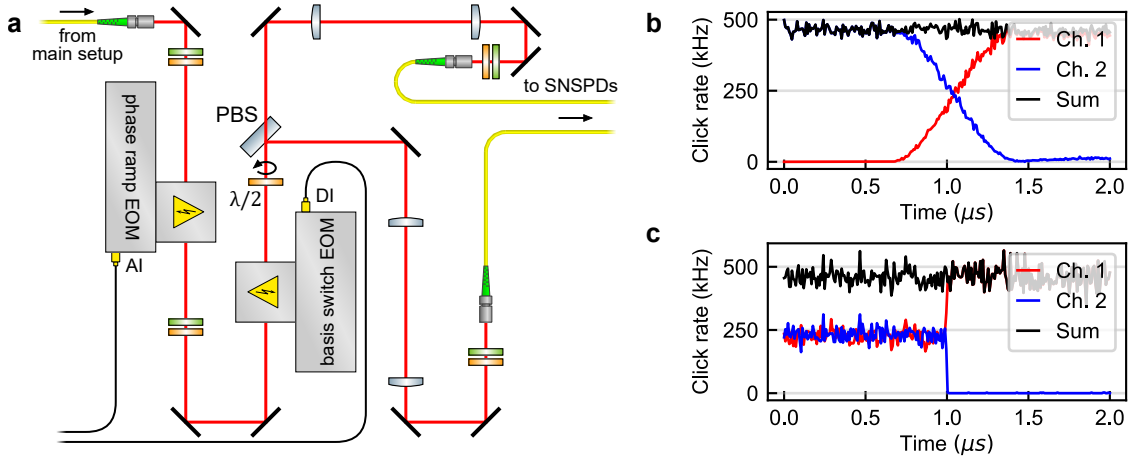

Figure 2.5.: Dynamically switchable polarisation-resolving detection setup. (**a**) Sketch of the optical setup. A PBS is used to discriminate between two orthogonal polarisations and to separate them into two optical channels. Both channels are coupled into optical fibres that are connected to SNSPDs. For each detection channel a 1:1 telescope is used to maximise the optical mode matching for higher detection efficiencies. Two polarisation EOMs are used, one for switching the detection basis and the other for applying a linear phase ramp to one of the polarisation components (see main text). They are supplied with an analogue input (AI) and a digital input (DI), respectively. (**b**) Calibration measurement for the phase ramp EOM. Using classical laser light, a linear voltage ramp is applied to the analogue input of the EOM. This rotates the polarisation as can be seen from the click rate in the two channels. (**c**) Calibration measurement for the basis switch EOM. For an R-polarised input, the light is evenly split up into the two channels. When applying the voltage $V_{\pi/2}$, the polarisation is rotated to H such that all the light is directed into channel 1.

Phase ramp compensation

The first EOM (QUBIG PC3R-NIR) has the purpose of compensating a time-dependent phase between the σ^+ and σ^- polarisation components of the photons. The photon generation mechanism is a two-photon Raman process described in more detail in chapter 2.2.2. Fig. 2.6 illustrates how the frequency of the photon depends on the m_F state from which the emission occurs. If a photon is generated from a superposition of the $|2, \pm 2\rangle$ states, the atom undergoes a transition to $|1, \pm 1\rangle$. For the two emission paths, the energy difference between the initial and the final state is either $\Delta E_{HF} + 3\hbar\omega_L$ or $\Delta E_{HF} - 3\hbar\omega_L$. Here, ΔE_{HF} is the hyperfine splitting and ω_L the Larmor frequency. This translates into

a frequency difference of $6\omega_L$ between the R (σ^+) and L (σ^-) components of the photonic qubit. In other words, the qubit basis states experience a relative phase shift that increases linearly with time. The larger the phase acquired during the duration of the photonic wave packet, the more infidelity is introduced. For the scenario depicted in Fig. 2.6 and with $\omega_L = 100\,\text{kHz}$, the phase accrual amounts to $\pi/4$ after about 400 ns, which is on the order of the photonic wave function duration. Hence, we expect a substantial effect on the fidelity, in particular for a quantum state consisting of many photons.

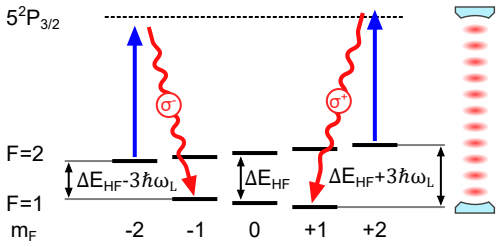

Figure 2.6: Photon phase ramp. The frequency of the emitted photon depends on the emission path. For photon generation from $|2, \pm 2\rangle$, the frequency difference between the σ^+ and σ^- components is $6\omega_L$.

In order to compensate for this effect, we developed a technique based on controlling the phase of the polarisation states with an EOM. The device we use for this purpose has an analogue input and imprints an optical phase on one of the eigenaxes of the crystal with respect to the other. As we want to induce a phase between the R and L components of the light field, we use a set of waveplates to map the two circular polarisations to the eigenaxes D (diagonal) and A (anti-diagonal) at the position of the EOM. With every photon emission we then apply a linear ramp waveform to the analogue input of the EOM counteracting the phase evolution due to the Zeeman splitting. Fig. 2.5b shows a calibration measurement demonstrating this effect. A classical light field with linear polarisation is introduced into the EOM. The detection basis is set such that all light is directed to a single detector for an input voltage of zero. As the voltage increases, the polarisation is rotated until all photon counts are registered in the other detector. The slope of the voltage ramp is tuned such that the frequency of the oscillation matches the phase evolution between the R and L components.

Detection basis switching

The second EOM (QUBIG PC3R-NIR) serves the purpose of dynamically switching between two predefined basis settings, namely the Z and X bases. Its operation principle resembles that of the phase ramp EOM, except that the voltage does not follow a linear slope, but is switched in a step-wise fashion. This enables the EOM to execute a $\pi/2$ rotation on the qubit. Again, a calibration measurement can be seen in Fig. 2.5c. Initially the voltage is set to zero, which corresponds to the X basis setting. The R polarized light is split up equally into both detectors. As soon as the voltage is switched to $V_{\pi/2}$, all of the light is directed into one of the two detectors. While the extinction ratio of the device is specified as >1,000:1, we typically achieved values above 2,000:1 in our setup, sometimes even as high as 10,000:1. The switching time required to switch from one setting to the other is on the order of 5 ns. The photons generated are typically separated by tens of microseconds, which is considerably longer than the switching time.

2.2. Experimental toolbox

In the preceding section, the various components of the experimental apparatus and the procedures for loading, trapping, cooling and imaging of single atoms were introduced.

In this section, we introduce the elementary tools that define the building blocks of the graph state generation protocols. Of particular importance are single-photon generation and coherent Raman rotations.

2.2.1. State preparation

The first step of each protocol is the initialisation of the atomic state. In all graph state experiments presented in this work, we initially prepare the atoms in $|2,0\rangle$, before generating a photon from this state. This is achieved using the well-established technique of optical pumping [86, 87]. More specifically, we use two laser fields to incoherently transfer the population to the desired initial state. The corresponding processes are illustrated in Fig. 2.7.

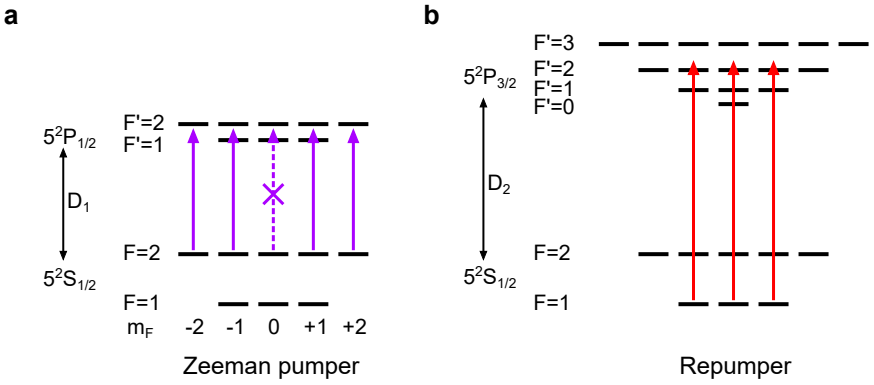

Figure 2.7.: Zeeman-selective optical pumping. (**a**) The Zeeman pumper drives the $|F = 2\rangle \rightarrow |F' = 2\rangle$ transition on the D_1 line. The $m_F = 0$ sublevel is a dark state due to dipole selection rules. (**b**) Population in $F = 1$, which is not addressed by the Zeeman pumper, is transferred back to $F = 2$ using the repumper.

The Zeeman pumper (Fig. 2.7a) is a π polarised laser at 795 nm, which couples to the $|F = 2, m_F \neq 0\rangle \leftrightarrow |F' = 2, m_F \neq 0\rangle$ transitions of the atomic D_1 line. The target state $|F = 2, m_F = 0\rangle$ is a dark state, as the corresponding transition is dipole-forbidden. However, population in the $m_F \neq 0$ states will be excited, followed by a spontaneous decay with some probability of ending up in the dark state. Since the atom can also decay to the $F = 1$ manifold, we apply a second laser that repumps the $F = 1$ population back to $F = 2$ by driving the $\left|5^2S_{1/2}, F = 1, m_F\right\rangle \leftrightarrow \left|5^2P_{3/2}, F' = 2, m'_F\right\rangle$ transition. The repumper has a wavelength of 780 nm, thereby coupling to the atomic D_2 line.

For both light fields, we find that the pumping scheme works best when the laser is slightly detuned from resonance. We observe that when the laser is tuned to resonance, the atom trapping deteriorates, which we attribute to an increased momentum transfer from the pumping lasers. For the Zeeman pumper, we choose a detuning of $\Delta = -38$ MHz, while for the repumper the detuning is $\Delta = 47$ MHz.

In order to achieve a high fidelity and efficiency in the initial state preparation, we developed an optical pumping scheme that was already used in previous experiments [85, 88]. The protocol consists of two steps. First, we apply the Zeeman pumper and the repumper simultaneously for 5 µs. During this period, the atomic population gradually accumulates in the $|F = 2, m_F = 0\rangle$ target state. In the second stage, we only apply the Zeeman pumper for 3.5 µs, while the optical power is doubled. This empties the states $|F = 2, m_F \neq 0\rangle$ with a $1/e$ decay time of less than 1 µs, thereby pumping the population either to the dark state $|F = 2, m_F = 0\rangle$ or to the $F = 1$ manifold. The relative

contribution of populations in these states determines the overall efficiency of the process. For our parameters, we achieve a probability of about 60% to populate the $|F = 2, m_F = 0\rangle$ state after one pumping cycle. We do tolerate this number to be substantially below 100%, as the population in $F = 1$ does not contribute to the subsequent photon emission. It is, however, essential that no population remains in the $|F = 2, m_F \neq 0\rangle$ states, as these would degrade the atom-photon entanglement fidelity (see chapter 2.2.5). The efficiency could be increased with a longer pumping time. However, this would also lead to a larger average number of scattered photons, which would increase the heating rate of the atom. Our settings represent a compromise between state preparation efficiency and trapping time.

2.2.2. Single-photon generation (vSTIRAP)

The generation of single photons is a ubiquitous problem in QIP, particularly in the context of quantum communication, where qubits are transmitted over large distances. The preparation of a true single-photon Fock state is a non-trivial task, as such a state is inherently different from a coherent state with an average photon number of $\langle n \rangle = 1$. Atoms or molecules, on the other hand, naturally emit single photons when relaxing from an excited state to a lower energy state via spontaneous emission. In the presence of a single emitter, only one photon can be generated at a time, since the system can only contain a single excitation at once. Apart from atoms and molecules, such systems can be realised in practice using a variety of physical systems, ranging from semiconductor quantum dots, trapped ions or colour-centres in diamond. Many of these systems, e.g. quantum dot sources [89], rely on the Purcell effect [90–92] to break the isotropy of spontaneous decay and direct the emission into a well-defined spatial mode. This is achieved by enhancing the photonic density of states using optical cavities or nanophotonic structures.

The vSTIRAP mechanism

The photon generation mechanism employed in this work differs from this Purcell-like emission in two respects. Firstly, our scheme involves three energy levels in a Λ-type configuration (instead of two), as sketched in Fig. 2.8. Secondly, the emission occurs as part of a two-photon Raman process, in which a photon is absorbed from the control field $\Omega(t)$ on the $|g_2\rangle \leftrightarrow |e\rangle$ transition and immediately re-emitted on the $|e\rangle \leftrightarrow |g_1\rangle$ transition, stimulated by the cavity mode. In a simple picture, this process can be understood as coherent Raman scattering into the optical resonator. In the ideal case, the excited state $|e\rangle$ remains unpopulated during this process. This is different from the typical scheme of quantum dot sources, in which the population is fully transferred to the excited state with an optical π pulse, followed by a spontaneous decay.

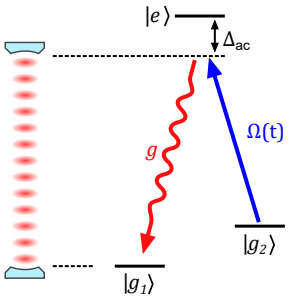

Figure 2.8: Photon generation via the vSTIRAP mechanism. The atom-cavity coupling is quantified by the coupling constant g. The control laser (blue) is described by the time-dependent control parameter $\Omega(t)$. The fields associated with g and $\Omega(t)$ induce a two-photon transition from $|g_2\rangle$ to $|g_1\rangle$. In the process, a photon is emitted into the cavity.

The Λ-scheme displayed in Fig. 2.8 can be simply mapped to the level scheme of ^{87}Rb

(Fig. 2.2) by declaring $|g_2\rangle \equiv |F = 2, m_F\rangle$ and $|g_1\rangle \equiv |F = 1, m_F \pm 1\rangle$. For a π-polarised control field $\Omega(t)$, only transitions with $\Delta m_F = \pm 1$ are possible due to the conservation of angular momentum. Processes with $\Delta m_F = 0$, accompanied by the emission of a π-polarised photon, cannot occur due to the alignment of the quantisation axis with the cavity axis. In our experiment, the atom-cavity detuning is set to $\Delta_{ac} = -150\,\mathrm{MHz}$, which, for historical reasons, we define with respect to the transition $\left|5^2S_{1/2}, F = 1, m_F = 1\right\rangle \leftrightarrow \left|5^2P_{3/2}, F' = 1, m'_F = 1\right\rangle$.

For over two decades, the two-photon Raman process in the Λ-scheme has been considered for coherent single-photon storage and retrieval. The underlying physics has been extensively investigated and applied to the case of free space atomic media [93–97], but also atomic ensembles [98] and single atoms coupling to a cavity [99, 100]. This formalism was subsequently extended to the case of multiple excited states $|e_i\rangle$ [70, 101], as present on the atomic D_2 line of rubidium.

Two findings from the aforementioned scientific literature will be examined in the subsequent discussion. In line with the topic of this thesis, we will focus on the emission process and not consider single-photon storage.

First, there is a tight relation between the temporal wave function of the photon and the time-dependent control field $\Omega(t)$. This allows to arbitrarily shape the photonic temporal wave function $\epsilon(t)$ [70]. This feature is not available in the spontaneous emission scheme of quantum dot sources. Second, the optimal efficiency of this process is[1]

$$\eta_0 = \frac{2C}{2C+1}\,, \tag{2.4}$$

independently of the control field $\Omega(t)$ and the photon wave function $\epsilon(t)$, provided that no population is left in the initial state $|g_2\rangle$.

A condition that is frequently assumed [98, 99] in the mathematical treatment of the problem is that the control pulse $\Omega(t)$ is sufficiently smooth, such that the excited state population can be adiabatically eliminated from the equations. If this condition is fulfilled, the process closely resembles a stimulated Raman adiabatic passage (STIRAP) in which one branch of the transition is driven by the vacuum cavity field. Hence, it is sometimes referred to as vacuum-STIRAP or vSTIRAP [102]. In contrast, for the experiments described in this thesis, we simply use a square pulse as control field $\Omega(t)$. This has certain practical advantages, as no waveform programming is required for the synthesis of the control field, but it may not fulfil the adiabaticity criterion. However, as we operate at an atom-cavity detuning of $\Delta_{ac} = -150\,\mathrm{MHz}$, the population in the excited state(s) $|e\rangle$ ($|e_i\rangle$) is anyway expected to be small. Therefore, we will adhere to the naming convention established previously and refer to the photon generation mechanism as vSTIRAP.

2.2.3. Coherent Raman transitions

Another essential component in the toolbox needed for the generation of multiphoton entangled states is the ability to coherently manipulate the atomic state. Since the hyperfine splitting between the ground state manifolds of rubidium is 6.834 GHz, one may consider microwave radiation in order to drive transitions between these states. We do indeed have a microwave horn antenna mounted in close proximity to the vacuum chamber, but the amount of radiation that reaches the atom does not suffice to drive these transitions fast enough. Therefore, we use the microwave antenna merely for spectroscopy purposes.

[1] The cooperativity parameter C occasionally varies in its definition by a factor of 2. Consequently, the efficiency may be expressed as $\eta_0 = C/(C+1)$ in other literature sources.

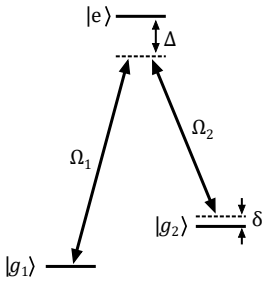

Figure 2.9: Stimulated Raman transition in a Λ-system. Both ground states $|g_1\rangle$ and $|g_2\rangle$ are coupled to the excited state $|e\rangle$ by two lasers with coupling strength Ω_1 and Ω_2, respectively. The two laser fields are detuned from the excited state $|e\rangle$ by the one-photon detuning Δ. The frequency difference between the two lasers equals the energy difference between $|g_1\rangle$ and $|g_2\rangle$ up to the two-photon detuning δ.

Instead, the coherent manipulations are based on two-photon Raman transitions, similar to the vSTIRAP mechanism described in the previous section. The underlying effect is often exploited in the context of chemistry and material physics, where it serves as the basis for the well-established technique of Raman spectroscopy. In the atomic physics community, stimulated Raman transitions are a popular tool to manipulate the state of atoms. The general use case is again a three-level Λ-system that consists of three states $|g_1\rangle$, $|g_2\rangle$ and $|e\rangle$ (Fig. 2.9). Typically, $|g_1\rangle$ and $|g_2\rangle$ are long-lived ground states, whereas $|e\rangle$ is a short-lived excited state. As for the vSTIRAP process, we then introduce a coupling for the transitions $|g_1\rangle \leftrightarrow |e\rangle$ and $|g_2\rangle \leftrightarrow |e\rangle$, whereas now both transition branches are coupled with classical laser beams with Rabi frequencies Ω_1 and Ω_2. In contrast to the vSTIRAP process, which is unidirectional, the stimulated Raman process can drive Rabi oscillations between the two ground states. We can then assign an effective Rabi frequency to the transition $|g_1\rangle \leftrightarrow |g_2\rangle$:

$$\Omega_0 = \frac{\Omega_1 \Omega_2}{2\Delta} \tag{2.5}$$

and effectively treat the system as a two-level system by eliminating the state $|e\rangle$ from the calculation. If the state of the system is $|g_1\rangle$ at time $t = 0$, the probability to measure state $|g_2\rangle$ after time t is,

$$P_{|g_2\rangle}(t) = \frac{\Omega_0^2}{\Omega^2} \sin^2\Big(\frac{\Omega t}{2}\Big), \tag{2.6}$$

where we have defined $\Omega = \sqrt{\Omega_0^2 + \delta'^2}$. Here, $\delta' = \delta + (\Omega_2^2 - \Omega_1^2)/4\Delta$ is defined in terms of δ, which is the bare two-photon detuning with respect to the unshifted levels. Hence, δ' is the effective two-photon detuning, taking into account the differential ac Stark shift $(\Omega_2 - \Omega_1)/4\Delta$ introduced by the two laser fields. From equation 2.6 we can see that we only get a full population transfer between the two states on two-photon resonance, i.e. $\delta' = 0$. In general, several excited states can contribute to the process. In this case, the Rabi frequency Ω_0 becomes a sum of multiple terms of the form $\Omega_1\Omega_2/2\Delta$, each of which represents the amplitude of the transition path via a certain excited state. Every term in this sum is then weighted with the Clebsch-Gordan coefficients associated with this transition path.

In our experiment, we use two Raman pairs that drive transitions between the $F = 1$ and $F = 2$ manifolds. The states $|g_1\rangle$ and $|g_2\rangle$ in Fig. 2.9 can in principle be any Zeeman sublevel of the ^{87}Rb hyperfine states $|F = 1\rangle$ and $|F = 2\rangle$, respectively, with the constraint that angular momentum is conserved in the process. The two Raman lasers operate at wavelengths of 790 nm and 795 nm, each serving distinct purposes, as explained below.

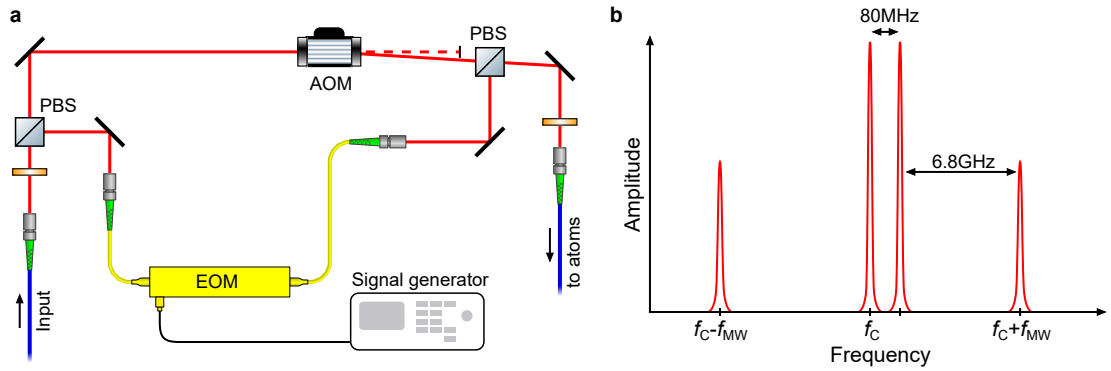

Figure 2.10.: 790nm Raman setup. (**a**) Sketch of the optical setup including the AOM and the fibre-coupled EOM. (**b**) Schematic plot of the optical spectrum of the light at the output of the setup. The phase-modulated light from the EOM track contains a carrier at a central frequency f_C and two sidebands shifted by f_{MW} to either side. The light from the AOM track is shifted by 80 MHz with respect to the EOM carrier. The Raman transition is driven by the two rightmost peaks, which have a frequency difference equal to the hyperfine splitting.

790nm Raman laser

The first Raman laser operates at a wavelength of 790 nm and is used for most of the atomic state manipulations in our experiments. It drives $\Delta m_F = \pm 1$ transitions between the $F = 1$ and $F = 2$ hyperfine ground states. The setup is shown schematically in Fig. 2.10a. The incoming laser beam is first split into two orthogonal linear polarisations. The reflected part is coupled into a fibre-coupled phase-modulation EOM, the transmitted beam passes through an acousto-optic modulator (AOM). The output of the EOM and the +1-order of the AOM are recombined on a PBS and coupled into a polarisation-maintaining (PM) fibre, leading to the main setup. As the two beams are orthogonal in polarisation, they are aligned to the fast and slow axes of the PM fibre, respectively. The output of the fibre is aligned in such a way that at the position of the atoms the two polarisation axes correspond to π and σ^+/σ^- polarisation in the atomic reference frame.

The output of a direct digital synthesizer (DDS) is used to drive the AOM with an RF signal of 80 MHz, thus shifting the first deflection order in frequency by the same amount. The EOM is driven with a microwave (MW) frequency of $\omega_{HF}/2\pi + 80$ MHz provided by a MW signal generator (Rohde&Schwarz SMF 100A). The driving frequency is the sum of the atomic hyperfine splitting $\omega_{HF}/2\pi$ and an offset which matches the frequency of the AOM. The spectral output of the EOM consists of a carrier equal to the input frequency f_C and two sidebands at frequencies $f_C \pm f_{MW}$, where f_{MW} is the microwave driving frequency. The spectrum of the light of both polarisation components is sketched in Fig. 2.10b. The offset of 80 MHz ensures that no intra-hyperfine transitions are driven by the EOM carrier and the output of the AOM.

Fig. 2.11a shows a spectrum of the various transitions between the two hyperfine states probed by the Raman laser. The atom is initialised in a mixture of the states $|1, \pm 1\rangle$. We then apply a pulse of fixed duration (25 µs) while scanning the MW frequency on the EOM over an interval of 800 kHz. The population in $|F = 2\rangle$ is read out with a photon emission into the cavity. The average number of photons detected per trial is plotted on the y-axis. The centre of the spectrum corresponds to the unshifted atomic hyperfine splitting. We observe a total of four peaks corresponding to the transitions as indicated in the level scheme. The peaks are separated from one another by 200 kHz due to the Zeeman splitting of 100 kHz. The two inner peaks have a lower amplitude. This is due to

a lower Rabi frequency Ω_0 resulting from the Clebsch-Gordan coefficients associated with the two-photon transition paths. We can then go on to drive Rabi flopping resonant to each of the four transitions (Fig. 2.11b-e). Again, we observe a difference in Rabi frequency for the inner and outer transition peaks, with the oscillation frequency differing by a factor of approximately 2.5.

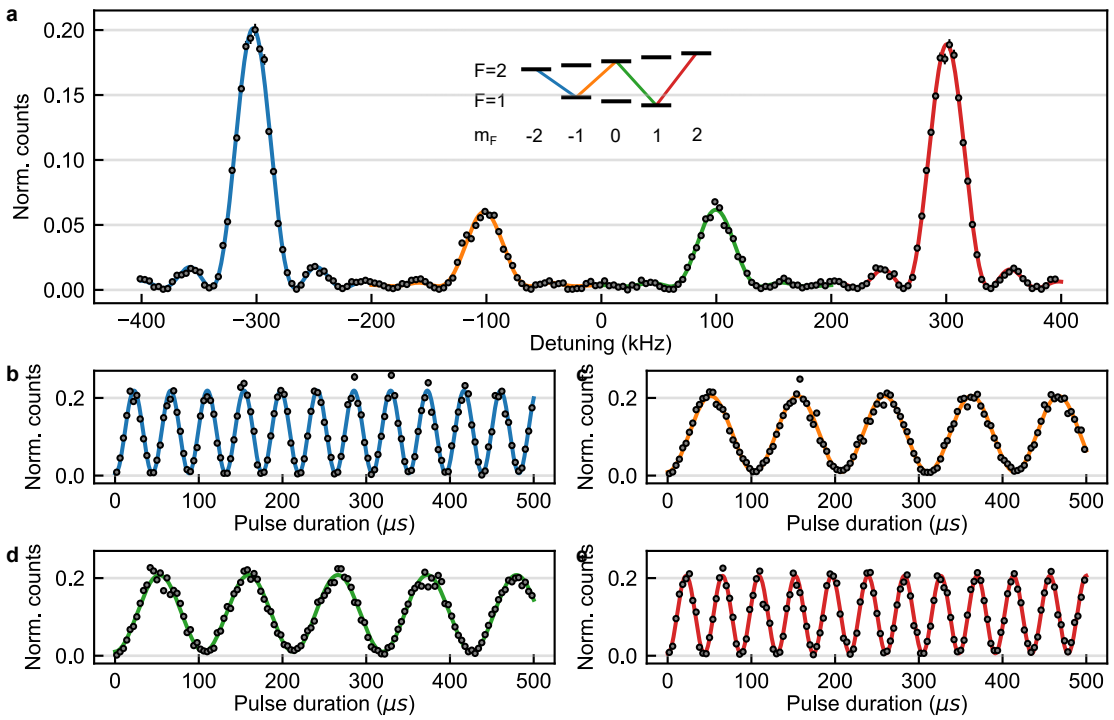

Figure 2.11.: Stimulated Raman transitions. (**a**) Spectrum of the $|F = 1\rangle \leftrightarrow |F = 2\rangle$ hyperfine transitions scanning the two-photon detuning. The four transition peaks are fitted using equation 2.6. The fits are plotted as solid lines, whose colours correspond to the transitions as indicated in the atomic level scheme. (**b-e**) Coherent Rabi flopping on the transitions seen in (**a**). Note that the spectrum in (**a**) was recorded using a reduced sideband amplitude on the EOM compared to (**b-e**). This results in narrower peaks and a better spectral resolution.

Single-qubit gates In the protocols described in chapter 4 and 5, we require single-qubit rotations between the qubit basis states $|\uparrow\rangle = |1, +1\rangle$ and $|\downarrow\rangle = |1, -1\rangle$. In principle, these could be implemented with a Raman laser directly addressing the $\Delta m_F = \pm 2$ transition between these states. However, in this scenario the two-photon transition paths interfere destructively for large detunings Δ (similar to the 795 nm Raman laser described further below). An alternative approach has been realized in one of our earlier works [88]. Here, we implemented a $\Delta m_F = \pm 1$ driving between the three Zeeman sublevels within the $F = 1$ hyperfine manifold via the intermediate level $|1,0\rangle$. Since the transitions $|1,0\rangle \leftrightarrow |1, \pm 1\rangle$ have the same transition frequency, they can only be driven simultaneously. It turns out that the intermediate level is only emptied after an integer number of π pulses, which consequently is the only gate operation possible in this scheme. Therefore, we modified this method to be able to drive $\pi/2$ rotations. Instead of $|1,0\rangle$ we use $|2,0\rangle$ as an intermediate state. Thanks to the Zeeman splitting, the two Raman transitions involved become distinguishable in frequency, as can be seen from the spectrum in Fig. 2.11a.

The single-qubit operation is then composed of three steps (Fig. 2.12a): First, the population in $|1,+1\rangle$ is transferred to the intermediate state $|2,0\rangle$ with a π pulse (①). Then, we perform the actual gate operation driving the transition $|1,-1\rangle \leftrightarrow |2,0\rangle$ for a time t_{gate} (②). In the last step, the intermediate state population is brought back to $|1,+1\rangle$ with another π pulse (③). The gate operation is characterised by measuring the correlations of the atomic state before and after the gate. Initially, the atom is projectively prepared in one of the eigenstates $|1,\pm 1\rangle$. We then apply the gate pulse sequence while scanning the gate time parameter t_{gate}. After the gate, we measure the state of the atom in the eigenbasis and compare the result with the initial state as a function of t_{gate} (Fig. 2.12b). We find that the composite pulse sequence realises an effective Rabi flopping between the qubit states $|\uparrow\rangle$ and $|\downarrow\rangle$. The parameter t_{gate} and the phase of the microwave signal ϕ_{MW} provide the necessary degrees of freedom to implement an arbitrary single-qubit rotation. However, in order to implement the protocols presented later on, $\pi/2$ pulses are sufficient.

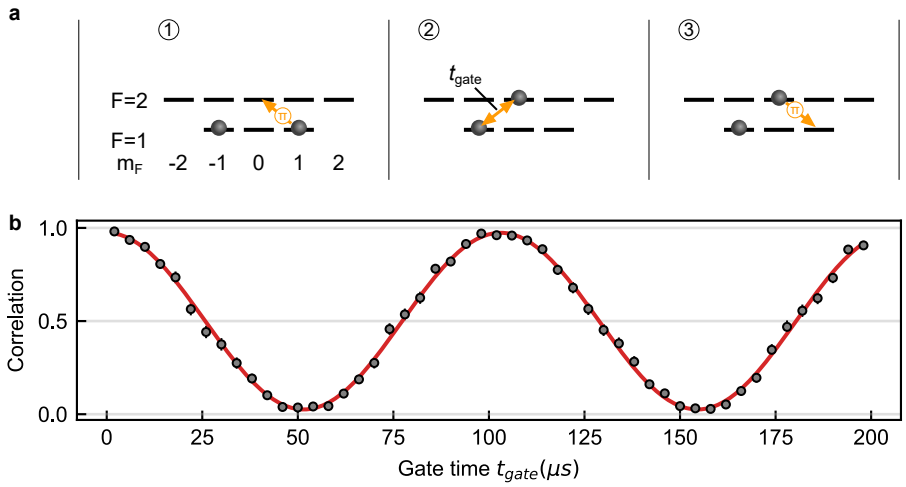

Figure 2.12.: Single-qubit gate. (**a**) Individual steps of the single-qubit gate. First, the $|1,+1\rangle$ population is transferred to the intermediate state $|2,0\rangle$. Next, we apply the actual gate operation on the transition $|1,-1\rangle \leftrightarrow |2,0\rangle$. Finally, we transfer the population in $|2,0\rangle$ back to $|1,+1\rangle$. (**b**) Effective single-qubit gate operation via the protocol shown in (**a**). The plot shows the correlation between the atomic state before and after the gate as a function of gate time t_{gate}. The oscillations have a visibility of 0.94(1).

795nm Raman laser

The second Raman laser in the experiment operates at 795 nm, driving Raman transitions via the atomic D_1 line. It addresses $\Delta m_F = \pm 2$ transitions between the two hyperfine manifolds. The purpose of this Raman laser is to transfer qubits from $|1,\pm 1\rangle$ to $|2,\mp 1\rangle$, enabling an atom-to-photon state transfer. During the emission from $|2,\mp 1\rangle$, the atom undergoes a transition to $|1,0\rangle$ and fully transfers the quantum state to the photon. This operation is only performed in the last step of the single-emitter protocols described in chapter 4.

A convenient feature of this transfer is that, even in the presence of a Zeeman splitting, both of the transitions can be addressed at the same resonance frequency, thus transferring both qubit state populations at the same time. The disadvantage is that the Rabi frequency Ω_0 vanishes for a large one-photon detuning Δ due to a destructive interference in the transition paths. Therefore, we have to choose a wavelength at which Δ is positive for

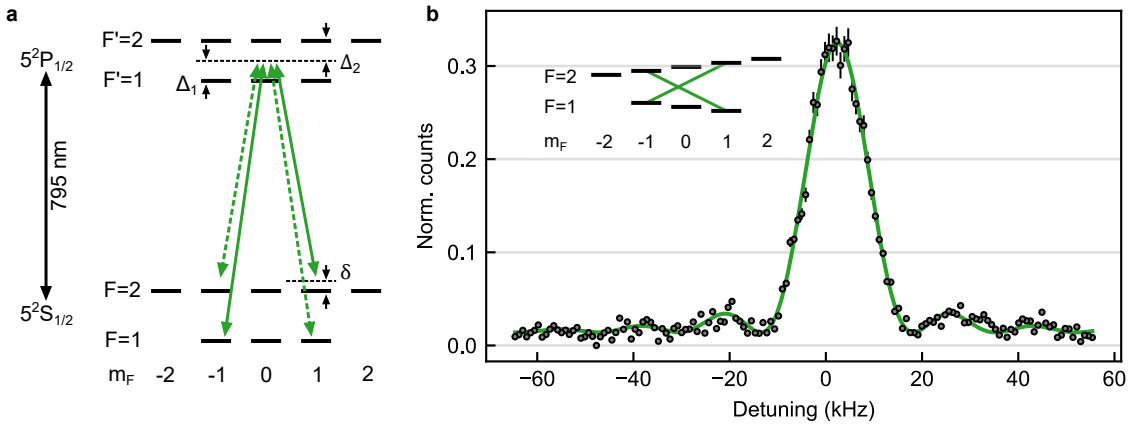

Figure 2.13.: 795nm Raman laser. (**a**) Atomic level scheme illustrating the Raman transition on the D_1 line. Both legs of the Raman laser are tuned in between the $F' = 1$ and $F' = 2$ hyperfine manifolds of the excited states with equal and opposite detunings $\Delta_1 = -\Delta_2 \approx 400\,\text{kHz}$. (**b**) Spectrum as a function of the two-photon detuning δ. The peak in the centre represents both transitions $|1, \pm 1\rangle \leftrightarrow |2, \mp 1\rangle$ as shown in the level scheme inset.

the $F' = 1$ and negative for the $F' = 2$ hyperfine states of the $5^2P_{1/2}$ excited state (Fig. 2.13a). In this way the interference becomes constructive, as the transition amplitudes acquire the same sign. The constructive interference comes at the expense of an increased spontaneous scattering rate, since the detuning Δ is only about 400 MHz.

For this reason, we have taken a different approach to the setup shown in Fig. 2.10a. For the 790 nm Raman setup, a substantial fraction of the overall optical power populates the carrier and the left sideband of the EOM, both of which do not contribute to the targeted two-photon Raman process. Although this fraction of the optical power is 'wasted', it does not lead to a significant amount of spontaneous scattering due to the large detuning Δ. However, for the 795 nm Raman laser, Δ is much smaller, so the fraction of the light that does not contribute to the process would degrade the π pulse fidelity. We therefore generate the light from two separate lasers and simply combine them on an NPBS, such that only the two frequencies needed are present in the spectrum. A spectrum of the Raman transition can be seen in Fig. 2.13b.

2.2.4. Atom readout

A readout of the atomic qubit can in principle be performed efficiently using fluorescence state detection enabled by the optical cavity. To do so, the cavity is tuned to the $\left|5^2S_{1/2}, F = 2\right\rangle \leftrightarrow \left|5^2P_{3/2}, F' = 3\right\rangle$ transition. A laser beam resonant or near-resonant with this transition is then applied to the atom such that it scatters photons into the cavity mode, when the atom occupies the $F = 2$ manifold. This enables deterministic and high-fidelity discrimination between the two hyperfine manifolds (see for example Ref. [80]).

Unfortunately, this tool is not available at the same time as the vSTIRAP mechanism, as the cavity resonance needs to be tuned to a different pair of levels in the two cases. Since we require the emission capability for generating photonic graph states, we have developed a different scheme to read out the atomic qubit, sketched in Fig. 2.14. Here, we transfer the atomic qubit from $|1, \pm 1\rangle$ to $|2, \pm 2\rangle$ and produce a photon which is detected in the R/L basis. As the emitted polarisation is correlated with the atomic state, we can infer the atomic state before emission of the photon. The measurement basis can be set

simply by beginning this procedure with an appropriate qubit rotation using the 790 nm Raman laser (see 2.2.3). For example, a $\pi/2$ pulse with the correct phase realises an X basis measurement.

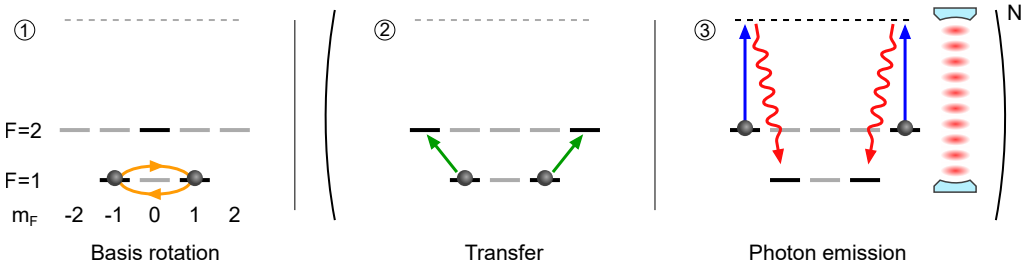

Figure 2.14.: Atomic qubit readout. First, the basis is set with a corresponding Raman rotation. Subsequently, the qubit is transferred to $|2, \pm 2\rangle$. Lastly, a photon is generated using the vSTIRAP process. Steps (2) and (3) are repeated N times to increase the efficiency.

The advantage of this scheme is that the photon emission brings the atom back to the initial state, such that the procedure can be repeated, in principle indefinitely. For a large number of iterations, the state readout becomes quasi-deterministic. With the single-photon efficiency η, the success probability p_s of having detected a photon after N attempts is

$$p_s(N) = 1 - (1 - \eta)^N \ , \tag{2.7}$$

which converges to 1 for large N.

In practice, the choice of N represents a compromise between efficiency and fidelity, since repeating many times also slightly increases the chance of errors occurring (see for instance chapter 4.4). In most scenarios, we prioritise fidelity, which means a relatively low number of N, typically ranging between 3 and 5. Nonetheless, this approach yields a significant enhancement in data rate, as indicated by equation 2.7.

2.2.5. Atom-photon entanglement

In an earlier section of this chapter, we have introduced the vSTIRAP photon emission process. We treated this mechanism in the context of a simple Λ-type system, where the population is coherently transferred from one ground state to another by emitting a photon into the cavity mode. When applying this scheme to the two ground states of rubidium, the atomic state and the photonic mode have more degrees of freedom as in the simple case described earlier. For example, the two atomic hyperfine levels of the atom split up into a total of eight Zeeman sublevels in the presence of a magnetic field. Furthermore, the emitted photon has two polarisation modes available. Finally, the atomic and photonic spin degrees of freedom are mutually constrained by the conservation of angular momentum. This ultimately gives rise to entanglement between the atomic state and the polarisation of the emitted photon.

The underlying mechanism can be easily understood by looking at Fig. 2.15, illustrating the creation of an atom-photon entangled pair. The atom is first prepared in the $m_F = 0$ state of the $F = 2$ hyperfine level. Subsequently, a vSTIRAP control pulse causes the emission of a photon. Due to the geometry of the system, where the magnetic field is aligned with the cavity axis, the photon can only be emitted via the σ^+/σ^- paths, with the atom undergoing a transition to either $|\uparrow\rangle = |1, +1\rangle$ or $|\downarrow\rangle = |1, -1\rangle$. The presence

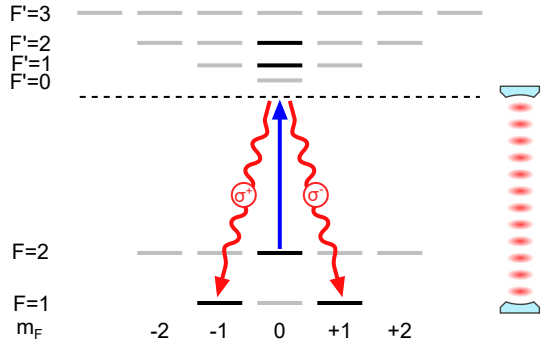

Figure 2.15: Atom-photon entanglement. The atom is initialised in $|2,0\rangle$ before a photon is generated via the vSTIRAP process. There are two emission paths, corresponding to σ^+ and σ^- polarisation. Atom-photon entanglement arises from the conservation of total angular momentum.

of both paths results in an atom-photon entangled state of the form

$$|\psi_{\mathrm{AP}}\rangle = \frac{1}{\sqrt{2}}\left(|\uparrow L\rangle - |\downarrow R\rangle\right), \tag{2.8}$$

which is equivalent to a $|\Psi^-\rangle$ Bell state. Here, we have written the photon in terms of the right- and left-hand circular polarisation states, $|R\rangle$ and $|L\rangle$. The relative minus sign is due to the Clebsch-Gordan coefficients associated with the two emission paths.

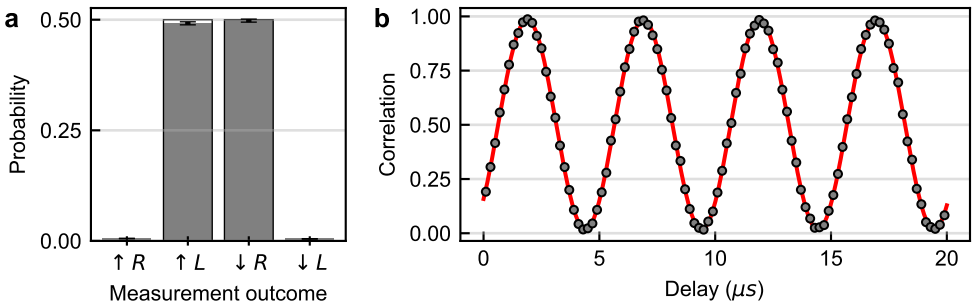

Figure 2.16.: Atom-photon entanglement. (**a**) Eigenbasis (Z basis) measurement of the spin-photon entangled pair. A high degree of correlation is observed in the probability of the two-qubit measurement outcomes $\uparrow R$, $\uparrow L$, $\downarrow R$ and $\downarrow L$. (**b**) Cross-basis measurement of the entangled pair. After an X basis measurement of the photon, the atomic qubit is read out after performing a $\pi/2$ pulse with variable delay. The high visibility indicates a large coherence of the entangled pair.

Fig. 2.16 shows the experimental data demonstrating the entanglement. In Fig. 2.16a we plot the probability of each of the four possible outcomes when measuring both qubits in the eigenbasis (Z basis), i.e. $|\uparrow / \downarrow\rangle$ for the atom and $|R/L\rangle$ for the photon. We observe strong atom-photon correlations, as the $|\uparrow L\rangle$ and $|\downarrow R\rangle$ components appear to be the most dominant contributions, with a combined population of 0.9898(5). To show that these two components are in a coherent superposition, we measure the photon in the X basis and the atom in a basis that lies on the equator of the Bloch sphere. To this end, we apply a $\pi/2$ pulse to the atomic qubit with a variable delay using the Raman pulse sequence introduced in chapter 2.2.3. The delay has the effect that the atomic qubit evolves and picks up a phase. In the rotating frame of the atomic qubit, this is equivalent to a periodically rotating detection basis as set by the phase of the Raman beams. Finally, we measure the atomic state and plot the atom-photon correlations as a function of the variable time delay. As expected we observe a sinusoidal behaviour of the observed quantity with a visibility of 0.966(3) as shown in Fig. 2.16b. From the population terms $|\uparrow L\rangle$ and $|\downarrow R\rangle$ and their coherence given by the oscillation visibility, we can infer a fidelity of 0.978(1) with respect to the ideal state as given by equation 2.8.

2.2.6. Extending atomic coherence via magnetic-field feedforward

One of the primary challenges for virtually all quantum technology platforms is to extend the qubit coherence time beyond the duration required to execute a particular protocol. Coherence time emerges as a particularly crucial metric in the realm of quantum repeaters [50, 88], where a quantum state has to be stored in quantum memories until entanglement is established across all segments of the communication link. The performance of a repeater station crucially depends on the coherence time of its memories. However, the importance of coherence time extends beyond the specific application of the quantum repeater. In fact, most quantum technologies that rely on matter qubits suffer to some extent from the effects of decoherence. A variety of techniques have been developed to combat the detrimental effects of a finite coherence time. The preferred technique depends largely on the specific sources of decoherence present in a given system. For example, if decoherence is mostly caused by magnetic field fluctuations, it may be beneficial to surround the apparatus with a layer of material, such as mu-metal, that shields the qubits from these fluctuations. The advantage of such a passive approach is that it does not require any active components, which are potential points of failure. However, an active stabilisation mechanism can be very effective in reducing magnetic field noise. The challenge is to position a magnetic field sensor as close to the setup as possible, such that its measurement accurately represents the field experienced by the qubits. The magnetic field measurement is then fed into a feedback loop, which acts on a pair of compensation coils in order to cancel the magnetic field fluctuations.

In our experiment, we have implemented a variation of this principle that eliminates the need for a magnetic field sensor. It was inspired by an exchange with the Saarbrücken group led by Prof. Jürgen Eschner, who have implemented this technique in their experiment [103]. Their scheme is active in the sense that an actuation coil is used for reducing the fluctuations of the magnetic field. However, in contrast to a feedback loop, which counteracts the momentary change of the magnetic field, this technique anticipates the future evolution of the magnetic field. Hence, we refer to this approach as 'feedforward' (FF). This mechanism applies very effectively to noise contributions that are periodic in time. Indeed, a common source of noise is the electronic equipment in physics laboratories. Most devices are powered by the 50 Hz alternating current (AC) from the mains supply line and therefore contain magnetically active components such as transformers. We have devoted great effort to identifying such devices and placing them as far away from the vacuum chamber as possible. Nonetheless, a measurement with a magnetic field sensor still shows the presence of periodic noise, with the most dominant frequency contributions being 50 Hz and its odd higher harmonics (150 Hz, 250 Hz, 350 Hz, etc.). These can be efficiently cancelled by applying an equal and opposite signal to a pair of compensation coils.

Implementation

The experimental implementation and the mode of operation are outlined in Fig. 2.17. The central hardware component is a Red Pitaya microcontroller with an analogue output serving as an arbitrary waveform generator (Fig. 2.17a). The latter directly delivers the compensation current to the magnetic coil. The compensation signal needs to be phase-locked with the 50 Hz noise. To do this, the Red Pitaya receives a reference signal in form of a square pulse on one of its digital inputs, triggered by the rising edge of the 230 V AC signal from the power outlet. Fig. 2.17b displays an exemplified time trace of the magnetic field in the experiment. The uncompensated signal (no FF) contains a large

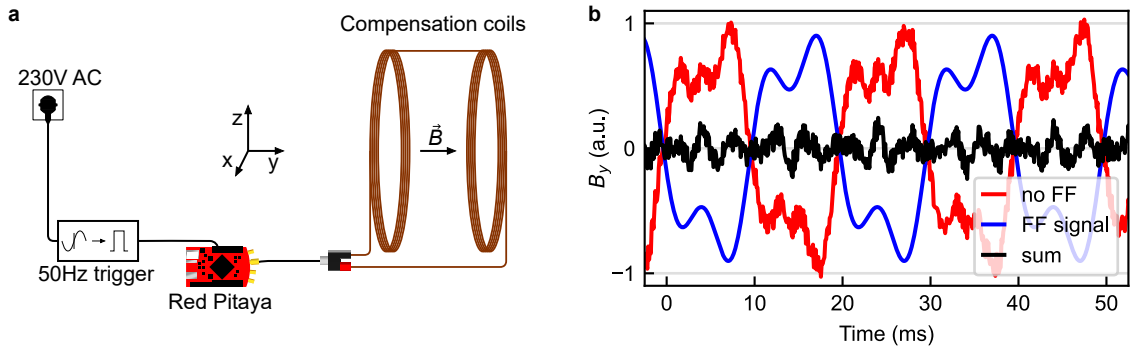

Figure 2.17.: Experimental scheme for magnetic-field feedforward. (**a**) A pair of magnetic coils is arranged in Helmholtz configuration. The coils are driven by the analogue output of a Red Pitaya microcontroller. The latter outputs a programmable waveform triggered by a digital input. The trigger signal is obtained from a circuit that converts the 230 V AC mains signal into a series of square pulses. (**b**) Illustration of the FF mechanism. The plot shows an exemplary time trace of the different magnetic field contributions along the y-axis. The uncompensated noise (red) has a large contribution at 50 Hz and its higher harmonics. The field generated by the compensation coils (blue), which is typically composed of only 50 Hz and 150 Hz, is tuned out of phase with the noise. This reduces the overall noise significantly (black). Nonperiodic noise and components at other frequencies are not captured by this mechanism.

contribution at 50 Hz (20 ms period), some of its higher harmonics and some nonperiodic noise. The field generated by the compensation coils (FF signal) cancels the two most dominant contributions in the noise spectrum. In the example shown in Fig. 2.17b as well as in our experiment, these are the 50 Hz and 150 Hz components.

To find the optimal output waveform, we run an optimisation procedure that returns the optimal phase and amplitude for each of the frequency components considered. The basic idea is to prepare the atom in a superposition of the two Zeeman states $|1, \pm 1\rangle$. The state will precess at twice the Larmor frequency (see for instance Fig. 2.16). We then measure the fringe contrast after about 500 µs, where the state has partly decohered. The parameters of the compensation waveform are then progressively optimised to maximise the contrast.

We start by setting the waveform to a sine wave with a frequency of 50 Hz and an amplitude on the order of what we expect for the optimised waveform. The choice of this initial guess is not crucial at this point. We then scan the phase of the signal over a full 2π interval. If noise at 50 Hz is present, the observed fringe contrast will vary as a function of the phase, with a maximum appearing where the compensation signal is perfectly out of phase with the noise (Fig. 2.18a). After fixing this phase value, we vary the amplitude and again find a maximum for the fringe visibility (Fig. 2.18b). This procedure can be repeated in the same way for other frequency components if an improvement in fringe visibility is observed. Fig. 2.18c and d show the same measurement for 150 Hz. It can clearly be seen that for 150 Hz the maximum fringe contrast is reached for a much smaller output amplitude than for 50 Hz. Moreover, the overall improvement is much greater for 50 Hz. From this we conclude that in our laboratory the most dominant noise contribution is that at 50 Hz, while the 150 Hz component plays a minor role. For frequencies of 250 Hz and above, as well as all even harmonics (100 Hz, 200 Hz, etc.), we do not observe any noticeable improvement. Therefore, we typically only compensate the fundamental mode at 50 Hz and the 150 Hz higher harmonic.

Fig. 2.19 shows the improvement achieved with the FF by comparing the coherence

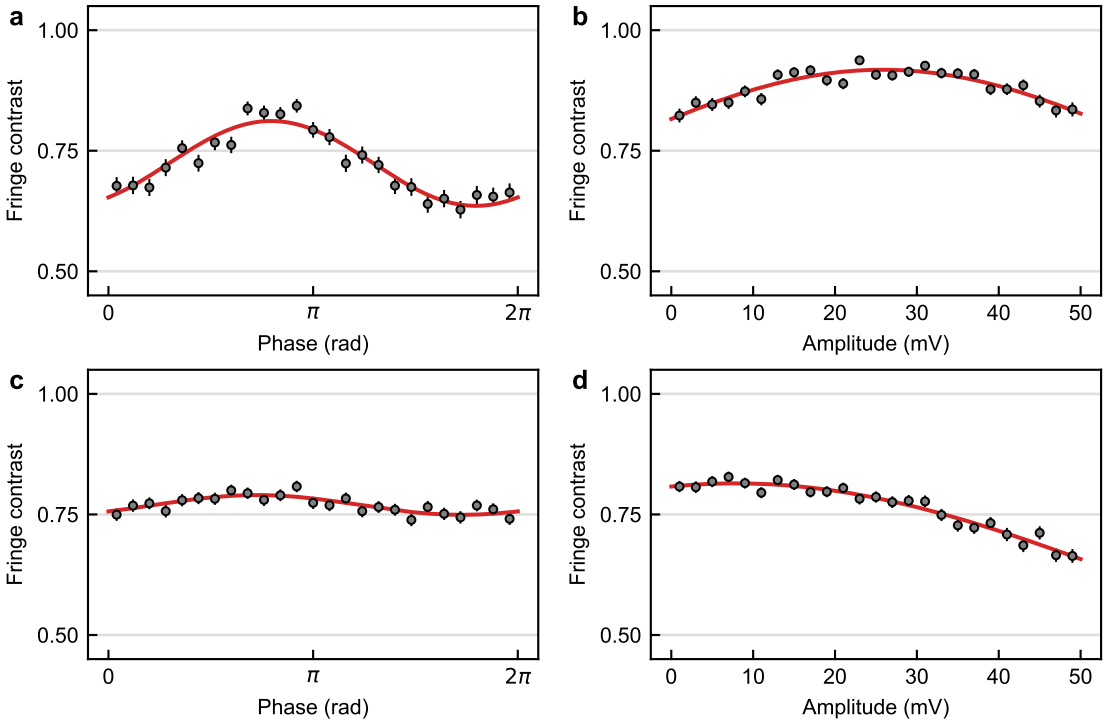

Figure 2.18.: Phase and amplitude sweeps for FF optimisation. Phase (**a**) and amplitude (**b**) sweep for the 50 Hz magnetic field component. Phase and amplitude correspond to the output signal of the Red Pitaya. (**c/d**) Same as (**a**) and (**b**), but for the 150 Hz component.

time both without (a) and with (b) the magnetic-field FF. Without FF the intrinsic coherence time of the atomic qubit states $|1, \pm 1\rangle$ is 633(8) µs. This number is extended to 1277(24) µs when enabling the FF compensation coil, thus doubling the coherence time. Note that this only includes the 50 Hz and 150 Hz frequency components along the y-axis, i.e. the direction of the magnetic bias field. While magnetic field noise on the x- and z-axes is expected to play a minor role compared to the more sensitive y-axis, we believe that further improvements could be attained by compensating the remaining two axes.

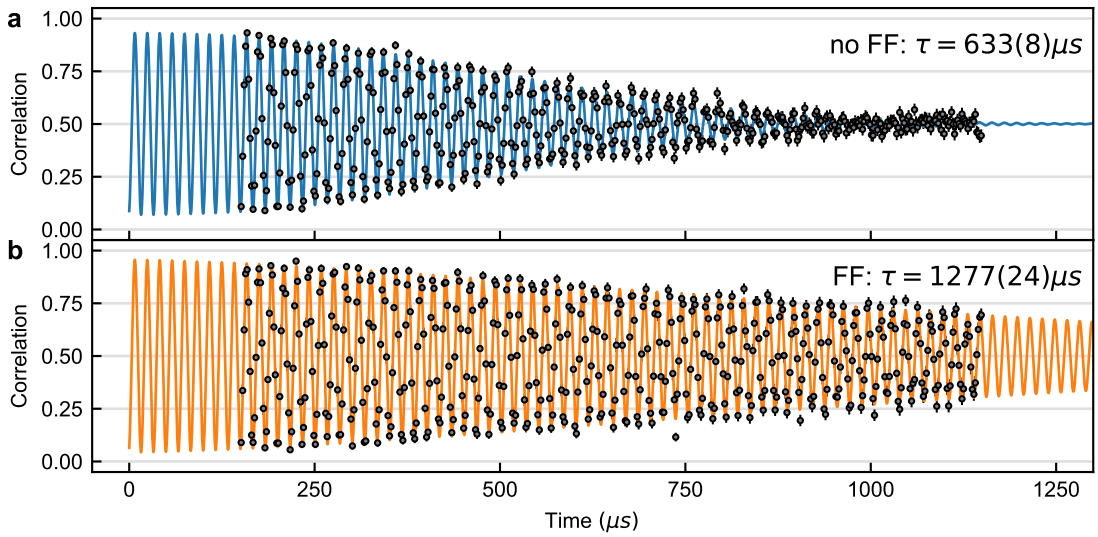

Figure 2.19.: Extended coherence time via magnetic feedforward (FF). Coherence time on the qubit states $|1, \pm 1\rangle$ without (**a**) and with (**b**) FF.

3. Graph state entanglement

Since the central topic of this thesis is the preparation of photonic graph states, this chapter is devoted to introducing the theoretical foundations of this subject. The first part of the chapter will lay the necessary groundwork and review the basic principles of entanglement. Subsequently, the more specialised concept of graph states is explained. Following that, we describe some important quantum information protocols that heavily rely on graph states as a resource. Finally, we will introduce a method for certifying graph state entanglement experimentally based on entanglement witnesses.

3.1. Preliminaries

We start with the basic principles of qubits and entanglement. The underlying concepts are introduced using illustrative examples, rather than in a complete and mathematically rigorous manner. An in-depth treatment of the topic can be found in standard quantum information textbooks (see e.g. [104])

3.1.1. Qubits

In quantum information processing, a **quantum bit** or **qubit** forms the smallest piece of quantum information. The state of a qubit $|\psi\rangle$ is typically expressed as a linear combination of orthonormal basis states, $|0\rangle$ and $|1\rangle$:

$$|\psi\rangle = \alpha\,|0\rangle + \beta\,|1\rangle\ , \tag{3.1}$$

where α and β are complex numbers fulfilling the condition $|\alpha|^2 + |\beta|^2 = 1$. In vector notation the basis states are expressed as $|0\rangle = \begin{pmatrix}1\\0\end{pmatrix}$ and $|1\rangle = \begin{pmatrix}0\\1\end{pmatrix}$. They are also eigenstates to the Pauli Z operator. In matrix notation the **Pauli operators** are defined as

$$X = \begin{pmatrix}0 & 1\\1 & 0\end{pmatrix}\ , \qquad Y = \begin{pmatrix}0 & -i\\i & 0\end{pmatrix}\ , \qquad Z = \begin{pmatrix}1 & 0\\0 & -1\end{pmatrix}\ . \tag{3.2}$$

The X and Y operators possess the eigenvectors $|\pm\rangle \equiv (|0\rangle \pm |1\rangle)/\sqrt{2}$ and $|\pm i\rangle \equiv (|0\rangle \pm i\,|1\rangle)/\sqrt{2}$, respectively, with $X\,|\pm\rangle = \pm\,|\pm\rangle$ and $Y\,|\pm i\rangle = \pm\,|\pm i\rangle$.

In the terminology used by physicists, a qubit is not only a unit of information, but also frequently refers to the physical entity that *carries* the qubit. Such a system may be a quantum particle, such as a trapped ion or atom, where two of its internal energy levels are chosen as the qubit states $|0\rangle$ and $|1\rangle$.

3.1.2. Separability and entanglement

States of multiple qubits are mathematically described using the tensor product. Consider qubits A and B associated with Hilbert spaces $\mathcal{H}_A$ and $\mathcal{H}_B$. Then the combined two-qubit state is written as a vector in the Hilbert space $\mathcal{H}_{AB} = \mathcal{H}_A \otimes \mathcal{H}_B$. A state in $\mathcal{H}_{AB}$ is called **separable** or a **product state** if it can be expressed in the form

$$|\Phi_{AB}\rangle = |\psi_A\rangle \otimes |\psi_B\rangle\ . \tag{3.3}$$

Quantum states that are not separable are called **entangled**. In a system composed of two qubits, the states defined as

$$\left|\Psi^{\pm}\right\rangle = (|01\rangle \pm |10\rangle)/\sqrt{2}\,, \tag{3.4}$$

$$\left|\Phi^{\pm}\right\rangle = (|00\rangle \pm |11\rangle)/\sqrt{2} \tag{3.5}$$

are known as Bell states. These are maximally entangled and form an orthonormal basis of the two-qubit Hilbert space.

3.1.3. Biseparability and genuine multipartite entanglement

The concept of entanglement is easily extended beyond the case of bipartite systems. For example, a system composed of three particles is in a (fully) separable state if and only if it can be written as

$$|\Psi_{ABC}\rangle = |\psi_A\rangle \otimes |\psi_B\rangle \otimes |\psi_C\rangle \ . \tag{3.6}$$

States that are separable with respect to a partition into two subsystems are called **biseparable**. For example, the state

$$|\Psi_{ABC}\rangle = \frac{1}{2}\big(|000\rangle + |110\rangle\big) = \left|\Phi^{+}\right\rangle_{AB} \otimes |0\rangle_C \tag{3.7}$$

is not fully separable, but biseparable under the $AB|C$ partition. It can be decomposed into a product state of two subsystems, one of which ($|\Phi^{+}\rangle_{AB}$) is entangled. A composite system in which no such decomposition exists, i.e. a system that is not biseparable, exhibits **genuine multipartite entanglement**. For example, the state

$$|\mathrm{GHZ}_3\rangle = \frac{1}{\sqrt{2}}\left(|000\rangle + |111\rangle\right) \tag{3.8}$$

cannot be written as the product of two subsystems. It is therefore a genuinely multipartite entangled state, known as Greenberger-Horne-Zeilinger (GHZ) state [105].

3.2. Graph states

In the last section we introduced the general concept of entanglement. However, the focus of this thesis lies on a particular subclass of entangled states called graph states. The framework of graph states is critical for understanding the experimental results presented in chapters 4 and 5, which is why the subsequent section gives a brief introduction to the topic, including the formal definition, several instructive examples and important properties.

3.2.1. Definition

There are two equivalent ways in which graph states can be defined. First, consider a graph $G = (V,E)$, consisting of vertices V representing the qubits and edges E in between them (see Fig. 3.1). The state associated with G is the multi-qubit state obtained by initialising all qubits in $|+\rangle = (|0\rangle + |1\rangle)/\sqrt{2}$ and performing controlled Z (CZ) gates between qubits that are connected by an edge. This can be written as

$$|\Psi_{\mathrm{G}}\rangle = \prod_{(a,b)\in E} CZ^{(a,b)}\,|+\rangle^{\otimes V} \ . \tag{3.9}$$

Here, $CZ^{(a,b)}$ denotes a CZ gate between qubits a and b. The product runs over all pairs of qubits (a,b) that are connected by an edge.

The second definition makes use of the stabiliser formalism [106]. A graph state is thereby defined by a set of stabiliser operators

$$S_i = X_i \prod_{j \in N(i)} Z_j \,. \tag{3.10}$$

In the product, $N(i)$ denotes the neighbourhood of qubit i, i.e. all qubits that share an edge with qubit i. The quantum state $|\Psi_\mathrm{G}\rangle$ which is a simultaneous eigenstate to all stabilisers, that is

$$S_i \,|\Psi_\mathrm{G}\rangle = |\Psi_\mathrm{G}\rangle \quad \forall i \in V \,, \tag{3.11}$$

is by definition the graph state that corresponds to a particular graph.

Both ways of defining graph states (equations 3.9 and 3.11) are equivalent to one another and may be used interchangeably.

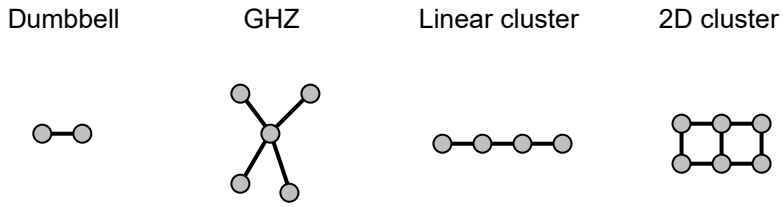

Figure 3.1.: Examples for common types of graph states. Dumbbell, GHZ state, linear cluster state and 2D cluster state.

Example 1: Dumbbell

The simplest example of a graph state is a state consisting of two entangled qubits, whose corresponding graph consists of two vertices and an edge connecting them (Fig. 3.1). Due to its visual appearance we will refer to it as 'dumbbell'. Its explicit expression reads

$$|\mathrm{DB}\rangle = \frac{1}{\sqrt{2}}\big(|{+}0\rangle + |{-}1\rangle\big) \,. \tag{3.12}$$

The stabilisers, as defined by equation 3.10, are X_1Z_2 and Z_1X_2. It can be easily verified that $|\mathrm{DB}\rangle$ is indeed a simultaneous eigenstate to both of these stabilisers. The dumbbell state is locally equivalent to the four Bell states (equation 3.4 and 3.5), meaning that it can be transformed to any of the Bell states and vice versa, using a suitable local unitary transformation. For example, applying a Hadamard gate[1] to the first qubit of the state $|\Phi^+\rangle$ gives the dumbbell graph state. Similarly, a Bell state can also be transformed into the dumbbell state using global unitaries, i.e. applying the same transformation to both qubits simultaneously. As this transformation is used in chapter 5, we will derive this result in the following.

A $-\pi/4$ rotation applied to the $|\Psi^+\rangle$ Bell state gives

$$\frac{1}{\sqrt{2}}\Big[-2\cos\Big(-\frac{\pi}{8}\Big)\sin\Big(-\frac{\pi}{8}\Big)\left(|00\rangle - |11\rangle\right) + \Big(\cos^2\Big(-\frac{\pi}{8}\Big) - \sin^2\Big(-\frac{\pi}{8}\Big)\Big)\left(|01\rangle + |10\rangle\right)\Big] \,, \tag{3.13}$$

[1] The Hadamard gate transforms the computational basis states into the superposition states $|\pm\rangle$, i.e. $H\,|0\rangle = |+\rangle$ and $H\,|1\rangle = |-\rangle$.

where we have used the transformations

$$|0\rangle \to \cos\left(\frac{\theta}{2}\right)|0\rangle + \sin\left(\frac{\theta}{2}\right)|1\rangle \,, \tag{3.14}$$

$$|1\rangle \to -\sin\left(\frac{\theta}{2}\right)|0\rangle + \cos\left(\frac{\theta}{2}\right)|1\rangle \,, \tag{3.15}$$

with $\theta = -\pi/4$. We use the trigonometric identities

$$\cos\left(\frac{\pi}{8}\right) = \frac{\sqrt{2+\sqrt{2}}}{2} \,, \tag{3.16}$$

$$\sin\left(\frac{\pi}{8}\right) = \frac{\sqrt{2-\sqrt{2}}}{2} \,, \tag{3.17}$$

and substitute them into equation 3.13 to obtain

$$\frac{1}{2}\big(|00\rangle + |01\rangle + |10\rangle - |11\rangle\big) = \frac{1}{\sqrt{2}}\big(|{+}0\rangle + |{-}1\rangle\big) \,, \tag{3.18}$$

which is the dumbbell state $|\mathrm{DB}\rangle$.

Example 2: Greenberger-Horne-Zeilinger (GHZ) state

The GHZ state [105] is one of the most prominent examples of multipartite entangled states in general. A GHZ state of N particles is most commonly written in the form $(|0\rangle^{\otimes N} + |1\rangle^{\otimes N})/\sqrt{2}$. Strictly speaking, the above expression does not satisfy the eigenvalue equation in equation 3.11, but is locally equivalent to

$$|\mathrm{GHZ}_N\rangle = \frac{1}{\sqrt{2}}\big(|0\rangle\,|{+}\rangle^{\otimes(N-1)} + |1\rangle\,|{-}\rangle^{\otimes(N-1)}\big) \,, \tag{3.19}$$

which is the state satisfying the formal definition. As a specific example, a GHZ state of 3 qubits reads $(|0++\rangle + |1--\rangle)/\sqrt{2}$ and is an eigenstate to the stabilisers $X_1Z_2Z_3$, Z_1X_2 and Z_1X_3.

Example 3: Linear cluster state

Linear or one-dimensional (1D) cluster states are identified in the graphical notation by qubits arranged in a straight line. For example, the explicit expression for a three-qubit linear cluster state is

$$|\mathrm{LC}_3\rangle = \frac{1}{\sqrt{2}}\big(|{+}0{+}\rangle + |{-}1{-}\rangle\big) \tag{3.20}$$

and its stabilisers are X_1Z_2, $Z_1X_2Z_3$ and Z_2X_3. Note that for three qubits, the linear cluster state is exactly equivalent to a GHZ state (up to index exchange). A four qubit linear cluster state

$$|\mathrm{LC}_4\rangle = \frac{1}{2}\big(|0+0{+}\rangle + |0-1{-}\rangle + |1-0{+}\rangle + |1+1{-}\rangle\big) \,, \tag{3.21}$$

on the other hand, cannot be transformed into a GHZ state via local unitary transformations. The same holds for any cluster state containing more than four qubits.

3.2.2. Redundantly encoded qubits

The notion of 'redundantly encoded qubits' is an important and useful tool in the context of graph states. This concept was introduced in Ref. [107]. The basic idea is that a logical qubit, i.e. a vertex in a graph, can be encoded by multiple physical qubits. For example, we can interpret an N-qubit GHZ state as a single logical qubit, that is

$$|+\rangle_L = |\mathrm{GHZ}_N\rangle = \frac{1}{\sqrt{2}}\left(|0\rangle^{\otimes N} + |1\rangle^{\otimes N}\right), \tag{3.22}$$

where $|0\rangle_L \equiv |0\rangle^{\otimes N}$ and $|1\rangle_L \equiv |1\rangle^{\otimes N}$ define the logical basis vectors. Following the convention of previous works [107, 108], we express the redundantly encoded vertex as a large circle containing a number of smaller circles, which in turn represent the physical qubits. The graph notation of the four-qubit GHZ state can be found in Fig. 3.2 (top left). The generalisation of this principle naturally leads to the concept of 'redundantly encoded graph states', in which each vertex of a graph may contain one or multiple physical qubits. A formal definition equivalent to equation 3.9 can be found in Ref. [108].

An important property of redundantly encoded vertices is that any of the physical qubits within them can be converted into a separate qubit vertex by application of a Hadamard gate (see Fig. 3.2). It is precisely this property that gives rise to the local equivalence between the Bell states and the dumbbell state: $|\Phi^+\rangle = |+\rangle_L$ in the basis $\{|00\rangle, |11\rangle\}$ transforms to $|\mathrm{DB}\rangle$ under a local Hadamard gate on one of the physical qubits. It further explains the connection between a GHZ state expressed as $(|00...0\rangle + |11...1\rangle)/\sqrt{2}$ and the expression that obeys the stabiliser eigenvalue equations (equation 3.8). The latter corresponds to a star-shaped graph, commonly associated with a GHZ state.

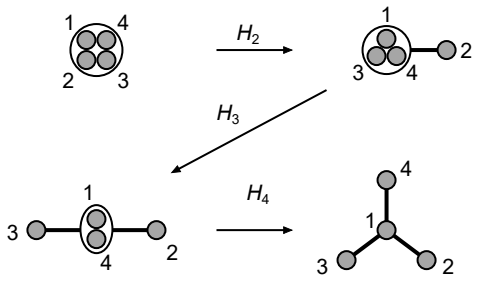

Figure 3.2: Redundantly encoded qubits. A GHZ state can be expressed as a single vertex, representing one logical qubit (top left). A Hadamard gate H_i applied to any qubit i results in it being 'pushed out', such that it forms a separate vertex. Performing a Hadamard operation on all but one qubit results in the star-shaped graph (bottom right).

3.2.3. Pauli measurements

Measuring individual qubits in a graph state reshapes the connectivity of the graph in a particular fashion, which is important for understanding how measurement-based quantum information processing works. Consider a linear cluster state as depicted in Fig. 3.3. A Z measurement (a) on one of the qubits removes it from the graph by cutting all the connections attached to it. The rest of the graph remains unaffected by this operation. A Y measurement (b), on the other hand, also removes the qubit, but connects the neighbouring graph vertices. When measuring the qubit in the X basis (c), the adjacent qubits are merged into a common vertex, forming a redundantly encoded qubit, as introduced earlier. Lastly, two adjacent X basis measurements (d) directly connect the neighbouring vertices of the measured qubits.

It is worth noting that the state obtained after the measurement may or may not acquire a phase, depending on the measurement outcome. Therefore, the graphical notation of

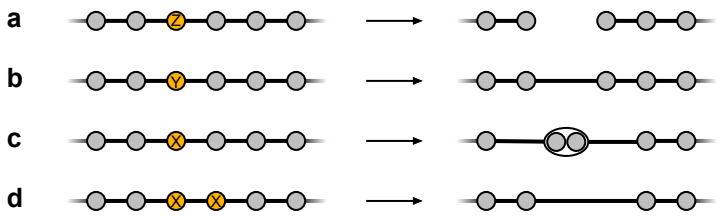

Figure 3.3.: Measurements on a linear cluster state. When a Pauli measurement is performed on one of the qubit vertices (orange), the respective qubit is removed from the graph, whose connectivity is modified as a consequence.

the processes in Fig. 3.3 implies that this phase is compensated, either by local unitaries or by modifying the measurement basis of the final qubit readout.

The effect of Pauli measurements on the topology of the graph has crucial consequences for quantum information processing. It allows a direct connection to be established between any two qubits within a graph state, simply by measuring the remaining qubits in specific bases. This property plays a vital role in the protocols discussed in the following section.

3.3. Measurement-based quantum information processing

As a motivation for the upcoming experimental chapters, the section that follows discusses the practical utility of graph states in QIP. The common scheme involves using entangled graph states as a resource and processing them with single-qubit measurements. For this reason, such protocols have become known as measurement-based quantum computation (MBQC) or communication. A comprehensive description of the topic would go beyond the scope of this chapter. For a more extensive discussion, readers are referred to Refs. [109–111].

Instead, we will focus on two specific examples, namely one-way quantum computation and the all-photonic quantum repeater. A third protocol known as the one-way quantum repeater will be discussed in chapter 5 along with the experimental results on tree graph states.

3.3.1. One-way quantum computation

One-way quantum computation, as proposed by Raussendorf and Briegel [54], represents the most prominent example of MBQC. Other examples include, for instance, the teleportation-based model [112]. However, the terms measurement-based quantum computation and one-way quantum computation are to some extent used interchangeably in the literature.

The concept of one-way quantum computation is illustrated in Fig. 3.4. It relies on a 2D cluster state $|\mathcal{C}_{2D}\rangle$ as a resource state. Here the graph vertices are arranged in a rectangular two-dimensional grid. The actual computation consists of a sequence of single-qubit measurements, which leaves a subset of the qubits in the desired output state.

At the beginning, qubits that are not needed for the computation (shown in orange) are measured in the Z basis, which effectively disentangles them from the cluster state (see Fig. 3.3). For didactic purposes, we consider this to take place prior to the actual computation, although the specific order in which this is done is not critical. Subsequently, the remaining qubits (blue) are measured in the $X-Y$ plane, e.g. in the basis given by

$(|0\rangle \pm \exp(i\alpha)\,|1\rangle)/\sqrt{2}$. Here, the parameter α defines the angle on the equator of the Bloch sphere. The measurements are executed in rounds on each column of the cluster, moving from left to right. The measurement outcomes obtained in each round determine the measurement basis of the subsequent round. In doing so, one can encode logical qubits on the horizontally oriented lines of the cluster state. A series of measurements with the appropriately chosen angles α realises an arbitrary single-qubit rotation. Two-qubit gates are implemented through vertical lines. In the example shown in Fig. 3.4, measuring the two qubits forming a vertical connection in the X basis will create a direct link between two horizontal lines (Fig. 3.3d).

The column-wise measurement of the cluster state proceeds until reaching the final column of qubits. The computational result is then obtained from a readout of these remaining qubits.

The single- and two-qubit gates as described above form a universal set, thereby enabling quantum computation. In fact, the one-way model is equivalent to the circuit model [113, 114], in the sense that any quantum circuit can be imprinted on a sufficiently large 2D cluster state. Fig. 3.4b shows an example of a quantum circuit, corresponding to the cluster state computation presented in Fig. 3.4a.

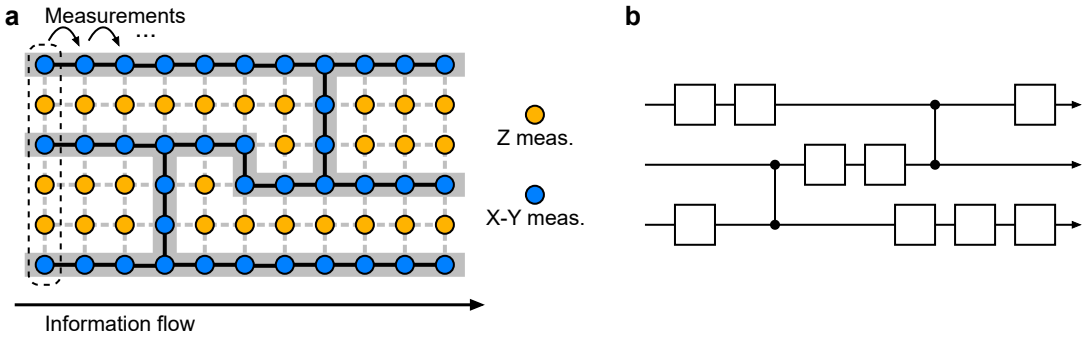

Figure 3.4.: One-way quantum computation. **(a)** A 2D cluster state serves as the resource. As defined by the algorithm, the qubits are either measured in the Z basis or the $X-Y$ plane. The computation is executed in rounds of measurements, moving column-wise from left to right. (**b**) Exemplary illustration of the quantum circuit corresponding to the computation shown in **(a)**. The boxes denote single-qubit unitary gates, vertical lines represent CZ gates.

3.3.2. All-photonic quantum repeater

Graph states also extend into the realm of quantum communication. A famous example of such a scheme is the all-photonic quantum repeater proposed in Ref. [55]. The underlying resource state is known as repeater graph state (RGS). In addition to single-qubit measurements, the protocol relies on Bell state measurements between pairs of photonic qubits. The achieved improvement in the scaling of the rate as a function of distance bears a strong resemblance to conventional repeaters [50]. However, this result is obtained without the need for quantum memories.

The basic principle is illustrated in Fig. 3.5. The structure of the repeater graph state consists of an inner layer of qubits with all-to-all connections. Each of these inner layer qubits carries one additional 'leaf' qubit, i.e. a qubit with only one connection. The inner layer qubits with their respective leaf qubits form a total of $2m$ arms. The resource state is drawn in Fig. 3.5 for the specific case $m = 3$.

In order to establish entanglement between two parties, Alice and Bob, a total of n RGS copies are prepared along the communication link. Bell state measurements (BSM)

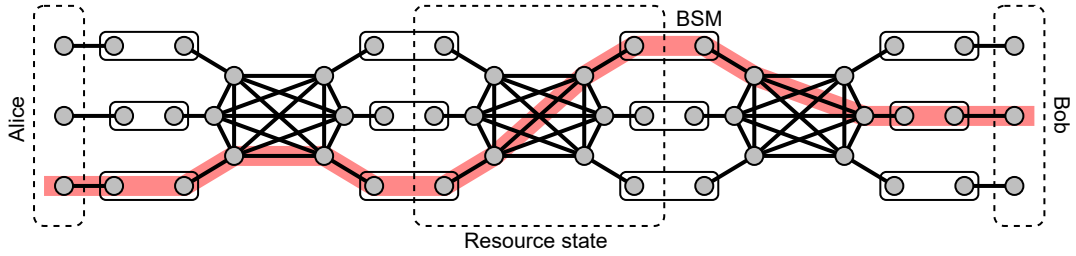

Figure 3.5.: All-photonic quantum repeater. The protocol relies on repeater graph states as the entangled resource state. Bell state measurements (BSM) are performed between the left and right arms of the n copies of repeater graph states. If at least one BSM per neighbouring pair of RGS succeeds, entanglement is established between Alice and Bob, as highlighted by the red line.

are carried out between the left and right arms of two adjacent RGS. A successful BSM results in a direct connection between inner layer qubits of the two neighbouring RGS. Having multiple arms combined with the all-to-all connectivity on the inner layer provides redundancy that increases the probability of establishing entanglement between Alice and Bob. A direct connection between the two parties is formed (depicted in red), if at least one Bell measurement succeeds at each BSM location between two adjacent RGS. Qubits which are not part of this link are simply disentangled from the cluster state with a Z basis measurement.

Due to the redundancy provided by the resource states, the success probability of the protocol scales polynomially with distance. As mentioned before, the all-photonic quantum repeater does not rely on quantum memories, unlike the original proposal [50]. Additionally, the memory-based protocol requires a waiting period to accommodate classical communication between neighbouring nodes. The all-photonic version of the quantum repeater eliminates the need for this waiting time, in principle allowing for a faster repetition rate.

3.4. Entanglement witnesses and fidelity bounds

Before proceeding to the next chapters, we now address the methodology of certifying graph state entanglement experimentally. For systems consisting of only a few particles, quantum state tomography (QST) would be the preferred choice, since it allows to reconstruct the full density matrix. However, for even a moderate number of qubits, the Hilbert space dimension becomes so large that full QST requires an enormous number of measurements in different basis settings. In fact, the number of local measurement settings scales exponentially with the number of qubits, leading to impractical measurement times, even for qubit numbers well below 10. For example, QST for a four-particle state already requires 256 measurement settings [59]. As we will see in the subsequent experimental chapters, our goal is to detect entanglement of more than 10 qubits. It is immediately clear that QST would not be a suitable measure to achieve this. For fidelity estimation we therefore chose a technique that applies the concept of entanglement witnesses [115–120] to graph states. As we will see later, this greatly reduces the number of local measurement settings for fidelity estimation.

In general, an entanglement witness $\mathcal{W}$ is an operator whose expectation value is positive or zero for any separable state. Therefore, a negative expectation value implies that the measured state is entangled. One says that $\mathcal{W}$ detects entanglement for $\langle W \rangle \leq 0$. The

opposite direction is not necessarily true, i.e. not all states that are non-separable will give a negative expectation value of $\mathcal{W}$.

For the special case of graph states it has been shown [120, 121] that a suitable witness can be constructed using the projector of the target state, writing

$$\mathcal{W} = \frac{\mathbb{1}}{2} - |\Psi_G\rangle\langle\Psi_G| \,. \tag{3.23}$$

Here, $\mathbb{1}$ is the identity matrix and $|\Psi_G\rangle$ is an arbitrary graph state. One can immediately see that if the fidelity $\mathcal{F} = \mathrm{Tr}\{\rho\,|\Psi_G\rangle\langle\Psi_G|\}$ exceeds 1/2, then the expectation value of $\mathcal{W}$ is less than zero and ρ must be entangled. Therefore, obtaining $\langle\mathcal{W}\rangle < 0$ and $\mathcal{F} > 1/2$ are two equivalent ways of detecting entanglement.

In an experiment, one would have to decompose the projector into a sum of locally measurable operators, i.e. strings of Pauli operators. For graph states such a decomposition readily exists in terms of their stabiliser operators. In this case we can write the projector as

$$|\Psi_G\rangle\langle\Psi_G| = \prod_{i=1}^{N} \frac{1+S_i}{2} \,. \tag{3.24}$$

Multiplying out the above product gives a sum of terms consisting only of Pauli X and Z operators. However, the number of required measurement settings still scales exponentially with the system size and there is no advantage over full QST. We can greatly reduce the experimental overhead by neglecting certain terms in the expression for the projector. This is possible if we can divide the stabilisers into two sets a and b, each of which can be measured with a single local measurement setting M_a and M_b. If this condition is satisfied, we can write the projector as

$$|\Psi_G\rangle\langle\Psi_G| = \prod_{i\in a} \frac{1+S_i}{2} \cdot \prod_{j\in b} \frac{1+S_j}{2} \equiv G_a \cdot G_b = G_a + G_b - 1 + (1-G_a)(1-G_b) \,, \tag{3.25}$$

where we have expressed the product terms in the short hand notation G_a and G_b.

3.4.1. Fidelity lower bound

By construction, the terms G_a and G_b take the values 1 or 0, which implies that $(1 - G_a)(1 - G_b)$ is also either 1 or 0. We can therefore omit the last term in equation 3.25 and formulate the inequality

$$P \equiv G_a + G_b - 1 \leq |\Psi_G\rangle\langle\Psi_G| \,, \tag{3.26}$$

or similarly

$$\langle P\rangle \leq \mathrm{Tr}\{\rho\,|\Psi_G\rangle\langle\Psi_G|\} = \mathcal{F} \,. \tag{3.27}$$

We identify the quantity $\mathcal{F}_- \equiv \langle P\rangle$ as a fidelity lower bound that detects entanglement via the condition $\mathcal{F}_- > 0.5$, which is equivalent to $\mathcal{W} < 0$. Remarkably, this allows us to estimate the fidelity with only two local measurement settings, independent of the number of qubits. As mentioned above, the condition is that all stabilisers can be measured with these two measurement settings. The experimental analysis of the generated graph states presented in chapter 4 and 5 relies heavily on this lower bound.

3.4.2. Fidelity upper bound

In a similar way, we can use the decomposition of the projector in equation 3.25 to derive an upper bound to the fidelity. Unlike the lower bound, the upper bound does not allow us to certify genuine multipartite entanglement for a given state. Nonetheless, it provides a good complementary measure to the lower bound, since it narrows down the interval in which the fidelity lies. The following derivation is strongly based on the Methods section of Ref. [122].

Using the Cauchy-Schwarz inequality we have

$$\langle G_a G_b \rangle_\psi \leq \sqrt{\left\langle G_a G_a^\dagger \right\rangle_\psi \left\langle G_b^\dagger G_b \right\rangle_\psi} \tag{3.28}$$

for any pure state $|\psi\rangle$. The terms $(1+S_i)/2$ are projectors, since $S_i^2 = 1$ and therefore

$$\left(\frac{1+S_i}{2}\right)^2 = \frac{1+2S_i+S_i^2}{4} = \frac{1+S_i}{2}\,. \tag{3.29}$$

It follows that G_a and G_b are themselves projectors, since

$$G_{a/b}^2 = \left(\prod_{i\in a/b} \frac{1+S_i}{2}\right)^2 = \prod_{i\in a/b} \left(\frac{1+S_i}{2}\right)^2 = \prod_{i\in a/b} \frac{1+S_i}{2} = G_{a/b}\,. \tag{3.30}$$

Here we have used that the stabilisers S_i and consequently the terms $(1+S_i)/2$ are commuting operators [123]. Equation 3.28 can then be simplified to

$$\langle G_a G_b \rangle_\psi \leq \sqrt{\langle G_a \rangle_\psi \langle G_b \rangle_\psi}\,. \tag{3.31}$$

We then generalise to mixed states by first writing the density matrix ρ as a linear combination of pure states, i.e. $\rho = \sum_k p_k |\psi_k\rangle \langle\psi_k|$, and applying the above inequality to each term in the sum separately. We obtain

$$\langle G_a G_b \rangle = \sum_k p_k \langle\psi_k| G_a G_b |\psi_k\rangle \leq \sum_k p_k \sqrt{\langle\psi_k| G_a |\psi_k\rangle \langle\psi_k| G_b |\psi_k\rangle}\,. \tag{3.32}$$

We identify the right term as the scalar product of two vectors $\langle u|v\rangle = \sum_k u_k v_k$, where the coefficients u_k and v_k define the vectors with respect to some orthonormal basis. We can then write $u_k = \sqrt{p_k \langle\psi_k| G_a |\psi_k\rangle}$ and $v_k = \sqrt{p_k \langle\psi_k| G_b |\psi_k\rangle}$ and use the Cauchy-Schwarz inequality again to get

$$\sum_k \sqrt{p_k \langle\psi_k| G_a |\psi_k\rangle} \sqrt{p_k \langle\psi_k| G_b |\psi_k\rangle} \leq \sqrt{\left(\sum_k p_k \langle\psi_k| G_a |\psi_k\rangle\right)\left(\sum_{k'} p_{k'} \langle\psi_{k'}| G_b |\psi_{k'}\rangle\right)}\,, \tag{3.33}$$

which shows that

$$\mathcal{F} = \langle G_a G_b \rangle \leq \sqrt{\langle G_a \rangle \langle G_b \rangle} \equiv \mathcal{F}_+\,. \tag{3.34}$$

The term $\mathcal{F}_+$ thereby provides an upper bound of the fidelity.

4. Graph state generation with a single atom

The results of this chapter have been published in Ref. [124]: P. Thomas, L. Ruscio, O. Morin, G. Rempe, **Efficient generation of entangled multiphoton graph states from a single atom.** *Nature* **608**, 677-681 (2022).

As discussed in the previous chapter, photonic graph states are a versatile resource for quantum computation and communication. Numerous quantum information protocols have been implemented in small-scale proof-of-principle experiments using spontaneous parametric down-conversion (SPDC) [59–61, 63]. However, the probabilistic generation process of this technique represents a severe scalability limitation.

As an alternative approach, single quantum emitters have been considered as efficient sources for photonic graph states [65–67]. In this case, the emission process is, in principle, deterministic, in the sense that the efficiency is constrained solely by optical losses, rather than by any inherent limitations within the photon generation mechanism itself. It is important to note that any experiment involving optics is inevitably affected by optical losses and thus cannot be truly deterministic. Nevertheless, following the language convention used in the scientific literature, we will continue to refer to such schemes as deterministic.

The fundamental principle of this method is to combine the emission capability with an internal spin degree of freedom of the quantum emitter. The interplay between the two leads to entanglement between the spin state and the polarisation of the photon (similar to chapter 2.2.5). Repeating this process multiple times results in entanglement that extends over the entire chain of generated photons. This scheme was first successfully demonstrated in 2016 using a quantum dot [68]. Since then, various other experiments have explored similar strategies, based on quantum dots [125–127] or Rydberg ensembles [128]. However, none of these implementations were able to demonstrate a scaling advantage over the probabilistic SPDC technique [63], primarily due to a low generation and collection efficiency.

This chapter describes experiments in which we efficiently prepare photonic graph states using a single atom in a cavity. We demonstrate the generation of two types of graph states, namely GHZ states and linear cluster states. In both cases, the experimental protocol consists of a periodic sequence of photon emissions interleaved with single-qubit rotations on the atomic state. We successfully prepare and measure GHZ states containing up to 14 photons and linear cluster states with up to 12 photons, with a fidelity exceeding the classical threshold of 0.5. The experimental sequence incorporates a built-in dynamical decoupling mechanism that protects the atomic qubit and thus the generated multiphoton state from noise. The measured coincidence rate exceeds that of previous implementations by orders of magnitude, demonstrating a clear scaling advantage of the single-emitter strategy.

4.1. Experimental protocol

The experimental setup used for our experiments is shown schematically in Fig. 4.1. The complete apparatus is described in depth in chapter 2.1. A more detailed drawing can be

found in Fig. 2.1.

For the experiment, we trap a single ^{87}Rb atom at the centre of a high-finesse optical cavity. By repeatedly applying the vSTIRAP mechanism (see chapter 2.2.2) we generate a series of single photons. The photons are outcoupled from the cavity predominantly through one of the mirrors, which we call the outcoupling mirror. The photons are directed to the detection setup (chapter 2.1.6), which is used to analyse their polarisation state. The main components of the detection setup are a polarising beam splitter (PBS) and a pair of superconducting nanowire single-photon detectors (SNSPD). The detection setup features dynamic control of the measurement basis via an electro-optic modulator (EOM), which is tuned for switching between the Z and X bases. A motorised $\lambda/2$-waveplate allows to continuously scan the detection basis along the equator of the Bloch sphere.

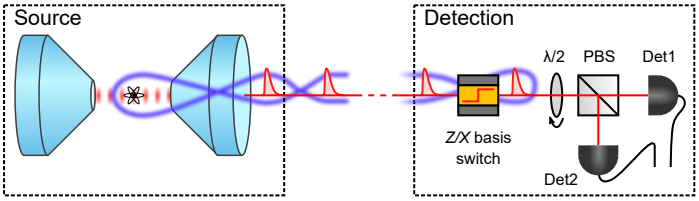

Figure 4.1.: Schematic sketch of the setup. The atom-cavity system acts as a source of single photons. These are analysed with a detection setup, consisting of a polarising beam splitter (PBS) and a pair of single-photon detectors (Det1 and Det2). A polarisation EOM and a motorised $\lambda/2$-waveplate allow control of the measurement basis.

The experimental sequence is shown in Fig. 4.2a, along with the corresponding processes in the atomic level diagram. First, the atom is prepared in the state $|2,0\rangle$ by optical pumping (see chapter 2.2.1). A control pulse is then applied to induce the vSTIRAP process, which produces the first photon (photon 1), which is entangled in polarisation with the atomic state. This process can be expressed as

$$|2,0\rangle \rightarrow \frac{1}{\sqrt{2}} \left(|1,+1\rangle |L\rangle - |1,-1\rangle |R\rangle \right) , \tag{4.1}$$

and constitutes the initialisation of the protocol. Here, $|R\rangle$ and $|L\rangle$ denote right and left circular polarisation and define the photonic qubit basis. This first step is exactly equivalent to the atom-photon entanglement mechanism described in chapter 2.2.5. The absence of a photon detection event signals the failure of the initialisation step. For this case, the sequence is programmed to go back to the initial state preparation, followed by another photon production attempt. If necessary, this procedure is repeated multiple times to increase the chances of detecting a photon. Since the optical pumping causes the atom to heat up, we find a compromise of a total of seven attempts for the initialisation step.

Next, we apply a single qubit rotation R_θ of angle θ to the atomic qubit using the 790 nm Raman laser (①). When producing GHZ states, the required angle is $\theta = 0$ and the Raman rotation can be skipped entirely. For 1D cluster states, we have to apply a rotation with $\theta = \pi/2$. Since in our geometrical configuration the atomic Clebsch-Gordan coefficients do not permit a direct Raman transfer between the states $|1,+1\rangle$ and $|1,-1\rangle$, we use a sequence of Raman transfers making use of the intermediate state $|2,0\rangle$, as explained in chapter 2.2.3. After the gate operation, we use the same Raman laser to transfer the qubit from $|1,\pm 1\rangle$ to $|2,\pm 2\rangle$ (②). By applying another vSTIRAP control pulse (③) we produce another photon (④), which also brings the atom back to $|1,\pm 1\rangle$. The steps ①-④ form

one iteration of the cycling stage as shown in Fig. 4.2a. One such iteration lasts 200 µs (50 µs) for the cluster (GHZ) state sequence. This cycle can be repeated for as many times as desired, each time adding another qubit to a growing chain of entangled photons. For a target state of size N, we run $N-2$ cycles to produce photons 2, 3,..., $N-1$. For the last photon (N) we perform the closing step, which realises an atom-to-photon state transfer. To do this, we use another Raman pair at 795 nm to transfer the qubit from $|1,\pm 1\rangle$ to $|2,\mp 1\rangle$, instead of $|2,\pm 2\rangle$ (see chapter 2.2.3). In the subsequent emission process, the atom undergoes a transition to the $|1,0\rangle$ state, fully transferring the qubit from the atom to the photon. This has the effect of disentangling the atomic qubit from the previously generated string of photons. In the cluster state protocol, it is alternatively possible to disentangle the emitter qubit by measuring the last photon in the Z basis [67]. A detailed illustration of the different steps of the protocol can be found in Appendix B.

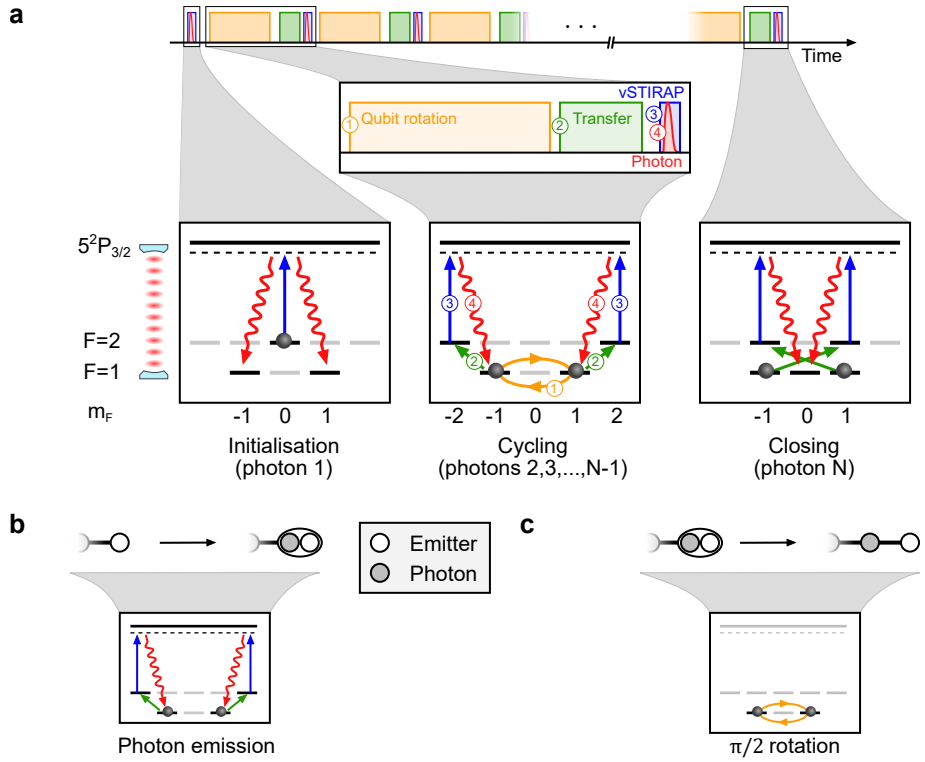

Figure 4.2.: Experimental protocol. (**a**) A first photon is generated from $|2,0\rangle$ (initialisation), followed by several iterations of the cycling step. Each iteration consists of a unitary single-qubit gate (1), a transfer of the qubit to $|2,\pm 2\rangle$ (2) and a vSTIRAP control pulse (3) which generates a photon (4). In the final step (closing) the qubit is transferred to $|2,\mp 1\rangle$. The subsequent photon emission disentangles the atomic degree of freedom from the photonic multi-qubit state. (**b**) In the graph state picture, the emission step corresponds to adding a photonic qubit to the emitter vertex, thus creating a redundantly encoded qubit. (**c**) A $\pi/2$ rotation on the atomic state pushes out the emitter qubit. This creates two separate vertices connected by an edge.

In chapter 3.2.2, we have already introduced the concept of redundantly encoded qubits. These are useful to understand the effect of the different steps in the protocol using the graph state notation. A photon emission consisting of a Raman transfer $|1,\pm 1\rangle \rightarrow |2,\pm 2\rangle$ combined with a vSTIRAP simply adds a photonic qubit to the emitter vertex (Fig. 4.2b). The photon and the emitter then form a redundantly encoded qubit consisting of two physical qubits. The GHZ state protocol simply repeats this step multiple times, so that the resulting multi-qubit state is a single redundantly encoded qubit consisting of N

physical qubits.

The effect of the Raman $\pi/2$ rotation is shown in Fig. 4.2c. The single-qubit gate performed on the atom pushes the emitter qubit out of the redundantly encoded vertex. The two qubits that previously shared a common vertex are now represented by two separate vertices connected by an edge. The cluster state protocol is a sequence of photon emissions interleaved with this 'push-out' operation. This creates a graph consisting of N vertices arranged in a line, i.e. a linear cluster state.

Fig. 4.3 shows a histogram of photon detection events as a function of time for fifteen consecutive photon generation attempts. Since we used the cluster state protocol for this measurement, the single-photon wave packets are equally spaced by 200 µs, which is the cycle duration of the sequence. The inset shows a zoom on one of the wave packets, which has a width of 300 ns (full width at half maximum). Due to spontaneous scattering processes, which mainly affect the tail of the photon (see chapter 4.4), we restrict the acceptance interval to 1 µs, as indicated by the dashed lines. This interval contains more than 98% of the single-photon wave packet.

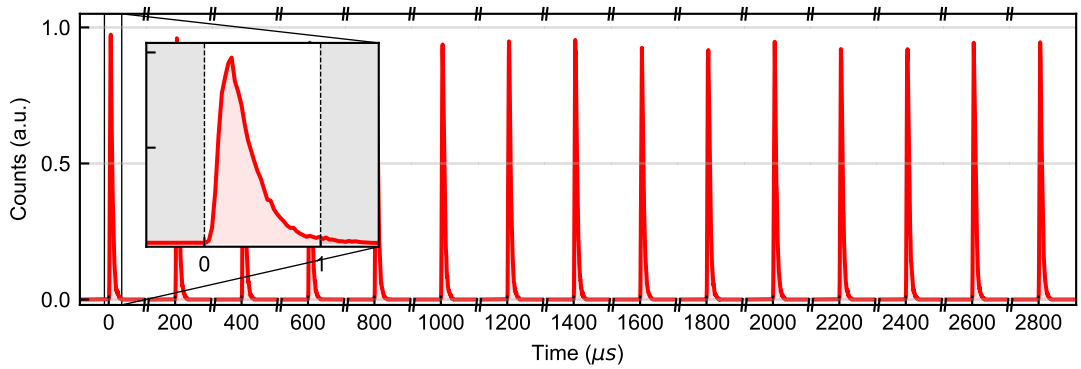

Figure 4.3.: Train of single photons. Histogram of photon detection events as a function of time for the cluster state protocol. Fifteen consecutive wave packets were recorded. The inset shows a zoom on one of the photons. The dashed lines mark the acceptance interval for postselection.

4.2. GHZ states

As a first example, we present the generation of GHZ states, which are an important example of multi-qubit entanglement. In its most common form, the explicit expression of an N-qubit GHZ state is

$$|\mathrm{GHZ}_N\rangle = \frac{1}{\sqrt{2}}\left(|0\rangle^{\otimes N} + |1\rangle^{\otimes N}\right). \tag{4.2}$$

Note that this differs from equation 3.19 up to local unitary rotations. Due to its simple structure, the GHZ state is relatively straightforward to characterise and the exact fidelity $\mathcal{F}_N^{(\mathrm{GHZ})}$ can be measured without performing full quantum state tomography [129]. At the same time, GHZ states are relatively susceptible to decoherence and are therefore often used for benchmarking and quantitative comparison between different platforms. While their fragile nature may be drawback in many scenarios, it can also be seen as a resource in the context of quantum metrology [130].

Fidelity estimation

For fidelity estimation, GHZ states are a special case among graph states. Their density matrix consists of only four non-zero elements, two on the diagonal and two on the off-diagonal, which greatly facilitates the measurement of the fidelity. Along the lines of what was described in chapter 3.4, a lower bound can be derived in terms of the stabilisers S_k, which for GHZ states gives

$$\mathcal{F}_N^{(\mathrm{GHZ})} \geq \left\langle \frac{1+S_1}{2} \right\rangle + \left\langle \prod_{k=2}^{N} \frac{1+S_k}{2} \right\rangle - 1\,. \tag{4.3}$$

Here, the stabilisers are defined as

$$S_1 = \prod_{i=1}^{N} X_i\,, \tag{4.4}$$

$$S_k = Z_{k-1}Z_k, \text{ for } k = 2,3,...,N\,. \tag{4.5}$$

Two local measurement settings are required to measure all stabilisers and thus the lower bound given in equation 4.3. In addition to this, it has been shown that the four elements of the density matrix can be measured to determine the exact fidelity using only $N+1$ local measurement settings [129]. Although this approach demands more effort than the two settings required for the lower bound, it is highly preferable to the exponential overhead that comes with the full reconstruction of the density matrix. This method, commonly known as *parity oscillations*, is briefly explained below.

Parity oscillations

To measure the populations $\mathcal{P}_N$ of the $|0\rangle^{\otimes N}$ and $|1\rangle^{\otimes N}$ components of the state, it suffices to measure all particles in the Z basis. We then obtain

$$\mathcal{P}_N = \left\langle (|0\rangle\langle 0|)^{\otimes N} + (|1\rangle\langle 1|)^{\otimes N} \right\rangle\,. \tag{4.6}$$

This is simply the number of events in which all qubits were measured in the same state divided by the total number of events, i.e. $\left(N_{|00...0\rangle} + N_{|11...1\rangle}\right)/N_{\mathrm{tot}}$.

For the coherence terms on the off-diagonal, we introduce the parity operator [63, 129]

$$\mathcal{M}_\phi = \begin{pmatrix} 0 & e^{-i\phi} \\ e^{i\phi} & 0 \end{pmatrix}^{\otimes N}\,. \tag{4.7}$$

The operator $\mathcal{M}_\phi$ is a tensor product of N identical matrices. These can be written as a sum of the X and Y Pauli matrices and correspond to a measurement in the basis $(|0\rangle \pm e^{i\phi}|1\rangle)/\sqrt{2}$. The measurement basis lies on the equator of the Bloch sphere, with the parameter ϕ determining the angle with respect to the X basis. For an ideal GHZ state, the expectation value of $\mathcal{M}_\phi$ exhibits a cosine-like behaviour, with the frequency of its oscillations being proportional to the qubit number N:

$$\langle \mathcal{M}_\phi \rangle = \cos(N\phi)\,. \tag{4.8}$$

The maxima and minima of this oscillation are found at angles of $\phi = k\pi/N$, where $k = 1, 2, ..., N$. For fidelity estimation, it is sufficient to measure the expectation value of $\mathcal{M}_\phi$ at these angles, i.e. N measurement settings with $\mathcal{M}_{k\pi/N}$. For example, measuring the

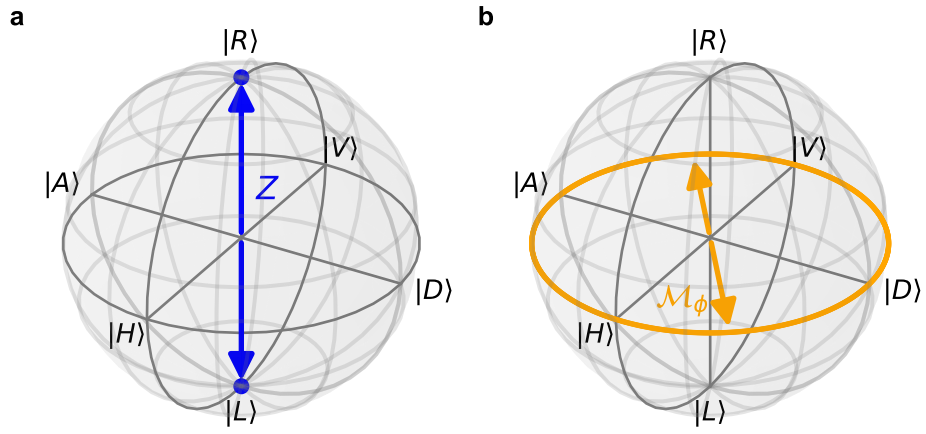

Figure 4.4.: Fidelity measurement for GHZ states. (**a**) The population term $\mathcal{P}_N$ is obtained from a measurement in the eigenbasis (Z basis). (**b**) The operator $\mathcal{M}_\phi$ corresponds to a measurement basis that lies on the equator of the Bloch sphere and allows to determine the coherences $\mathcal{C}_N$. For a given experimental run, all photons are measured in the same basis.

coherence terms $\mathcal{C}_3$ of the three-qubit GHZ state $|\mathrm{GHZ}_3\rangle = (|000\rangle + |111\rangle)/\sqrt{2}$ requires the terms $\mathcal{M}_{\pi/3}$, $\mathcal{M}_{2\pi/3}$ and $\mathcal{M}_\pi$. The term $\mathcal{C}_N$ is then computed using the formula

$$\mathcal{C}_N = \frac{1}{N}\sum_{k=1}^{N}(-1)^k \left\langle \mathcal{M}_{k\pi/N} \right\rangle . \tag{4.9}$$

Measuring the quantities $\mathcal{P}_N$ and $\mathcal{C}_N$ in this way requires a total of $N+1$ measurement settings. Alternatively, the coherence term $\mathcal{C}_N$ can be obtained by simply measuring the full oscillation pattern of equation 4.8 and extracting the visibility from a cosine fit. Combined with the population term $\mathcal{P}_N$, the fidelity is given by the formula

$$\mathcal{F}_N^{(\mathrm{GHZ})} = (\mathcal{P}_N + \mathcal{C}_N)/2 . \tag{4.10}$$

Results

We start by measuring the population terms $\mathcal{P}_N$ on the diagonal of the density matrix. These are obtained from a Z basis measurement of all qubits. The measurement probability of certain measurement patterns is plotted in Fig. 4.5a-h. A measurement pattern is simply given by the measurement results (R and L) of each qubit obtained in a given experimental run. These are grouped according to the number of R photons in the detected pattern. In this way, the $|RR...R\rangle$ and $|LL...L\rangle$ components become clearly visible as the two dominant contributions in each plot. The sum of both of these terms gives the populations $\mathcal{P}_N$.

The coherence terms $\mathcal{C}_N$ are obtained by scanning the measurement basis along the equator of the Bloch sphere, i.e. setting the basis to $(|R\rangle \pm e^{i\phi}|L\rangle)/\sqrt{2}$, where ϕ takes values between 0 and π. Fig. 4.5i-o shows the characteristic parity oscillations, scaling as $\propto \cos(N\phi)$. We measure the full oscillations for photon numbers N = 2,3,4,5,6,8,10. In each case we extract the visibility of the oscillation to determine the coherence terms in the density matrix. For photon number $N = 14$, we measure about one coincidence every three minutes. At this rate, measuring the full oscillation pattern would be an

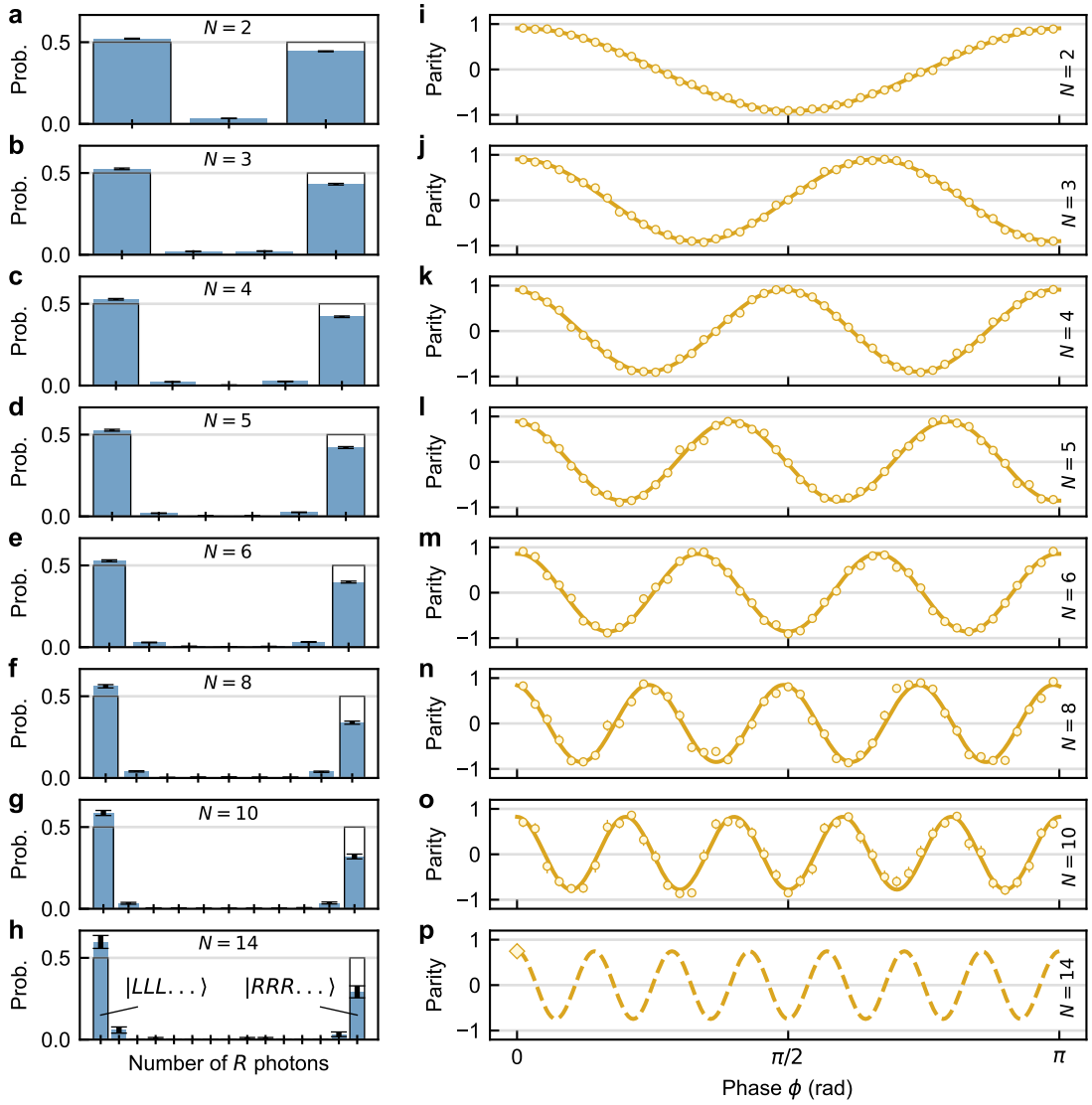

Figure 4.5.: Population ($\mathcal{P}_N$) and coherence ($\mathcal{C}_N$) terms of the generated GHZ states. (**a-h**) Measurement statistics of different computational basis patterns. The y-axis shows the measurement probability, the x-axis denotes the number of R photons the measurement pattern contains. Thus, the dominant contribution represented by the outermost bars correspond to the $|RRR...\rangle$ and $|LLL...\rangle$ components of the GHZ states. We observe an asymmetry between the two patterns as compared to the ideal statistics as indicated by black frames, most likely stemming from a small difference in optical detection efficiency of the R and L detection channels. (**i-p**) Parity oscillations for different GHZ state sizes. The oscillation frequency increases linearly with the qubit number N. The visibility of the oscillation corresponds to the coherence term $\mathcal{C}_N$. For $N = 14$ (**p**) only one setting of the phase parameter ϕ was measured (yellow diamond). The expected oscillation behaviour with an amplitude equal to the measured value at $\phi = 0$ is plotted as a dashed line.

unreasonably lengthy process. We therefore only measure the parity for $\phi = 0$, which is indicated by the yellow diamond in Fig. 4.5p.

The fidelity is then obtained from equation 4.10 and is shown in red in Fig. 4.6. Since we do not measure the full oscillation for $N = 14$, we provide a fidelity lower bound based on the stabiliser operators S_k. Note that in our choice of basis, the parity measurement at $\phi = 0$ corresponds to an X measurement, from which we obtain S_1. Measuring all

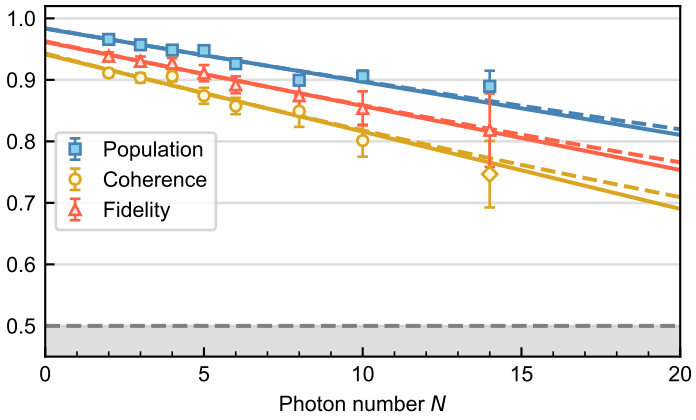

Figure 4.6.: GHZ state fidelity. Population $\mathcal{P}_N$ (blue) and coherence terms $\mathcal{C}_N$ (yellow) as obtained from the measurement in Fig. 4.5 for different N. The fidelity $\mathcal{F}_N$ (red) is derived from the formula $\mathcal{F}_N = (\mathcal{P}_N) + \mathcal{C}_N)/2$ and plotted in red. The data is fitted with a linear (solid) and an exponential (dashed) fit model.

the photons in the Z basis gives access to all other stabilisers $S_{k\geq 2}$. Thanks to equation 4.3, we can then prove genuine 14-photon entanglement with a fidelity $\mathcal{F}_{14}^{(\mathrm{GHZ})} \geq 76(6)\%$, exceeding the 50% threshold by more than 4 standard deviations. To date, this is the largest entangled state of optical photons observed experimentally.

Within the measured range, we observe a shallow decay of $\mathcal{P}_N$, $\mathcal{C}_N$ and $\mathcal{F}_N$ as a function of photon number. The overall trend is well described by a linear model (solid lines) with a slope of 0.86(9)%, 1.3(2)% and 1.04(9)% per photon, respectively. If one were to include even higher N, an exponential model (dashed lines) would be more appropriate. By extrapolation, we can then predict at which photon number N the fidelity would cross the 50% threshold. For the exponential model, this would occur at around 55 photons. In contrast, the linear fit crosses the 50% threshold slightly earlier, at approximately 44 qubits.

Built-in dynamical decoupling

The high fidelity observed even in larger states is, to some extent, attributable to a dynamical decoupling mechanism intrinsic to the protocol. It manifests itself in the fact that the fidelity remains high, even if the duration of the protocol is deliberately extended beyond the intrinsic coherence time of the emitter, which is approximately 1 ms (see also Fig. 2.19). In essence, this mechanism arises from the opposite signs of the Zeeman splitting within the $F = 1$ and $F = 2$ hyperfine manifolds, and is closely related to standard spin echo or dynamical decoupling techniques. During the experimental sequence, the atomic state carrying the qubit periodically alternates between the $|1, \pm 1\rangle$ and $|2, \pm 2\rangle$ states. When the qubit is in the $F = 1$ ($F = 2$) manifold and picks up a random phase due to magnetic field noise, a transfer to $F = 2$ ($F = 1$) followed by an appropriate waiting time will reverse this phase. This is because the energy shift on the qubit states now acts in the opposite direction. This is true as long as the noise occurs on a timescale much longer than one cycle of the protocol, as is the case for spin echo or dynamical decoupling schemes.

To demonstrate the existence of this mechanism, we extend the duration of the protocol, which is expected to exacerbate the effect of decoherence. In particular, we run the protocol for a six-photon GHZ state, with the duration of one photon generation cycle increased

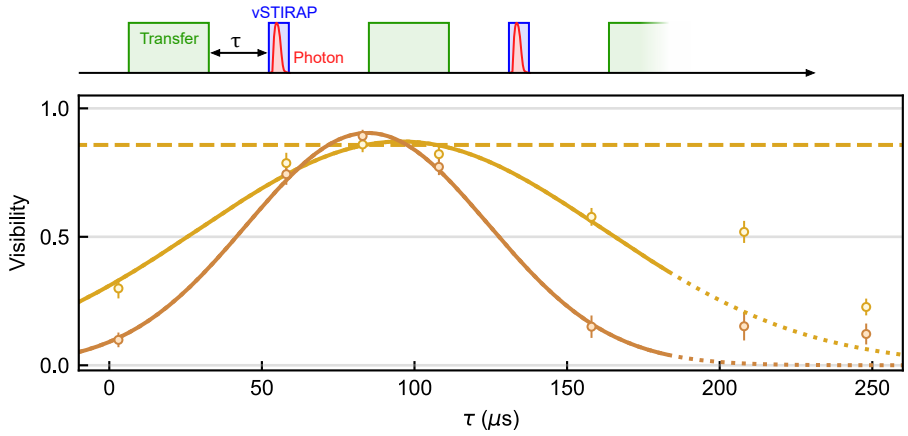

Figure 4.7.: Built-in dynamical decoupling mechanism. To demonstrate that the magnetic field noise is indeed reduced, we run the protocol for a six-photon GHZ state and extend the duration of the protocol to 1.25 ms. The visibility of the parity oscillations is plotted in yellow on the y-axis. To further highlight the effect, we deactivate the magnetic-field feedforward and repeat the measurement (brown). The data are fitted to a Gaussian function, only including data points where the fit is plotted as a solid line. The dashed horizontal line marks the visibility of the fringes seen in Fig. 4.5m.

from 50 μs to 300 μs. The full protocol then takes 1.25 ms, which is roughly equal to the coherence time of the atom. We vary the time τ between the Raman transfer and the photon production pulse, effectively scanning the time the atomic qubit spends in $|F = 2\rangle$ relative to the time it spends in $|F = 1\rangle$. The visibility of parity oscillations is plotted as a function of τ (Fig. 4.7, yellow markers), thereby making the dynamical decoupling effect visible. The central observation is the maximum of the fringe contrast around 90 µs, which is where the phases acquired in $|F = 1\rangle$ and $|F = 2\rangle$ cancel out. Note that for a perfect phase cancellation, the qubit has to spend twice as much time in $|F = 1\rangle$ than in $|F = 2\rangle$, due to the different m_F quantum numbers. The observed maximum in Fig. 4.7 is therefore in the expected position. The data are fitted to a Gaussian function to emphasise the overall trend. In terms of the maximum fringe visibility, we observe no difference from the data obtained using the standard protocol with 50 µs per cycle (yellow dashed line). Note that an accurate theoretical model requires a better knowledge of the noise spectrum present in the experiment. The choice of a Gaussian fit function therefore serves only as a guide to the eye, offering no insight into the underlying dynamics.

To provide further evidence, we repeat the experiment while deliberately increasing the magnetic field noise. This is achieved by deactivating the magnetic-field feedforward (see chapter 2.2.6). We observe a similar behaviour, with no notable difference in the maximum oscillation amplitude at the rephasing point. However, we do see that the measured curve is narrower than in the previous case, as expected.

In conclusion, the data provide clear evidence for the existence of a mechanism that greatly reduces the influence of magnetic field noise on the fidelity of the generated GHZ states. The advantage is that this effect can be exploited by simply manipulating the timing parameters, without the need for any additional steps in the protocol.

Supersensitive phase measurements

Beyond the applications in the realm of quantum information processing, quantum effects play a pivotal role in quantum metrology. This field of research aims to enhance the

precision of measurements by harnessing quantum phenomena, in particular entanglement and squeezing. Squeezing, for example, has become an established tool to increase the sensitivity of modern gravitational wave detectors [131].

Entangled states of photons have been proposed as a means of increasing the sensitivity of interferometric measurements [130]. A classic example showcasing the enhancement of phase sensitivity through entanglement is a Mach-Zehnder interferometer that is probed with a state known as N00N state [132, 133]. The term 'N00N state' originates from its mathematical expression $(|N,0\rangle_{a,b} + |0,N\rangle_{a,b})/\sqrt{2}$, where a and b denote the arms of the interferometer. A state of this form bears a strong resemblance to an N-photon GHZ state. Indeed, both types of states can be used to detect small changes in a certain parameter, such as the optical phase [134]. The concept of entanglement-enhanced interferometry has been explored in various experiments using nonlinear optics sources [135–138] and more recently quantum dots [139].

In the following, we consider a GHZ state consisting of N photons. The N-fold increase in the oscillation frequency (see Fig. 4.5) is the characteristic signature of an enhanced susceptibility to the optical phase. This behaviour, also observed in N00N states, is termed superresolution. However, it is important to note that superresolution is distinct from the concept of supersensitivity, which refers to a superior phase sensitivity compared to classical light. For this to be the case, certain conditions must be met in regard to oscillation visibility and efficiency.

To illustrate this, consider a birefringent medium that induces a phase shift ϕ between the right and left circular polarisation states. The transformation would be expressed as

$$T_\phi = |R\rangle\langle R| + e^{i\phi}|L\rangle\langle L| \,. \tag{4.11}$$

A single photon in the horizontally polarised state $|H\rangle = (|R\rangle + |L\rangle)\sqrt{2}$ evolves to

$$T_\phi |H\rangle = \big(|R\rangle + e^{i\phi}|L\rangle\big)/\sqrt{2}\,, \tag{4.12}$$

when passing through the medium. Afterwards, the probability of measuring the photon in the $|H\rangle$ state is

$$P_{|H\rangle} = \big(1+\cos(\phi)\big)/2\,. \tag{4.13}$$

Repeating the experiment N times can be used to estimate ϕ. The uncertainty of the measurement is $\Delta\phi_{\text{class}} = 1/\sqrt{N}$, which is known as the standard quantum limit (SQL). If instead we prepare an N-photon GHZ state, it would transform as

$$T_\phi |\text{GHZ}_N\rangle = \frac{1}{\sqrt{2}}\big(|R\rangle^{\otimes N} + e^{iN\phi}|L\rangle^{\otimes N}\big)\,. \tag{4.14}$$

Due to the factor of N in the phase factor, the uncertainty is now $\Delta\phi_{\text{ent}} = 1/N$. This is referred to as the Heisenberg limit and constitutes an improvement of $1/\sqrt{N}$ over the SQL. If the oscillations have a visibility V smaller than one, then $\Delta\phi_{\text{ent}}$ becomes $1/NV$ [136]. The enhancement in phase sensitivity can then be expressed as the ratio

$$\frac{\Delta\phi_{\text{class}}}{\Delta\phi_{\text{ent}}} = V\sqrt{N}\,, \tag{4.15}$$

where supersensitivity is achieved, if this ratio lies above one.

Fig. 4.8 displays $\Delta\phi_{\text{class}}/\Delta\phi_{\text{ent}}$ as a function of photon number N. Here, the visibility V corresponds to the amplitude of the parity oscillations shown in Fig. 4.5. We observe supersensitivity, i.e. $\Delta\phi_{\text{class}}/\Delta\phi_{\text{ent}} > 1$, up to a photon number of $N = 178$, with a maximum at $N = 35$.

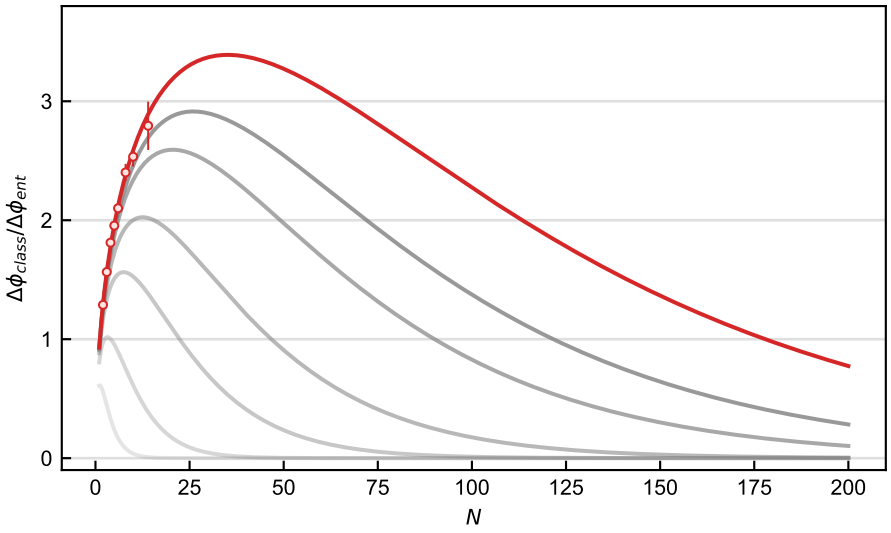

Figure 4.8.: Supersensitive phase estimation. The enhancement in sensitivity is given by the ratio $\Delta\phi_{\text{class}}/\Delta\phi_{\text{ent}}$. The data points correspond to the intrinsic efficiency of $\eta = 1$, which does not consider optical losses. The red line is a fit to equation 4.15. The sensitivity drops if the efficiency is below one. This is shown by the grey lines, for which η takes the values 0.99, 0.98, 0.95, 0.9, 0.75, 0.43.

It is important to note that the achieved supersensitivity is conditioned on the detection of all N photons. In the presence of optical losses, an average number of $1/\eta^N$ trials is required to obtain an N-photon coincidence. Here, η is the probability to generate and detect a single photon. In this case, the sample is on average exposed to N/η^N photons per successful measurement. To beat the SQL, we therefore require a precision of $\sqrt{\eta^N/N}$ or better. The condition for supersensitivity is then modified to

$$\Delta\phi_{\text{class}}/\Delta\phi_{\text{ent}} = \sqrt{\eta^N} V \sqrt{N} > 1\,, \tag{4.16}$$

which is equivalent to the condition[1] $\eta^N V^2 N > 1$ [135]. The grey lines in Fig. 4.8 represent $\Delta\phi_{\text{class}}/\Delta\phi_{\text{ent}}$ for finite efficiencies $\eta < 1$. With the visibility achieved in our experiment, genuine supersensitivity would be reached for $\eta = 0.75$ and $N = 3$. Chapter 4.5 discusses ways to optimise the efficiency in our setup.

4.3. Linear cluster states

As a second example, we proceed with the generation of linear cluster states. Their explicit expression is more complicated than that of GHZ states. This is linked to the fact that their density matrix contains more non-zero elements, which makes the fidelity estimation more demanding. However, we take advantage of the fact that cluster states obey the set of stabiliser eigenvalue equations defined by their corresponding graphs (equation 3.11). For a linear cluster state of N qubits, the stabilisers are

$$S_k = Z_{k-1} X_k Z_{k+1}\,, \tag{4.17}$$

[1] There appears to be no clear consensus on how to incorporate the efficiency into this condition. It is sometimes stated as $\eta V^2 N > 1$, where η denotes the intrinsic preparation efficiency of the state, without accounting for optical losses [135, 136]. This formulation specifically addresses limitations that are inherent to probabilistic generation schemes like SPDC. In other literature sources (e.g. Ref. [138]), η does include transmission and detection efficiencies.

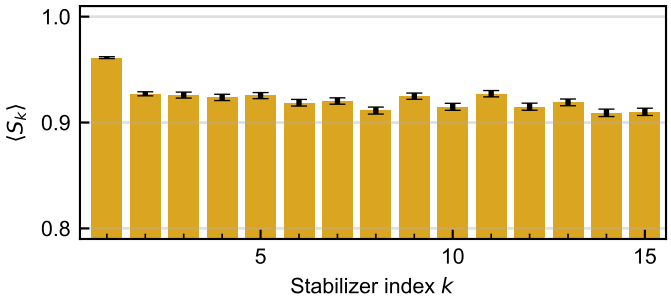

Figure 4.9.: Linear cluster state stabilisers. Measured expectation values of the stabiliser operators as a function of the stabiliser index.

where $k = 1, 2, ..., N$ and $Z_0 = Z_{N+1} = \mathbb{1}$.

The experimentally measured stabilisers are plotted in Fig. 4.9. We run several cycles of the protocol, as shown in Fig. 4.2, and collect coincidences of three consecutive photons ($k-1$, k, and $k+1$). If detected in the appropriate basis combination, these contribute to the stabiliser $S_k = Z_{k-1}X_kZ_{k+1}$. While in principle the protocol could be repeated for any number of cycles, we choose to terminate the sequence at $k = 15$ to measure the first 15 stabilisers. We find an average of $\langle S_1 \rangle = 96.13(9)\%$ and $\langle S_k \rangle = 92(1)\%$ for $k \geq 2$. These results suggest a large overlap between the generated state and the target linear cluster state.

In addition, a lower and an upper bound for the entanglement fidelity can be obtained from the stabilisers as discussed in chapter 3.4. For linear cluster states, the lower bound reads

$$\mathcal{F}_N^{(\mathrm{C})} \geq \langle G_a \rangle + \langle G_b \rangle - 1\,. \tag{4.18}$$

with

$$G_a = \prod_{k \text{ even}} \frac{1+S_k}{2}\,, \tag{4.19}$$

$$G_b = \prod_{k \text{ odd}} \frac{1+S_k}{2}\,. \tag{4.20}$$

The two product terms G_a and G_b correspond to the local measurement settings $M_a = Z_1X_2Z_3X_4...$ and $M_b = X_1Z_2X_3Z_4...$, respectively. As an illustrative example, we apply equation 4.18 to the specific case of a four-qubit linear cluster state and obtain

$$\mathcal{F}_4^{(\mathrm{C})} \geq \left\langle \frac{1}{4}\big(1+Z_1X_2Z_3\big)\big(1+Z_3X_4\big) \right\rangle + \left\langle \frac{1}{4}\big(1+X_1Z_2\big)\big(1+Z_2X_3Z_4\big) \right\rangle - 1\,. \tag{4.21}$$

As derived in chapter 3.4, an upper bound to the fidelity is given by the inequality

$$\mathcal{F}_N^{(\mathrm{C})} \leq \sqrt{\langle G_a \rangle \langle G_b \rangle}\,. \tag{4.22}$$

The witness-based fidelity estimation offers the advantage of an enormous reduction in measurement time as compared to quantum state tomography. However, this comes at the cost of a potentially large uncertainty, given by the width of the fidelity interval defined by the lower and upper bounds. The lower end of this interval must be above the 50% threshold in order to prove genuine multipartite entanglement. We find this to be the case for linear cluster states of up to 12 photons (Fig. 4.10). For the largest state of 12

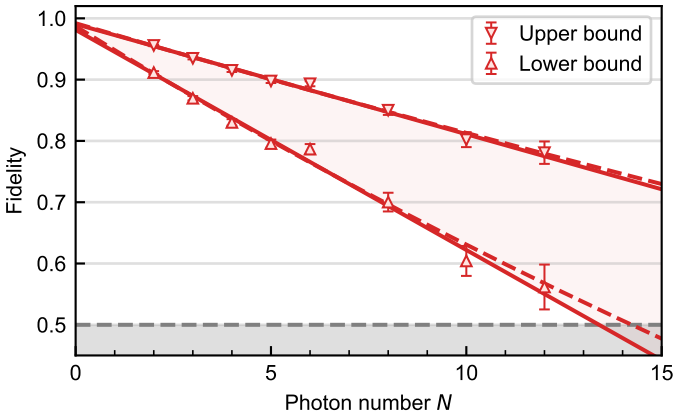

Figure 4.10.: Fidelity of linear cluster states. Measured data for the lower bound (triangles pointing upwards) and upper bound (triangles pointing downwards) as defined in equation 4.18 and 4.22. The solid (dashed) lines are linear (exponential) fits to the data. The grey dashed line marks the classical threshold of 50%. The true state fidelity lies between the two bounds in the red shaded area.

qubits, we measure the fidelity to be bounded by $0.56(4) \leq \mathcal{F}_{12}^{(C)} \leq 0.78(2)$. As for GHZ states, the cluster state data also follow an approximately linear trend, but decay faster with a slope of 3.6% and 1.8% per qubit for the lower and upper bound, respectively. We attribute this mainly to the $\pi/2$ rotation in between photon emissions, as this is the only additional step in the cluster state protocol.

Due to our method of fidelity estimation, the error per qubit is subject to a large uncertainty. This poses great difficulties in quantitatively estimating the contribution of a particular mechanism to the overall error. Other methods could greatly reduce this uncertainty [140, 141], but require the ability to measure qubits in the Y basis. Our current detection setup (Fig. 2.5) only allows measurements in the X or Z basis. However, an additional basis switch EOM would give access to the third basis setting, as well.

4.4. Sources of error

While the infidelity per photon of about 1% and 3.6% for GHZ and linear cluster states already represents a state-of-the-art result, we are interested in identifying as many sources of error as possible in order to improve the system for potential future experiments. With errors at the percent level, it becomes increasingly difficult to quantitatively identify the different sources of infidelity. Nevertheless, we have attempted to estimate the main contributors based on our experimental data.

Photon emission error

Imperfections in the photon emission process are likely to be a major contributor to the overall error. The following section discusses three different error processes related to the vSTIRAP mechanism. These are sketched in Fig. 4.11a-c.

The first is the result of an imperfect polarisation setting of the vSTIRAP control laser. Consider an atom in the state $|F = 2, m_F = 2\rangle$ prior to the photon emission step (Fig. 4.11a). Ideally, the control laser is purely π-polarised and couples to the excited state $|F' = 2, m'_F = 2\rangle$. In practice, however, it is difficult to perfectly align the polarisation

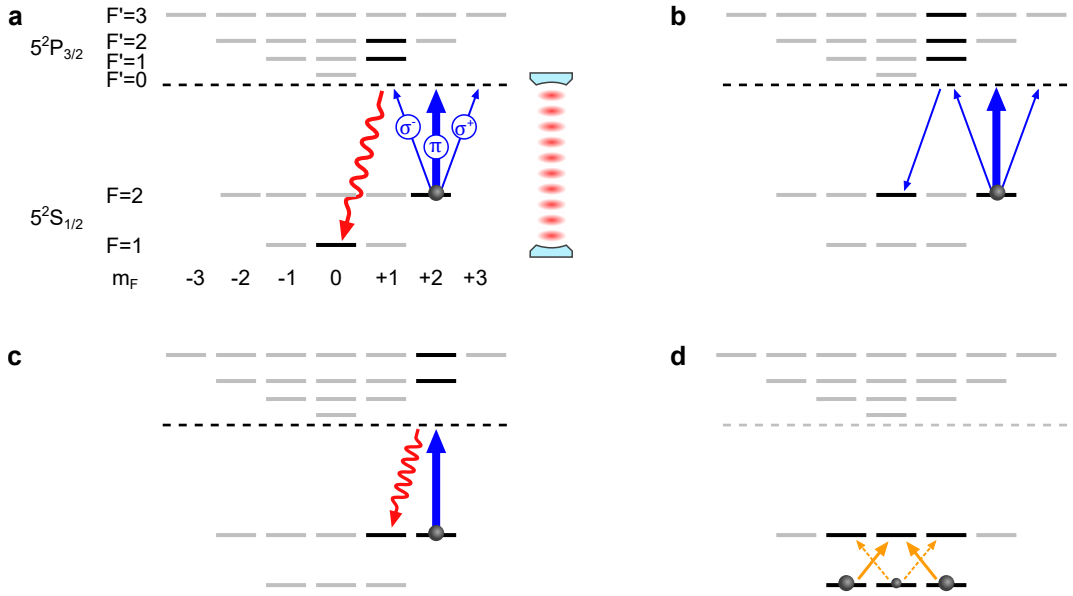

Figure 4.11.: Error mechanisms. (**a**) The ideally π polarised control laser is expected to have a small contamination of σ^+/σ^- components. These couple to the $|F'=1,m'_F=1\rangle$ and $|F'=2,m'_F=1\rangle$ levels of the excited state and induce a vSTIRAP process in which the atom ends up in $|F=1,m_F=0\rangle$. (**b**) The σ^+/σ^- components can also drive Raman transitions within the $F=2$ manifold, transferring the atom to $|F=2,m_F=0\rangle$. (**c**) Due to the finite cooperativity, the control laser can couple incoherently to the $|F'=2,m'_F=2\rangle$ or $|F'=3,m'_F=2\rangle$ state. From there the atom decays spontaneously, e.g. to $|F=2,m_F=1\rangle$. (**d**) The mechanisms shown in (**a-c**) lead to a small population in $|F=1,m_F=0\rangle$. A subsequent Raman $\pi/2$ pulse not only addresses the qubit populations (solid arrows), but also transfers the unwanted $m_F=0$ population to the $F=2$ manifold (dashed arrows).

vector with the quantisation axis, since neither the magnetic field, defining the quantisation axis, nor the polarisation can be precisely measured at the atomic position. This results in a small contamination of the control field by σ^+/σ^- polarisation components. The σ^- component can then couple to the states $|F'=1,m'_F=1\rangle$ and $|F'=2,m'_F=1\rangle$, leading to a $\Delta m_F=-2$ vSTIRAP process to the state $|F=1,m_F=0\rangle$.

A second process resulting from the imperfect polarisation of the control laser is shown in Fig. 4.11b. The σ^+/σ^- components can drive Raman transitions from the initial state $|F=2,m_F=2\rangle$ to $|F=2,m_F=0\rangle$, from which the atom can still emit a photon into the cavity, as it couples to the control laser.

The third process is linked to the finite cooperativity of the atom-cavity system (Fig. 4.11c), which allows the control laser to couple incoherently to the excited states, followed by a spontaneous decay. In this process, the $F'=3$ manifold is particularly detrimental. While $|F'=2\rangle$ contributes to the coherent photon emission to $|F=1,m_F=1\rangle$, the $|F'=3\rangle$ state can only decay back to $|F=2\rangle$, which is still addressed by the control laser. In Fig. 4.11c, this process is shown for the case where the atom ends up in the state $|F=2,m_F=1\rangle$, but it could also decay incoherently to $|F=2,m_F=2\rangle$ or $|F=1,m_F=1\rangle$.

Among the scenarios described above, events which result in the atom remaining in the $F=2$ manifold are of particular importance, i.e. Fig. 4.11b and c. In these cases, the atom can couple to the control laser a second time and emit a 'wrong' photon. Due to the atomic lifetime, these error mechanisms are expected to lead to a delayed photon emission. This is in agreement with the experimental data shown in Fig. 4.12. Here we run

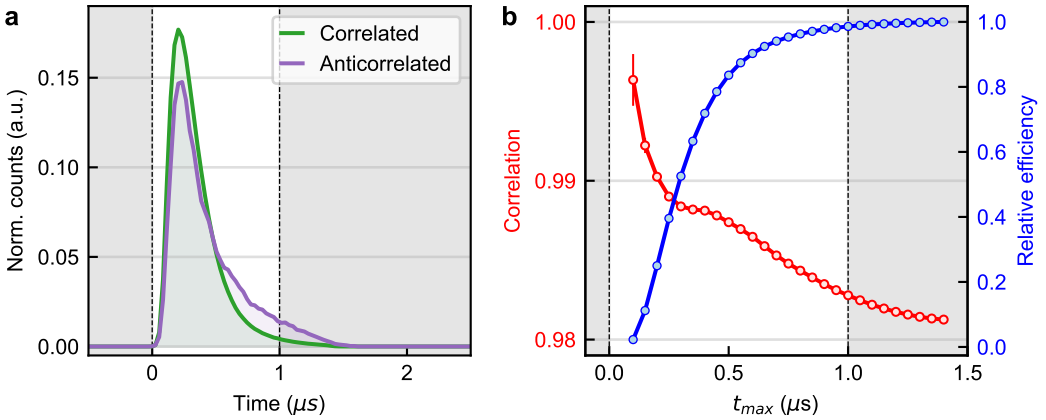

Figure 4.12.: Photon emission error. Correlation analysis in the Z basis of two consecutive photons in the GHZ protocol. (**a**) Histogram of the single-photon counts for the correlated and anticorrelated events. Since in most cases the photons are correlated, we normalise both wave packets to have the same area under the curve. The dashed lines mark the standard acceptance interval of 1 µs. (**b**) The data in red show the correlation for a variable acceptance interval $[0, t_{\max}]$. The relative efficiency (blue) is the relative portion of events that fall within this interval.

the GHZ protocol and analyse the correlations between two successive photons detected in the R/L basis. Fig. 4.12a displays the photon wave packet for events where the two photons are either correlated or anticorrelated. Since the correlated events are about 50 times more frequent, the wave packets are renormalised for clarity. In the anticorrelated case, we clearly observe that the centre of mass is shifted to the right, as more photons are detected towards the tail of the wave packet. This is confirmed in Fig. 4.12b. The y-axis shows the measured correlation between the two photons as a function of the width of the time interval in which the photon is detected. A clear drop in correlation is observed for longer detection intervals, meaning that the later the photons are detected, the lower their correlation. These observations are consistent with the photon emission error processes outlined in Fig. 4.11a-c. Mainly due to the mechanisms shown in Fig. 4.11a and c, there is a small probability that the atom will end up in $|F = 1, m_F = 0\rangle$ after photon emission. They are unlikely to affect the fidelity of GHZ states since in this case the atom does not produce a photon in the subsequent cycle. However, as will be explained later on, such events cause infidelity in the cluster state protocol.

Raman rotations

Another potential source of infidelity is given by the Raman rotations that implement single-qubit gates. Depending on the Raman driving strength, there is a certain probability of crosstalk between different transitions (see Fig. 2.11a), as they start to overlap in frequency for large Rabi frequencies. This probability depends on the ratio between the Rabi frequency Ω_0 and the Larmor frequency ω_L. Therefore, we choose a relatively small Rabi frequency on the order of $2\pi \cdot 10\,\mathrm{kHz}$ to minimise this effect. A simple estimate for the crosstalk is given by the factor $\Omega_0^2/(\Omega_0^2 + \delta'^2)$ in equation 2.6. Using $\delta' = 2\omega_L = 2\pi \cdot 200\,\mathrm{kHz}$, we find that the amount of crosstalk is less than 1%.

An experimental measure of the Raman infidelity is given by the oscillation visibility seen in Fig. 2.12. Taking into account photon emission errors of 1%, we find that the additional error introduced by the Raman rotation is about 1.5%, which is slightly more than is expected from Raman crosstalk alone. This discrepancy could be explained by

fluctuations in laser intensity. Moreover, it is worth noting that the observed infidelity could be caused, at least to some extent, by unwanted populations in other m_F states. This mechanism, which we refer to as 'qubit leakage', is explained in more detail below. However, the Raman errors and qubit leakage are difficult to discriminate experimentally. We estimate that the infidelity introduced by the Raman process alone is on the order of 1% or less.

Qubit leakage

During the cluster state protocol, the atomic qubit explores a subspace of the Hilbert space spanned by the two hyperfine ground state manifolds and their Zeeman sublevels. First, we have the qubit subspace composed of the states $|1,\pm 1\rangle$, which we call $\mathcal{H}_Q$. For photon emission and single-qubit rotations, the atomic population explores the intermediate states $|2,\pm 2\rangle$ and $|2,0\rangle$. We refer to these three states as $\mathcal{H}_{Q'}$. The three remaining states $|1,0\rangle$ and $|2,\pm 1\rangle$, which we define as the subspace $\mathcal{H}_\perp$, are ideally never populated. Nevertheless, we observe a small probability that the qubit leaks into this subspace or into an unwanted state within $\mathcal{H}_Q \otimes \mathcal{H}_{Q'}$.

The mechanisms responsible for this have been discussed previously (see Fig. 4.11a-c). For the cluster state protocol, events in which the atom undergoes a transition to $|1,0\rangle$ are particularly detrimental. The Raman $\pi/2$ rotation that follows photon emission addresses not only the transitions $|1,\pm 1\rangle \leftrightarrow |2,0\rangle$, but also the unwanted transitions $|1,0\rangle \leftrightarrow |2,\pm 1\rangle$, thus driving the parasitic population in $|1,0\rangle$ to the $F=2$ manifold (Fig. 4.11d). From there, the vSTIRAP pulse brings it back to $|1,0\rangle$. As a consequence, this population remains trapped in the unwanted subspace $\mathcal{H}_\perp$, but still produces photonic qubits throughout the rest of the protocol. The error thus propagates through the entire portion of the graph generated from that point on.

In order to confirm that this leakage to $|F=1,m_F=0\rangle$ actually occurs, we perform the following experiment, as sketched in Fig. 4.13a. We generate a photon from $|2,0\rangle$, identical to the atom-photon entanglement protocol (chapter 2.2.5), and postselect on detecting an L-polarised photon (step ①). We then drive the transition $|1,-1\rangle \leftrightarrow |2,0\rangle$, which is also in resonance with $|1,0\rangle \leftrightarrow |1,-1\rangle$ (step ②). Ideally, this does not affect the population in $|1,+1\rangle$, but could drive the parasitic population in $|1,0\rangle$. Finally, we transfer the $|1,+1\rangle$ population to $|2,+2\rangle$ and generate a photon (step ③). The probability of measuring this photon in the $|R\rangle$ state is plotted in Fig. 4.13b. While we expect this probability to be close to 1, we observe a sinusoidal deviation from this case. These oscillations are evidence for a small population in $|1,0\rangle$ after the initial photon emission. Indeed, the oscillation frequency is consistent with the relative strength of the transition, as determined by the corresponding Clebsch-Gordan coefficients. For a given optical power, we here expect a relative factor of $3/\sqrt{3}$ compared to the $|1,-1\rangle \leftrightarrow |2,0\rangle$ transition (see Fig. 2.11c).

We partially compensate for this effect in our measurements by applying a photon generation pulse after the Raman single-qubit rotation. This empties the $F=2$ manifold and in some of the cases produces a photon indicating the failure of the gate operation. However, the probability of detecting the error in this way is limited by the finite photon collection efficiency.

Detection errors

A minor source of error is given by imperfections in the detection setup. Since we measure photonic qubits, these errors stem from imperfect optical components and polarisation misalignment. The detection basis is set by passing light through a reference polariser,

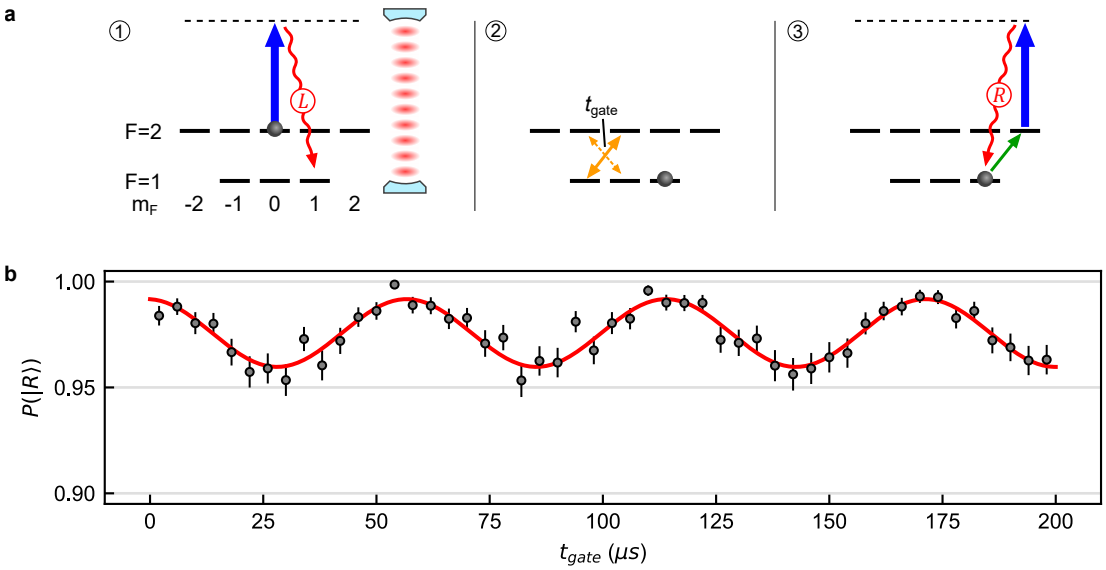

Figure 4.13.: Qubit leakage. (**a**) Protocol for probing the parasitic population in $|1,0\rangle$. First, the atom is projected into the state $|1,1\rangle$ by measuring an L-polarised photon. Subsequently, a Raman pulse of length t_{gate} is applied to the transitions $|1,-1\rangle \leftrightarrow |2,0\rangle$ and $|1,0\rangle \leftrightarrow |2,-1\rangle$. Finally, the population in $|1,1\rangle$ is read out. (**b**) Probability of measuring the second photon in the $|R\rangle$ state. The oscillations are evidence that after the initial step a small population resides in the state $|1,0\rangle$.

which is located directly behind the cavity, and maximising the extinction ratio between the two detectors. We reach an extinction ratio of about 1:10,000. When switching between the Z and the X bases, we apply a voltage to the EOM to rotate the polarisation. The extinction ratio of the EOM is specified as $> 1:1{,}000$, but we have measured values between $1:2{,}000$ and $1:5{,}000$.

4.5. Coincidence rate

In preceding sections of this chapter, we have demonstrated genuine multipartite entanglement in photonic graph states. Our approach relies on photon emission from a single atom in a cavity, using the vSTIRAP mechanism. Unlike the SPDC process, this mechanism does not encounter a fundamental limitation of the efficiency. Nevertheless, the previous record for the largest state of entangled photons was set using SPDC [63]. Several implementations of deterministic schemes [68, 125–128] have fallen short of this record, primarily due to a low photon collection efficiency. Therefore, a critical step toward demonstrating a genuine advantage over the probabilistic SPDC process involves improving the collection efficiency. The remainder of this chapter discusses the efficiency of our system and how it affects the rate at which an N-photon entangled state can be prepared and measured.

The success probability p_N of detecting a coincidence of N consecutive photons scales exponentially with the photon number, i.e. $p_N = \eta^N$. Here η denotes the probability of generating and detecting a single photon for a given attempt and can be expressed as the product of the source efficiency η_s and the detection efficiency η_d. The intrinsic source efficiency η_s, that is the probability of obtaining a photon at the output of the cavity, is given by

$$\eta_s = \frac{2C}{2C+1}\eta_{\mathrm{esc}}\,. \tag{4.23}$$

This expression is similar to equation 2.4, up to the escape efficiency $\eta_{\mathrm{esc}} = 0.89$, which

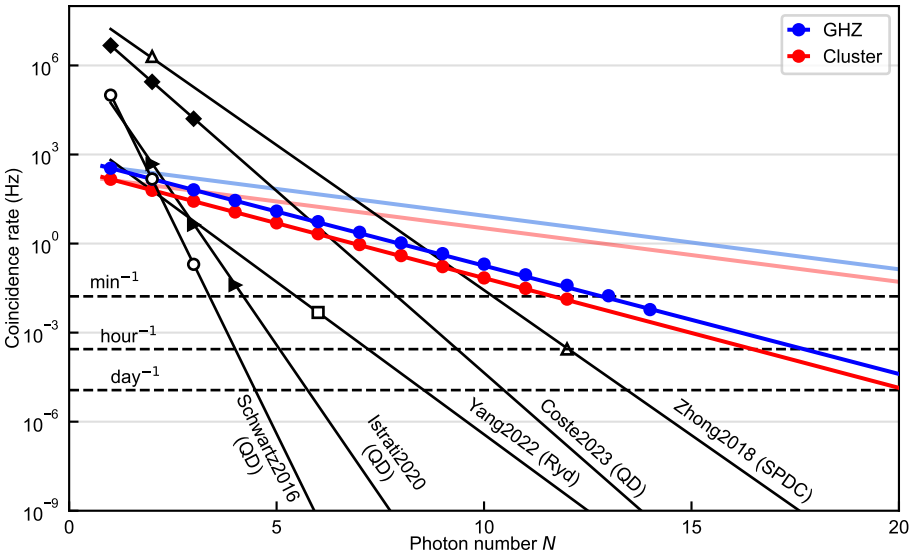

Figure 4.14.: Measured coincidence rate as a function of photon number. The data (blue for GHZ and red for cluster states) represent the real time coincidence rate of N photon events. The solid lines are exponential fits, from which we extract a single-photon generation and detection probability of $\eta = 43.18(7)\%$. The light coloured lines represent the estimated coincidence rates at the cavity output. Here we assume a loss-corrected efficiency of $\eta = 0.66$ (see also Ref. [70]). For comparison with our experiment, we plot the coincidence rates of other photon sources, such as quantum dots (QD), Rydberg ensembles (Ryd) and spontaneous parametric down-conversion (SPDC): Schwartz2016 [68], Istrati2020 [125], Yang2022 [128], Coste2023 [127], Zhong2018 [63].

takes into account the finite outcoupling probability from the cavity. Note that the above formula is only valid in the case of a single excited state, as the efficiency becomes a function of the atom-cavity detuning, i.e. $\eta_s(\Delta_{\mathrm{ac}})$, when multiple excited states are present.

The detection efficiency η_d is the probability of obtaining a detection event, given the presence of a photon at the output of the cavity. In our setup, it amounts to approximately $\eta_d \approx 0.7$, with the various loss contributions being free-space-to-fibre couplings (94% twice), propagation through optical fibre (97%), free-space optics (90%) and detector efficiency (90%).

The overall coincidence rate as a function of photon number N is shown in Fig. 4.14 including post-selection and experimental duty cycle. The experimental data for our cavity QED system are shown in blue for GHZ states and in red for cluster states. In both cases the data is extracted from the largest state that we measured (14 photons for GHZ and 12 photons for cluster states). Each point on the plot represents the rate at which the first N photons are successfully detected. As expected, the coincidence rate scales as η^N. From an exponential fit, the combined source-to-detector efficiency $\eta = 43.18(7)\%$ is extracted, meaning that almost every second emission attempt generates a click in the detector. The light coloured lines are the estimated coincidence rates when correcting for losses in the optical setup. These are given by the parameter η_d. Finally, we present a comparison of our system with other existing platforms, including the best available SPDC system and single-emitter sources, such as quantum dots or Rydberg-blockaded atomic ensembles. Although the repetition rate of some of these systems is orders of magnitude higher than in our protocol, our system outperforms them in terms of real-time coincidence count rate and efficiency scaling.

The source-to-detection efficiency η can be further improved by optimising specific parts

of the setup. The intrinsic source efficiency η_s could be improved by increasing both the cooperativity C and the escape efficiency η_{esc}. For instance, reducing the cavity mode waist by a factor of two would be a feasible adjustment of the cavity geometry. This modification would result in a fourfold increase of the cooperativity, without altering the escape efficiency, thus boosting the source efficiency η_s to above 80%.

In addition to modifications of the cavity, one could optimise the detection optics. The optical path from the cavity to the detector includes two optical fibres, each causing in- and out-coupling losses. Placing the detection setup directly on the experimental table would eliminate the need for one of the fibres. Carefully choosing low-loss components on the remaining optical path would further reduce losses. We believe that with these improvements, a detection efficiency of $\eta_d = 0.85$ is attainable.

By implementing all of the above steps, the overall source-to-detection efficiency could be raised to about 70%. This number exceeds the mark of 2/3, which is an important threshold for loss-tolerance in linear optical quantum computation [74].

5. Fusion of photonic graph states

The results of this chapter have been published in Ref. [122]: P. Thomas, L. Ruscio, O. Morin, G. Rempe, **Fusion of deterministically generated photonic graph states.** *Nature* **629**, 567-572 (2024).

In the previous chapter, we have described the generation of elementary graph states of photons from a single atom used as a photon emitter. Two types of graph states were created and characterised, namely GHZ states and linear cluster states. However, a single emitter is insufficient for the generation of more complex graph states, such as 2D cluster states. To fully exploit the capabilities of these quantum emitter sources, it is necessary to combine multiple emitters and couple them using quantum logic operations. This chapter describes the first step in this direction. In our experiment, we use two atoms to independently generate elementary photonic graph states, as demonstrated in the previous chapter. We then make use of the fact that the atoms are each entangled with the photonic graph state and fuse the two states using an atom-atom entangling operation. We show that the output state satisfies the set of eigenvalue equations associated with its stabilisers and certify genuine multipartite entanglement by measuring a fidelity lower bound. In particular, we focus on two types of states, namely ring and tree graph states. Both have been recognised as important resources in the context of measurement-based quantum computation and communication [56, 57, 142].

A suitable gate operation between the emitter qubits is essential in order to generate graph states of arbitrary topology. Several mechanisms have been investigated for implementing quantum-logic gate operations between neutral atoms.

A widely used mechanism, well established in neutral atom systems, is based on the interaction mediated by the Rydberg blockade [143–145]. Recent advances have led to remarkable improvements in this technique [146–148]. Nevertheless, it remains a challenge to perform these operations in the vicinity of macroscopic objects, which often carry surface charges that perturb the highly sensitive Rydberg states. Nonetheless, moderate progress has been reported in this respect [149]. Given that in our system the atoms are trapped between two bulk mirrors with a relative distance of only 500 µm, the Rydberg-mediated quantum gate is not expected to meet our requirements.

However, the optical cavity mode itself can be used to mediate interactions between two atomic qubits. Atom-photon [150], photon-photon [151] and atom-atom [78, 152] quantum gates have been demonstrated by exploiting the normal mode splitting of the atom-cavity system in conjunction with the reflection of a photon off the optical resonator. Although this gate mechanism, known as the 'reflection mechanism', is deterministic in principle, its efficiency is limited in practice by optical losses and the use of weak coherent pulses as ancillary qubit. Along with other imperfections, these mechanisms also limit the gate fidelity, which was 74% in the case of the two-atom gate demonstrated in Ref. [152].

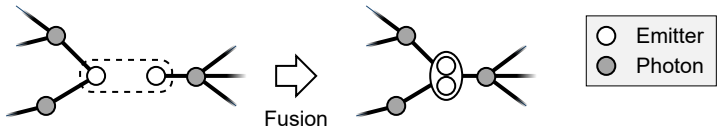

Figure 5.1.: Fusion of graph states. Two separate graphs are merged into a larger graph by application of a fusion operation [107]. In our approach, the fusion is carried out on the emitters, both of which are entangled with several photons. The bonds of each emitter vertex are preserved during the fusion process.

5.1. Photonic fusion

In light of the aforementioned considerations, we have chosen a different scheme, based on the interference of two photons emitted by the atoms. In simple terms, it can be compared to an optical Bell state measurement (BSM) based on the Hong-Ou-Mandel (HOM) effect [153]. In quantum information science, optical BSMs have become a standard tool, enabling, for example, quantum teleportation protocols [62, 154] or entanglement between distant matter qubits [77, 155–157].

Browne and Rudolph realised that the HOM-like interference of two photons could be exploited to construct cluster states [107], thereby enabling one-way quantum computation. They proposed an optical setup, consisting of polarising beam splitters, waveplates and detectors, which allows to 'fuse' vertices of different graph states. This method, known as 'fusion', represents an important innovation, as it enables universal quantum computation within the one-way model, even when using non-deterministic gate operations.

Here we extend this principle and adapt it to our cavity QED system. In this particular form, we refer to our scheme as 'cavity-assisted fusion gate'. The main difference from the original proposal is that in our approach, the cavity replaces the beam splitter as the element that enables two-photon interference. Previous cavity QED experiments have used this mechanism as an optical BSM to create ion-ion entanglement [158] and more recently as an entanglement swapping operation in a quantum repeater protocol [88]. We combine this process with the photonic graph state generation techniques established in the previous chapter. First, we demonstrate that the interference of two photons allows the preparation of a two-atom Bell state, similar to Ref. [158]. We then apply this process to two atoms, each of which is entangled with multiple photons. In this case, two multi-qubit entangled states are fused into a single larger graph state, as shown in Fig. 5.1. In comparison to the original proposal of Ref. [107], our implementation of fusion significantly reduces the required resource overhead, since certain building blocks of the graph can be created deterministically in the form of GHZ and linear cluster states [108]. Consequently, it constitutes a hybrid approach that makes use of both deterministic and non-deterministic elements.

We commence by introducing the cavity-assisted fusion gate. In its simplest form, it involves only the two emitter qubits and creates a $|\Psi^+\rangle$ Bell state at the output (Fig. 5.2a). The protocol starts by initialising both atoms in the state $|2,0\rangle$ using standard optical pumping techniques (see chapter 2.2.1). A global vSTIRAP control pulse is then applied to both atoms simultaneously, generating two photons in the cavity mode (Fig. 5.2b). The temporal intensity profile is shown in Fig. 5.2c. This process can be viewed as the generation of two atom-photon entangled pairs (Fig. 5.2d, see also chapter 2.2.5) of the form

$$|\psi_{\mathrm{AP}}\rangle = \frac{1}{\sqrt{2}} \left(|\uparrow\rangle\,|L\rangle - |\downarrow\rangle\,|R\rangle \right) , \tag{5.1}$$

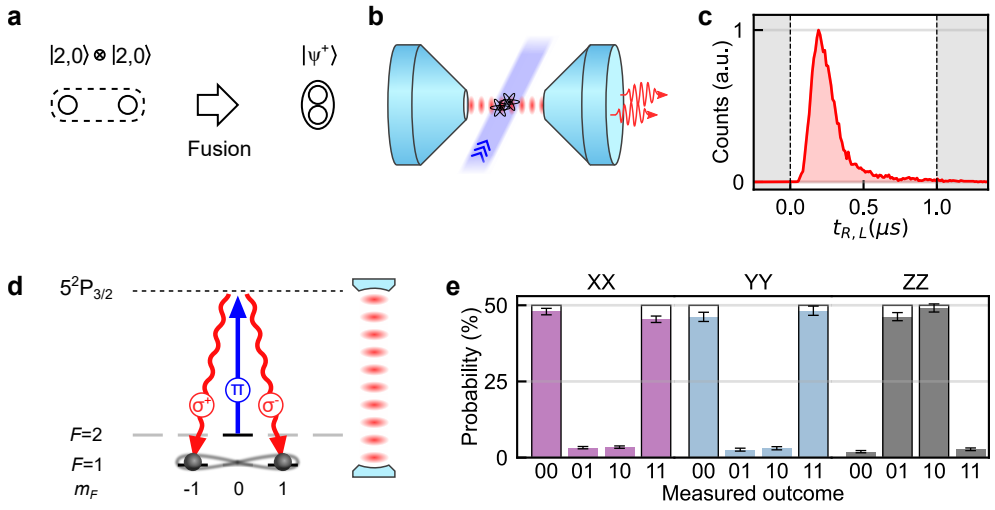

Figure 5.2.: Cavity-assisted fusion gate. (**a**) Graph state representation of the fusion process in its most elementary form. Two atoms are entangled in the $|\psi^+\rangle$ Bell state. (**b**) The two atoms are addressed by the same global vSTIRAP laser. The two photons are generated simultaneously. (**c**) Histogram showing the temporal profile of the two emitted photons. Photons that are detected outside of the dashed lines are discarded. (**d**) Illustration of the fusion in the atomic level scheme. Both atoms undergo a process equivalent to atom-photon entanglement, whereas both atoms couple to the same control laser and the cavity mode. Detecting the photons in opposite polarisation modes projects the atoms onto a Bell state. (**e**) Correlation measurement of the generated $|\psi^+\rangle$ Bell state with the detection basis pairs XX, YY and ZZ. The black frames correspond to the ideal $|\Psi^+\rangle$ state. The observed correlations certify an entanglement fidelity of 0.915(5).

where both photons are emitted into the cavity. Both photons are then measured in the Z (R/L) basis. The protocol succeeds if the photons are measured in opposite detectors, i.e. for detection outcomes RL or LR. Mathematically this corresponds to applying the projector $\langle R|\langle L|$ to the state $|\psi_{\mathrm{AP}}\rangle^{\otimes 2}$. It is easy to show that this results in the maximally entangled Bell state

$$\left|\Psi^+\right\rangle = \frac{1}{\sqrt{2}}\left(|\uparrow\downarrow\rangle + |\downarrow\uparrow\rangle\right) . \tag{5.2}$$

If both photons are instead measured in the same detector (RR or LL) the atoms are projected onto a product state ($|\uparrow\uparrow\rangle$ or $|\downarrow\downarrow\rangle$), which means that the fusion has failed.

The simultaneous emission into the cavity mode can be seen as an erasure of which-path information. In other words, it is impossible to tell, which atom emitted which photon. Therefore, the measurement of the two photons in opposite polarisation modes implements a parity measurement of the two atoms, with the outcome $\langle ZZ\rangle = -1$, without revealing any information about the state of each atom individually. Hence, the atoms are projected onto a superposition of $|\uparrow\downarrow\rangle$ and $|\downarrow\uparrow\rangle$. In the projection via the operator $\langle R|\langle L|$, it is implicitly assumed that both photons are emitted into the same spatio-temporal mode, which is indeed crucial for the quality of this process. As will become clear below, an imperfect mode overlap of the two photons leads to an incomplete erasure of which-path information and consequently to a non-unity fidelity of the fusion operation.

To show that the photons are indeed indistinguishable and that the fusion gate works as expected, we analyse the fidelity of the two-atom state with respect to the ideal state (equation 5.2). In particular, we measure correlations in terms of the Bell state stabilisers XX, YY and ZZ, where X, Y and Z are the Pauli operators. The measured data are shown in Fig. 5.2e. For each stabiliser, we plot the probability of obtaining a particular

measurement outcome (00, 01, 10 and 11). In all three measurement bases, we observe a high degree of correlation between the two atomic qubits. The fidelity can then be calculated using the formula

$$\mathcal{F} = \frac{1}{4}\left(1 + \langle XX\rangle + \langle YY\rangle - \langle ZZ\rangle\right) . \tag{5.3}$$

For the data in Fig. 5.2e, this corresponds to a fidelity of 0.915 ± 0.005. This number already includes postselection involving temporal filtering of the detection times. The criteria for postselection and how they affect the fidelity are explained below.

Postselection criteria

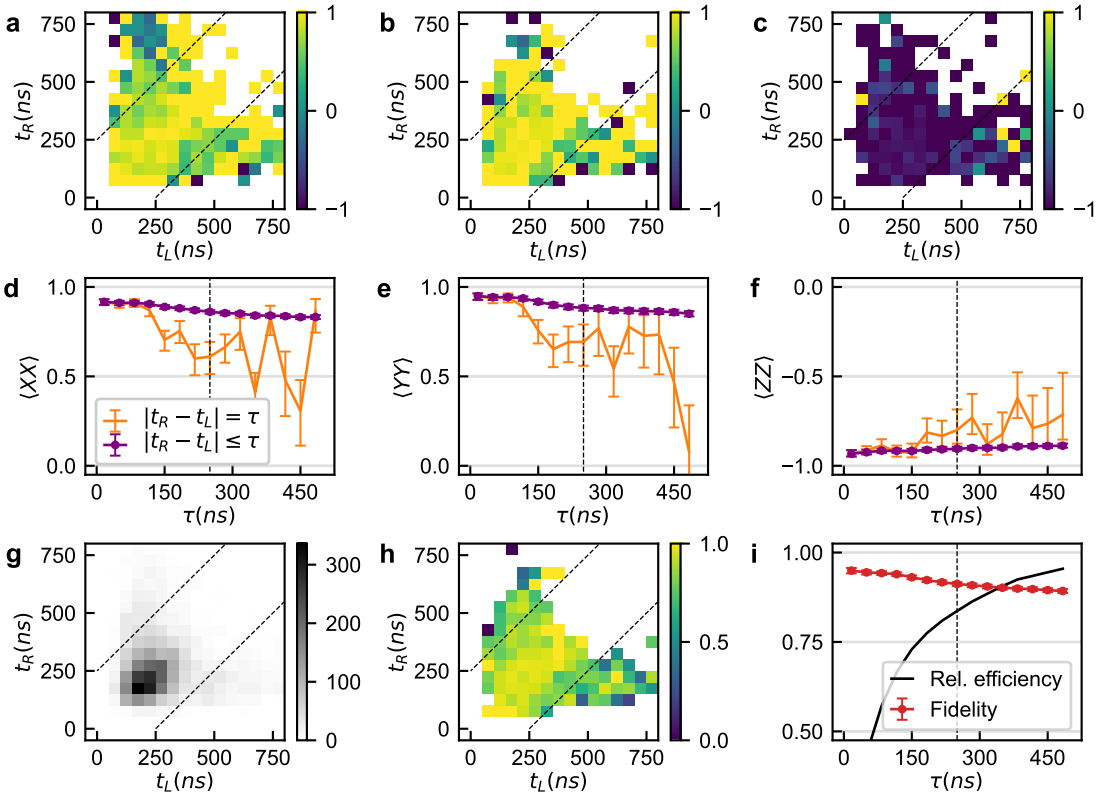

Figure 5.3.: Effect of temporal filtering on entanglement fidelity. (**a-c**) Density plot of the correlator expectation values $\langle XX\rangle$, $\langle YY\rangle$ and $\langle ZZ\rangle$ as a function of $t_{R/L}$. Pixels for which no events were recorded are shown in white. (**d-f**) Expectation values $\langle XX\rangle$, $\langle YY\rangle$ and $\langle ZZ\rangle$ as a function of detection time difference. The orange (purple) line is the respective correlator for $|t_R - t_L| = \tau$ ($|t_R - t_L| \leq \tau$), where τ is the variable on the x-axis. (**g**) Number of two-photon events as a function of t_R and t_L. Most events fall in a region close to $t_R = t_L = 200\,\text{ns}$. (**h**) Density plot of the entanglement fidelity as a function of $t_{R/L}$. (**i**) Relative efficiency and entanglement fidelity as a function of $|t_R - t_L| \leq \tau$. The relative efficiency is normalised by the number of two-photon events detected in the 1 µs acceptance interval shown in Fig. 5.2c. Black dashed lines mark the postselection criterion $|t_R - t_L| \leq 250\,\text{ns}$.

We find that the fidelity exhibits a dependence on the detection times t_R and t_L of the R and L polarised photons. The first postselection step concerns the absolute detection time $t_{R,L}$. For this, we choose an acceptance interval of 1 µs, as shown in Fig. 5.2c. About

98% of all two-photon events fall within this interval, which means that about 2% of the data is discarded in this way.

The second postselection step concerns the relative detection time. It can be observed that the fidelity decreases for larger detection time differences $|t_R - t_L|$. This can be seen in Fig. 5.3a-c, which show a density plot of the stabilisers XX, YY and ZZ as a function of t_R and t_L. For all three plots, the correlations are highest in vicinity of the diagonal, that is, when $t_R \approx t_L$. As the time difference $|t_R - t_L|$ increases, the correlations decrease substantially, especially for the XX and YY stabilisers. This appears to be the case regardless of the absolute detection times $t_{R,L}$. We therefore choose a postselection region, as marked by the dashed lines, which contains all events for which $|t_R - t_L| \leq 250$ ns.

Fig. 5.3d-f confirms this trend, displaying the correlations as a function of $|t_R - t_L| = \tau$ (orange) and $|t_R - t_L| \leq \tau$ (purple). The latter case represents the cumulative average of all events for which the two photons are detected within an interval of τ or less. Over a wide range of τ, the expectation values of the two-qubit correlators are close to the ideal case, $\langle XX \rangle = \langle YY \rangle = 1$ and $\langle ZZ \rangle = -1$. The slight decay with increasing τ indicates an imperfect indistinguishability of the photonic temporal modes. The choice of postselection criteria therefore represents a trade-off between efficiency and fidelity. Fig. 5.3g displays the density of the number of events and shows that the vast majority of the data is contained by the postselection bounds. At the same time, the fidelity derived from the individual stabiliser measurements is still reasonably high in this region, as shown in Fig. 5.3h. Finally, the trade-off between efficiency and fidelity is once again illustrated in Fig. 5.3i. The relative efficiency is defined as the ratio of two-photon events, for which $|t_R - t_L| \leq \tau$. The fidelity is the cumulative average derived from the stabiliser measurements in Fig. 5.3d-f using equation 5.3.

The results of these measurements demonstrate that the photon arrival time has a noticeable impact on the fidelity. Nevertheless, we observe that even without any postselection on the photon arrival time, the fidelity is still 0.851(6). This value already includes the effects of errors related to state preparation and readout. When choosing the rather strict criteria of $t_{R,L} \leq 500$ ns and $|t_R - t_L| \leq 20$ ns, the fidelity increases to 0.963(8). However, in this case the relative efficiency is only about 15%. For this reason, we choose the previously mentioned values of $t_{R,L} \leq 1$ µs and $|t_R - t_L| \leq 250$ ns, which result in a total postselection ratio close to 80%.

Fusion of graph states

The scenario described above is the simplest case of the fusion mechanism, in which the emitter qubits do not share a bond with any other qubit prior to the fusion (Fig. 5.2a). The resulting state $|\Psi^+\rangle$ can be interpreted as a logical qubit redundantly encoded [107] in the basis $\{|0\rangle_L \equiv |10\rangle_s, |1\rangle_L \equiv |01\rangle_s\}$. Here we write the atomic qubits in terms of the basis vectors $|0\rangle_s \equiv |\uparrow\rangle$ and $|1\rangle_s \equiv |\downarrow\rangle$, where the subscript '$s$' denotes a 'spin' qubit. As we will see below, the principle of the fusion also applies when the two atoms are part of a graph state and do share bonds with other qubits. The two emitter vertices are then merged into a single vertex, preserving the bonds attached to them, as shown in Fig. 5.1. In this case, the photon emission occurs from the atomic states $|2, \pm 2\rangle$. Since the $|2, +2\rangle$ and $|2, -2\rangle$ states couple to the R and L polarisation modes, respectively, a successful fusion corresponds to the projection onto the subspace $\{|01\rangle_s, |10\rangle_s\}$. We therefore define the fusion projection operator

$$P = |01\rangle_s \langle 01|_s + |10\rangle_s \langle 10|_s \,, \tag{5.4}$$

which describes the process mathematically.

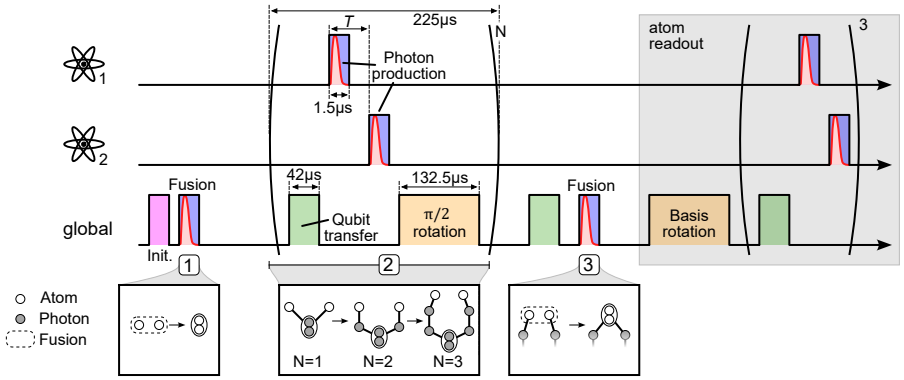

Figure 5.4.: Ring graph state protocol. Experimental sequence showing the individual steps on atom 1, atom 2 and operations performed globally, i.e. on both atoms simultaneously. The different steps include initialisation (purple), vSTIRAP (blue) and photons (red), single-qubit rotations (orange) and transfers between the hyperfine levels (green). The duration of the protocol is 1 ms for the box and 1.2 ms for the hexagon graph state. The sequence is shown below in the graph state formalism.

Note that for the emission from $|2, \pm 2\rangle$ the control laser couples to different excited states than for the $|2, 0\rangle$ state. Consequently, the photonic wave packet is slightly longer due to a larger atom-cavity detuning. To obtain the same postselection ratio of 80% as in the case of $m_F = 0$, we allow for a detection time difference $|t_R - t_L|$ of up to 400 ns, instead of 250 ns.

In the following sections, we demonstrate the concept of photonic fusion as described above. In particular, the states we generate using this principle are ring and tree graph states.

5.2. Ring graph states

We can use the two-atom Bell pair $|\Psi^+\rangle$ as a starting point to prepare different graph states. As a first example, we choose to show the generation of ring graph states, i.e. graph states with a circular topology. These have been proposed as resources for fusion-based quantum computing [159] and quantum error correction [142].

The experimental protocol is illustrated in Fig. 5.4. In the graph state picture, it can be understood as a sequence of three steps. First, we prepare the $|\Psi^+\rangle$ Bell state using the cavity-assisted fusion gate as explained above (Fig. 5.4, step 1). Next, we run N photon generation cycles on both atoms in parallel, each of which adds two photonic qubits to the graph. This results in a linear cluster state with the atoms being located at the ends of the chain (Fig. 5.4, step 2). Within each photon generation cycle, the atoms are transferred from $|1, \pm 1\rangle$ to $|2, \pm 2\rangle$ before emitting a photon via the vSTIRAP process using the single-atom addressing system. The two photons are separated in time by $T \approx 20$ µs. The parameter T serves as a degree of freedom to tune the phase of the atomic qubits with respect to each other. It is also necessary to allow enough time for the AOD to redirect the addressing beam between the first and second atom. Once both photons have been emitted, the Raman laser is used to perform a $\pi/2$ rotation on the atomic qubits. In the graph state picture, this has the effect of 'pushing out' the emitter qubits to form separate vertices. The alternating sequence of photon emission and $\pi/2$ rotation corresponds to the linear cluster state protocol described in chapter 4, executed in parallel on both atoms. In principle, the cycle can be repeated for an arbitrary number

of iterations. The number of cycles determines the size of the final ring graph state. After N cycles the protocol proceeds to the fusion step (Fig. 5.4, step 3). Here, the vertices of the emitter qubits, which form the ends of the linear cluster graph, are fused into another redundantly encoded qubit. This step transforms the one-dimensional chain into the final ring graph.

Odd vs. even parity

As mentioned above, running the sequence for a certain number of iterations determines the final size of the ring, with two vertices added per cycle. Therefore, the protocol as shown in Fig. 5.4 will always produce a graph of even parity, i.e. an even number of vertices. The protocol can be adapted to produce odd parity graphs by simply performing a local $\pi/2$ rotation immediately after the initial fusion gate (Fig. 5.4, step 1). This has the effect of pushing out one of the emitter qubits from the common vertex, which results in the dumbbell state (see chapter 3, Fig. 3.1). In our experiment, achieving local single-qubit rotations with high fidelity presents a technical challenge, primarily due to the requirement of a tight focus of the Raman beams on individual atoms. As an alternative, we perform a global $\pi/4$ rotation, which gives the same result, as shown in chapter 3.2.

Experimental results

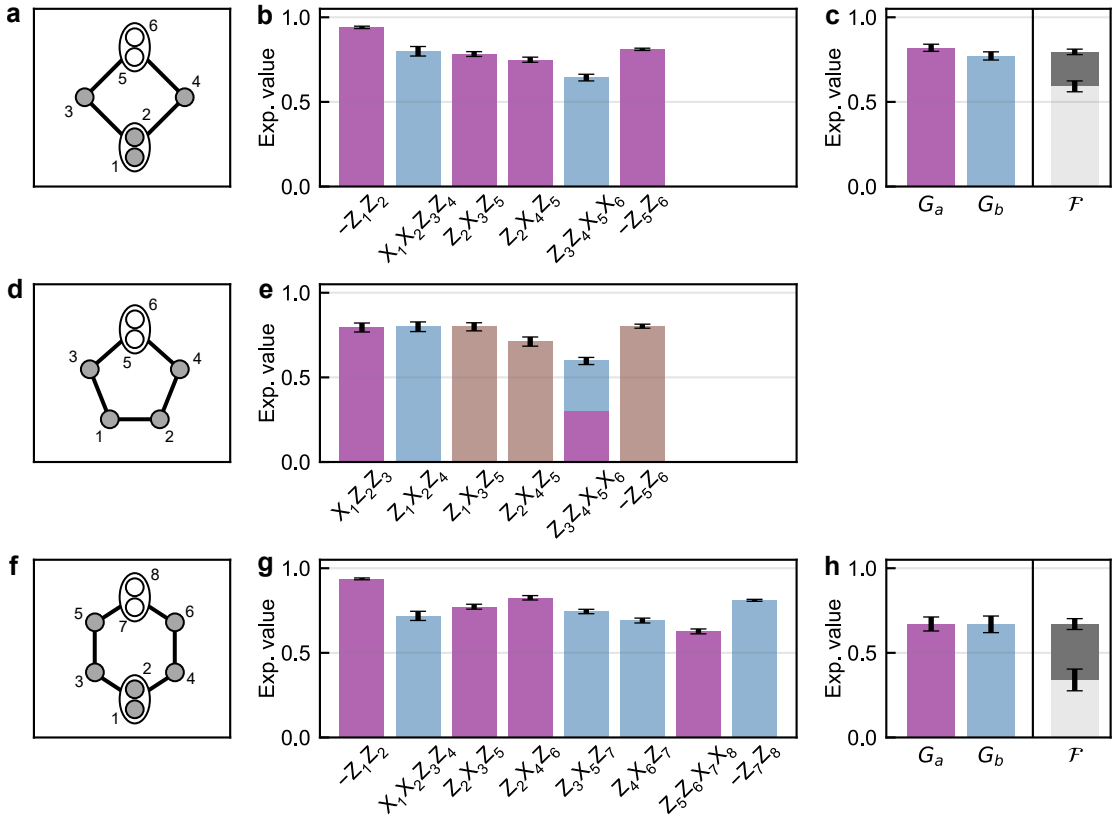

Figure 5.5.: Experimental results for ring graph states. (**a,d,f**) Graphical representation of the generated ring graph states. (**b,e,g**) Stabiliser expectation values. The colours represent the measurement settings used to obtain the stabilisers. (**c,h**) Product terms $G_{a/b}$ and fidelity constrained by the interval $\mathcal{F}_- \leq \mathcal{F} \leq \mathcal{F}_+$.

Fig. 5.5 shows the experimental results for the graph states corresponding to a box, pentagon and hexagon graph. The graphical representation of these states is displayed in panels a, d, f. The measured expectation values of their respective stabiliser operators are plotted in panels b, e, g. Overall, we observe a good agreement with the ideal state with values between 0.6 and 0.94. Note that the stabilisers associated with redundantly encoded vertices are modified compared to the standard definition. For instance, in the case of the box graph, we have $S_1 = -Z_1Z_2$, $S_2 = X_1X_2Z_3Z_4$, $S_5 = Z_3Z_4X_5X_6$ and $S_6 = -Z_5Z_6$. These differ from the standard form (equation 3.10) in that the operators X_i and Z_i are exchanged on a single index.

For the box and hexagon graphs the stabilisers are divided into two sets a and b, each of which can be measured with a single measurement setting M_a and M_b. For instance, the box graph stabilisers can be measured with the settings $M_a = Z_1Z_2X_3X_4Z_5Z_6$ and $M_b = X_1X_2Z_3Z_4X_5X_6$. Each stabiliser in Fig. 5.5b is coloured according to the measurement setting that was used to obtain it. Similar to the 1D cluster states presented in chapter 4, we can derive a lower bound $\mathcal{F}_-$ and an upper bound $\mathcal{F}_+$ for the fidelity. As before, these are defined as $\mathcal{F}_- = \langle G_a\rangle + \langle G_b\rangle - 1$ and $\mathcal{F}_+ = \sqrt{\langle G_a\rangle \langle G_b\rangle}$, with $G_{a/b} = \prod_{i\in a/b}(S_i+1)/2$.

However, due to the parity of the states (odd and even), the fidelity bounds are only defined for the box and hexagon graphs, but not for the pentagon graph. The latter requires three measurement settings, which is why we can only measure the stabiliser operators. The different measurement settings for each state are summarised in Table 5.1.

	M_a	M_b	M_c
Box	$Z_1Z_2X_3X_4Z_5Z_6$	$X_1X_2Z_3Z_4X_5X_6$	—
Pentagon	$X_1Z_2Z_3Z_4X_5X_6$	$Z_1X_2Z_3Z_4X_5X_6$	$Z_1Z_2X_3X_4Z_5Z_6$
Hexagon	$Z_1Z_2X_3X_4Z_5Z_6X_7X_8$	$X_1X_2Z_3Z_4X_5X_6Z_7Z_8$	—
Tree	$Z_1Z_2X_3Z_4Z_5X_6Z_7Z_8$	$X_1X_2Z_3X_4X_5Z_6X_7X_8$	—

Table 5.1.: Local measurement settings for ring and tree graph states. For each of the graphs shown in Fig. 5.5a,d,f and Fig. 5.8b the measurement settings (M_a, M_b and M_c) are written as a string of Pauli operators (X_i and Z_i) corresponding to the measurement of the ith qubit. The pentagon graph requires one more setting than the box, hexagon and tree graphs.

5.3. Tree graph states

As a second example, we demonstrate the generation of a tree graph state [73] consisting of eight qubits. A graph of tree topology is uniquely defined by its branching vector $\boldsymbol{b} = [b_0,...,b_m]$, which describes the connectivity between the different levels of the tree. The depth of the tree graph $d = m + 1$ is equal to the number of levels below the root qubit. By convention, the root qubit is located at the zeroth level. For illustration, the tree graph corresponding to the branching parameters $[2, 3, 2]$ is shown in Fig. 5.6.

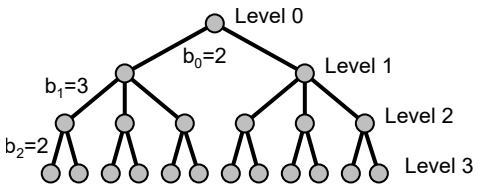

Figure 5.6: Tree states. Example tree graph with branching vector $[2, 3, 2]$.

As a simple example, consider a tree state of depth 2 with the branching vector $\boldsymbol{b} = [2,2]$.

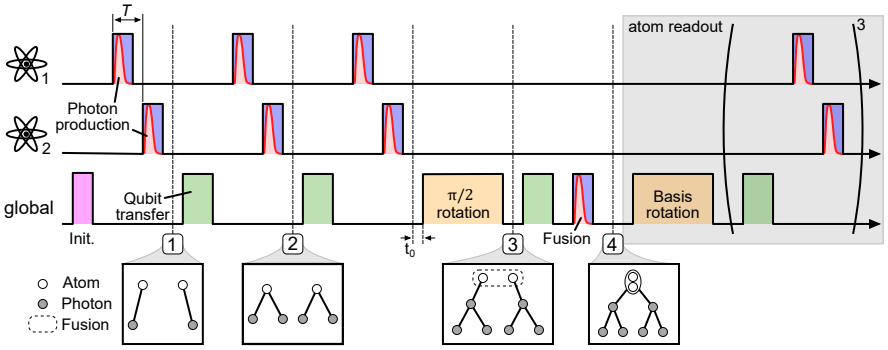

Figure 5.7.: Tree graph state protocol. Sequence of individual operations similar to Fig. 5.4. The complete protocol takes 0.8 ms. The generation process is depicted in graph state notation at the bottom of the figure.

It can be written explicitly as

$$|\psi_{\text{tree}}\rangle = \frac{1}{2\sqrt{2}}\Big(|0\rangle\left(|0++\rangle + |1--\rangle\right)^{\otimes 2} + |1\rangle\left(|0++\rangle - |1--\rangle\right)^{\otimes 2}\Big)\,, \tag{5.5}$$

which can be easily shown by applying the stabilisers to the above expression. This state can be prepared by first creating two star-shaped graphs (GHZ states) and then fusing two of their leaf qubits. The experimental implementation of this strategy is sketched in Fig. 5.7 and described in the following.

First, both atoms are initialised in the $|F = 2, m_F = 0\rangle$ state. We then generate two photons, one from each atom, by applying the vSTIRAP control pulse via the addressing system. Similar to the ring protocol, the two photons are separated in time by $T \approx 20\,\mu$s. A Hadamard gate is performed on each of the photons. Experimentally, this operation is included in the setting of the measurement basis. This results in two atom-photon entangled pairs. Their graphical representation corresponds to the dumbbell state (see Fig. 3.1). Next, two more photon generation cycles are carried out. Each cycle consists of a Raman transfer from $|1, \pm 1\rangle$ to $|2, \pm 2\rangle$ followed by a photon emission on each atom. We again apply a Hadamard gate to the photons. We also perform a Raman $\pi/2$ pulse on both atoms after a free evolution time t_0. From this we obtain the tensor product of two GHZ states, each consisting of one atom and three photons. Omitting normalisation, we write the state as

$$|\psi\rangle = \bigotimes_{j\in\{1,2\}} \Big(|+\rangle_s\,|0++\rangle + e^{-i\phi_j(t_0)}\,|-\rangle_s\,|1--\rangle\Big)\,. \tag{5.6}$$

where the subscript 's' denotes the atomic spin qubits. Each of the two product terms carries a phase factor $\phi_1(t_0) = 2\omega_L t_0$ and $\phi_2(t_0) = 2\omega_L(t_0 - T)$, which captures the free evolution of the atomic qubits. The phase terms are functions of the $\pi/2$ pulse timing parameter t_0, while $\phi_2(t_0)$ additionally depends on the photon separation T (see Fig. 5.7). The phase is actively tuned to $\phi_1(t_0) = 0$ and $\phi_2(t_0) = \pi$ by adjusting the timing parameters t_0 and T accordingly, as shown in Fig. 5.8a.

The two branches are fused into a larger graph state using the fusion gate. We do this by generating two photons using the global vSTIRAP control laser (Fig. 5.2b). As before, the detection of one photon in R and one in L corresponds to the projection of the atoms onto the subspace $\{|01\rangle_s, |10\rangle_s\}$, associated with the projector P (equation 5.4). After a

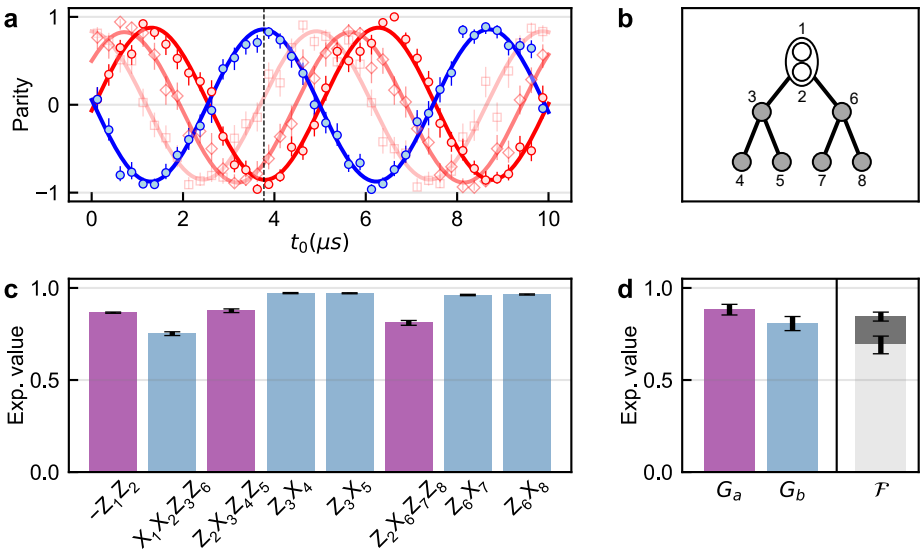

Figure 5.8.: Tree graph states. (**a**) Phase synchronisation of the two branches before the fusion. We observe oscillations of the parity as a function of the $\pi/2$ pulse timing t_0. Branch 2 (red) is tuned to have a relative phase of π with respect to branch 1 (blue). The working point is indicated by the dashed line. The phase of branch 2 shifts as T is varied (light red). (**b**) Graphical representation of the experimentally generated tree state. We choose a labelling convention as indicated by the indices next to each vertex. (**c**) Measured stabiliser expectation values. The colour of each bar corresponds to the local measurement setting M_a (purple) or M_b (blue). (**d**) Product terms G_a, G_b and fidelity. The fidelity falls within the lower and upper bounds $\mathcal{F}_-$ and $\mathcal{F}_+$ marked by the black interval.

successful fusion we have

$$\begin{aligned} P\left|\psi\right\rangle =& \left(\left|10\right\rangle_s + \left|01\right\rangle_s\right)\left|0++\right\rangle^{\otimes 2} + \left(\left|10\right\rangle_s - \left|01\right\rangle_s\right)\left|0++\right\rangle\left|1--\right\rangle \\ &+ \left(\left|10\right\rangle_s - \left|01\right\rangle_s\right)\left|1--\right\rangle\left|0++\right\rangle + \left(\left|10\right\rangle_s + \left|01\right\rangle_s\right)\left|1--\right\rangle^{\otimes 2} \\ =& \left|10\right\rangle_s\left(\left|0++\right\rangle + \left|1--\right\rangle\right)^{\otimes 2} + \left|01\right\rangle_s\left(\left|0++\right\rangle - \left|1--\right\rangle\right)^{\otimes 2}. \end{aligned} \tag{5.7}$$

For convenience we have moved the second spin qubit to the first position in the above expression, which allows us to express the two atoms as a logical qubit encoded in the basis $\{\left|0\right\rangle_L \equiv \left|10\right\rangle_s, \left|1\right\rangle_L \equiv \left|01\right\rangle_s\}$. Adding a normalisation constant, we can then write the final state as

$$\left|\psi_{\text{tree}}\right\rangle = \frac{1}{2\sqrt{2}}\left(\left|0\right\rangle_L\left(\left|0++\right\rangle + \left|1--\right\rangle\right)^{\otimes 2} + \left|1\right\rangle_L\left(\left|0++\right\rangle - \left|1--\right\rangle\right)^{\otimes 2}\right). \tag{5.8}$$

This is equivalent to the expression in equation 5.5, with the only difference that the root qubit is now redundantly encoded by the two atoms. Alternatively, it is possible to remove one of the atoms from the state by performing an X basis measurement.

In order to characterise the experimentally generated state and its overlap with the target state (equation 5.5), we determine the expectation values of the stabiliser operators. The measured data are shown in Fig. 5.8c. All eight stabilisers are above 0.7, some of them close to 1. Two measurement bases are required to obtain all the stabilisers (Table 5.1) as indicated by the colour. To measure the upper and lower bound $\mathcal{F}_+$ and $\mathcal{F}_-$ we filter the data for coincidences of all eight qubits. As before, we obtain the product correlators G_a, G_b and the fidelity interval spanned by $\mathcal{F}_+$ and $\mathcal{F}_-$ (Fig. 5.8d). The data certify genuine multipartite entanglement with $0.69^{+0.04}_{-0.05} \leq \mathcal{F} \leq 0.85^{+0.02}_{-0.03}$.

The number of coincidences, the measurement time and the resulting coincidence rate are summarised for both ring and tree graph states in Appendix D.

The one-way quantum repeater

Tree graph states serve as the fundamental resource for a quantum communication protocol known as the one-way quantum repeater [57]. Similar to the original proposal of the quantum repeater [50], the scheme involves dividing the communication link into smaller segments with repeater stations placed between them. Each station prepares a copy of the photonic resource state and uses it to encode and transmit a message qubit $\alpha|0\rangle + \beta|1\rangle$ to the next station. The strategy of encoding the information non-locally on a multiphoton entangled state is robust to some degree of optical loss between two neighbouring stations and allows the message qubit to be re-encoded on a fresh copy of the resource state. Intuitively, this concept bears some resemblance to the principle of signal amplification in classical repeaters. However, it does not involve copying the qubit in any way, as this would violate the no-cloning theorem [27]. Instead, the recovery of the qubit is made possible by the redundancy of information provided by the tree encoding.

For simplicity, consider a depth-2 tree state with branching parameters $[2, 2]$ (equation 5.5), similar to the graph shown in Fig. 5.8b. In the actual communication protocol, the root qubit of this state would be a stationary matter qubit. For the encoding step, a Bell measurement is performed between the message qubit and the root qubit of the tree state. This removes the root qubit from the tree state and at the same time teleports the message qubit onto the remaining photonic state. At the next station, the qubit can be recovered, even if some of the photons have been lost. The $[2, 2]$ tree state tolerates the loss of up to two qubits in one of the branches [57].

The probability of successfully transmitting the message qubit through a link with n repeater stations is $p_s = \eta_{\text{eff}}^{n+1}$. Here, η_{eff} is the effective probability of transmitting the message qubit from station k to station $k+1$. η_{eff} depends crucially on the topology of the resource state defined by the branching vector $\boldsymbol{b}$. For branching parameters $[b_0,...,b_m]$, the effective efficiency is given by the expression [73]

$$\eta_{\text{eff}} = [(1-\epsilon+\epsilon R_1)^{b_0} - (\epsilon R_1)^{b_0}](1-\epsilon+\epsilon R_2)^{b_1}\,, \tag{5.9}$$

where the terms R_k obey the recursive relation

$$R_k = 1 - [1-(1-\epsilon)(1-\epsilon+\epsilon R_{k+2})^{b_{k+1}}]^{b_k}\,. \tag{5.10}$$

Here $R_{m+1} = 0$, $b_{m+1} = 0$ and $\epsilon = 1-\eta$, where η is the single-photon efficiency. The parameter ϵ is simply the loss probability for a single photon between two stations (including both transmission and detection). The effective transmission probability η_{eff} is plotted in Fig. 5.9 for different branching vectors. The strategy of using single photons to encode the message qubit serves as a benchmark. Here, the effective efficiency is simply η. The tree encoding provides an advantage if η_{eff} is above this threshold. As can be seen from Fig. 5.9, trees of greater depth d tend to perform better in terms of effective efficiency. Note that for illustrative purposes, specific branching parameters have been chosen with the restriction $b_i \leq 3$. Importantly, a depth of $d = 3$ or greater is required to gain an advantage over the single-photon encoding. For larger depths, the curve shifts further to the left. However, the effective efficiency η_{eff} can never exceed the single-photon efficiency for values of $\eta < 0.5$, since this would violate the no-cloning theorem [27, 73]. This implies that the tree encoding can only provide an advantage if η is above the threshold of 0.5.

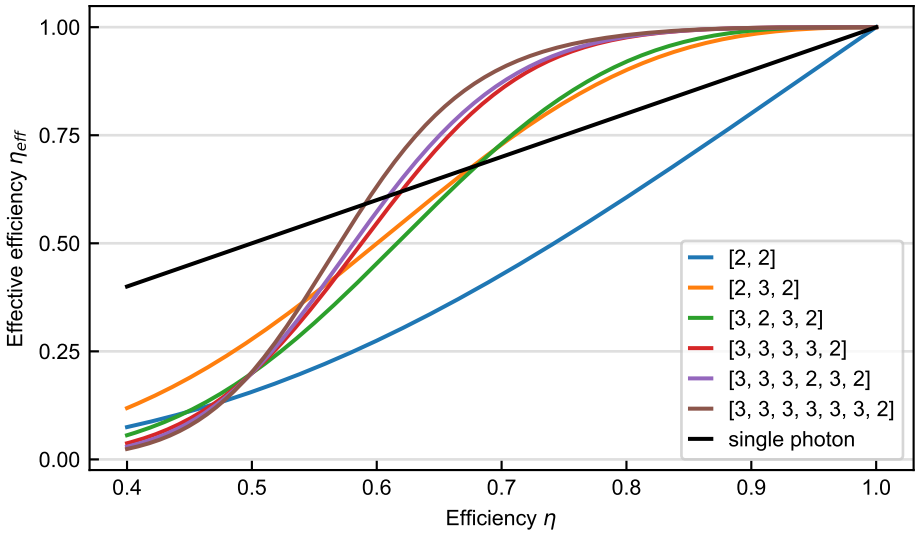

Figure 5.9.: Transmission probability of the message qubit. Effective transmission efficiency η_{eff} as a function of single-photon efficiency η. For tree states of depth $d \geq 3$, suitable branching parameters can be determined to obtain an advantage of the tree state encoding over the single-photon encoding. The branching parameters were restricted to $b_i \leq 3$.

5.4. Estimation of errors

The fidelity of the ring and tree graph states is below unity due to various experimental imperfections. Some of these imperfections can be attributed to specific steps in the protocol. For instance, we believe that the largest contribution to infidelity comes from the cavity-assisted fusion gate. In the subsequent discussion, we identify several physical mechanisms that degrade the fidelity. From this, we derive a simple model that allows us to predict the fidelity of a given graph state. We then compare the fidelity obtained from the model with the experimentally measured fidelity interval.

5.4.1. Error contributions

In chapter 4, we have already discussed some of the mechanisms that we believe are the main sources of infidelity for the elementary GHZ and linear cluster states. For these states, a single emitter was used to run a protocol composed of single-photon emissions and single-qubit rotations. The errors for these two processes were both estimated to be on the order of 1%.

For the present chapter, the situation is somewhat more complex. Here we use two emitters to execute protocols that are more sophisticated than those used previously. While the errors associated with single-photon emissions and single-qubit rotations still apply, we have to consider further mechanisms, which are discussed below.

Fusion

The central ingredient that enables experiments with multiple emitters is the cavity-assisted fusion gate. To estimate the fidelity of this process, we consider the preparation of the $|\Psi^+\rangle$ Bell state (Fig. 5.2 and 5.3). For our choice of postselection criteria, the experimentally generated state has a fidelity of 0.92. Correcting for the atomic state readout

error (about 1% per atom), we estimate the fidelity of the fusion to be 0.94 and infer an error rate of 6% per fusion operation.

Longitudinal polarisation components

In the two-emitter protocols, single-photon emissions take place using the single-atom addressing system, which involves focusing the vSTIRAP control laser down to a few micrometres. The small beam waist introduces polarisation components in the propagation direction of the laser [160]. In the atomic reference frame, these appear as σ^+/σ^- polarisation, thereby exacerbating the errors associated with imperfections in laser polarisation (see Fig. 4.11). For a beam waist of 6 µm, we estimate the additional error to be on the order of 1%.

Decoherence

Another potential source of infidelity, which was not accounted for in the single-emitter protocols (chapter 4), is decoherence. It was not considered previously because of the dynamical decoupling mechanism, which seems to mitigate the effect almost entirely. Here, the protocol was specifically designed for a single emitter with almost no free evolution time between different steps. For the ring and tree state protocol, we had to introduce some waiting time between photon emissions within a given cycle. This means that at least one of the atoms spends some extra time in the more magnetically sensitive $|2, \pm 2\rangle$ states. We therefore expect decoherence to play a larger role for ring and tree graph states than for GHZ and linear cluster states. However, it is generally a non-trivial problem to quantify the susceptibility of a given graph state to decoherence, since the error generally depends on the entanglement topology [161].

Atom positioning

Both atoms are trapped in a two-dimensional optical lattice potential. The positioning procedure is to some extent probabilistic (see chapter 2.1.4), which means that the atom pair explores a range of x- and y-positions, thus sampling a small region of the optical beams involved in the protocol. For example, the atoms experience a small shot-to-shot variation in the optical light shift. In addition, the Rabi frequency of the Raman laser varies slightly with position. Finally, the vSTIRAP addressing system actively aims along the x-direction, but does not adjust for the y-coordinate. Due to the relatively small beam waist of 6 µm, this affects the photon generation efficiency, but also the amount of circular polarisation components, as discussed above.

Drifts of optical and magnetic fields

In addition to the positional fluctuations of the atoms, the optical beams can drift, which has the same effect but occurs on much longer time scales. Similarly, the magnetic bias field is subject to certain variations over time due to changes in the laboratory environment. Drifts in both the optical and magnetic fields cause a shift in the oscillation frequency of the atomic qubit. As long as these changes occur slowly, they can be compensated for by regular retuning of the experimental sequence.

5.4.2. Error model

Accurately simulating our experimental protocols and the errors that occur within them is challenging for various reasons. First, a large Hilbert space has to be considered in a multi-particle system. Moreover, the atomic ground state consists of a total of eight sublevels, giving rise to complex dynamics, even for a single emitter qubit. Finally, modelling the evolution of graph states in the presence of noise is a non-trivial task, as some types of graph states are more susceptible to noise than others, depending on their entanglement topology [161].

We therefore choose a simplified model in which we write the density matrix as the sum of the ideal density matrix and a fully mixed state:

$$\rho_{\text{exp}} = (1 - p_{\text{noise}})\rho_{\text{ideal}} + p_{\text{noise}}\frac{\mathbb{1}}{2^n}\,. \tag{5.11}$$

Here p_{noise} is the total error probability, ρ_{ideal} is the ideal density matrix, $\mathbb{1}$ is the identity matrix and n is the number of qubits. We decompose the combined error probability p_{noise} into the different error contributions and write

$$p_{\text{noise}} = 1 - (1 - p_P)^{N_P}(1 - p_R)^{N_R}(1 - p_F)^{N_F}\,. \tag{5.12}$$

Here p_P is the probability of spontaneous scattering during photon emission, p_R the error probability for a Raman rotation, p_F the error probability for the fusion process and N_P, N_R, N_F the respective number of operations in the protocol. We only include these three steps in our model, as these are the elementary operations in our protocols. As explained previously, other mechanisms such as qubit leakage or decoherence are more difficult to incorporate because the magnitude of their effect depends on the specific protocol, making it impossible to assign an error probability to a particular step in the protocol.

In Table 5.2, we compare the fidelity obtained from our model with the experimentally measured fidelity bounds. For the box and tree graph states, the modelled fidelity $\mathcal{F}_{\text{model}}$ lies within the interval defined by $\mathcal{F}_+$ and $\mathcal{F}_-$. For the hexagon graph, $\mathcal{F}_{\text{model}}$ is slightly above the upper bound $\mathcal{F}_+$. However, considering the statistical uncertainty, our simple model is still consistent with the experimental data. It is also important to note that the model does not include effects such as decoherence and qubit leakage, which could explain the slight discrepancy observed.

	Box	Pentagon	Hexagon	Tree
N_P	6	6	8	8
N_R	6	8	8	4
N_F	2	2	2	2
$\mathcal{F}_+$	0.80 ± 0.02	-	0.67 ± 0.03	$0.85^{+0.02}_{-0.03}$
$\mathcal{F}_{\text{model}}$	0.74	0.73	0.69	0.77
$\mathcal{F}_-$	0.59 ± 0.03	-	$0.34^{+0.06}_{-0.07}$	$0.69^{+0.04}_{-0.05}$

Table 5.2.: Comparison between our theoretical model and the experimental data. We compare the predicted fidelities obtained from the model with the measured upper and lower bounds of the fidelity. We use the following error probabilities as input to the model: $p_P = 0.02$, $p_R = 0.01$ and $p_F = 0.06$.

6. Conclusion and outlook

In recent years, entangled graph states have emerged as versatile tools and promising candidates for a variety of applications in quantum information science, including computing, communication and sensing. The experiments performed in this thesis address the experimental challenge of generating photonic graph states of various types.

To achieve this goal, we first used a single rubidium atom in an optical cavity to sequentially emit photons via the vSTIRAP process. In combination with single-qubit Raman rotations on the atomic qubit, this enabled us to generate GHZ and linear cluster states. Our experiments demonstrated GHZ state entanglement of up to 14 photons, the largest state of entangled photons produced to date. The fidelity of the state decreased by only 1% per additional photon. The measured data for linear cluster states demonstrated genuine multipartite entanglement of up to 12 qubits. For the largest states of 14 photons (GHZ states) and 12 photons (linear cluster states) the generation rate was on the order of one event per minute, substantially faster than for previous implementations.

In the second part, we used two atoms in the optical cavity. We first studied the photonic fusion mechanism used to entangle the two atomic qubits. In the fusion process the atoms simultaneously emit a photon into the cavity, erasing the which-path information. Measuring the photons in opposite detectors then projects the atoms into the $|\Psi^+\rangle$ Bell state. We then combined the emission capability of each atom with the photonic fusion to merge two separate graph states into one larger one. We measured the stabiliser operators of ring and tree graph states of up to 8 qubits. For two instances of these, namely the box graph and the tree graph, our measurement additionally confirmed genuine multipartite entanglement.

Scalability and future improvements

In the future, different pathways could be explored in order to develop the presented method further. The main challenge lies in incorporating more emitter qubits into the scheme. One approach is to increase the number of emitters within the same cavity and couple them through fusion, as realised for two atoms in chapter 5. The most promising way to achieve this is to utilise optical tweezers, which has matured into a powerful technology for accurately controlling large arrays of atoms [146, 148, 162]. Alternatively, the individual atom-cavity systems could be organised in a distributed architecture connected by optical links, as illustrated in Fig. 6.1.

The efficiency of hardware usage is the main advantage of the first approach over the second. Placing the emitters in one cavity is more cost-effective and potentially more scalable than the distributed arrangement. The ability to increase the number of emitters is primarily limited by the available laser power. While the finite cavity mode volume may present an obstacle, this issue could be mitigated by the use of movable arrays of optical tweezers [146, 148]. The distributed architecture offers superior addressability of the individual emitters hosted by separate setups. Local gate operations and readout can be performed essentially without crosstalk, circumventing a frequent problem for most quantum devices, including the proposed one-cavity architecture. Considering both strengths

and weaknesses of the two approaches, a hybrid approach combining the two is also a viable option.

In both of the previously discussed scenarios there are different options concerning the two-qubit logic operations between the emitter qubits. We will here group these options into the probabilistic fusion, based on two-photon interference, and unitary two-qubit gates. The fusion mechanism was demonstrated in chapter 5 for two atoms in one cavity. The same concept could be applied to emitters in separate cavities, where the photons are simply overlapped on a beam splitter. Arguably the biggest disadvantage of the fusion mechanism is its probabilistic nature, succeeding only 50% of the time. A deterministic unitary two-qubit gate would therefore provide a substantial scaling advantage.

One way to realise such a gate is the remote quantum-logic gate based on the reflection of an ancillary photon (see Fig. 6.1). Our group has demonstrated such protocols both for two atomic qubits in the same cavity [152] and more recently in separate cavities [78]. These protocols are in principle deterministic, assuming the absence of loss of the ancillary photon. However, in practice the detection of the latter heralds the success of the protocol. The efficiency is therefore limited by optical losses. Moreover, in our implementations the ancillary photon was generated from faint laser pulses. Keeping the mean photon number of these pulses low was necessary to suppress the multiphoton components, resulting in a further decrease in efficiency. The fusion mechanism, although probabilistic, represented the overall better compromise for our experimental setting.

Another possibility, which we have not yet explored in our cavity experiments, is the use of quantum gates based on Rydberg-Rydberg interactions. These have been demonstrated with high fidelities for atoms in optical tweezer arrays [147]. However, transposing this technique to atomic cavity QED faces a significant obstacle due to the strong susceptibility of Rydberg states to electric fields. We expect that the surface charges on the substrates of the cavity mirrors strongly disturbs the quantum state during the Rydberg gate protocol. Nevertheless, some progress has been made in addressing this issue [149].

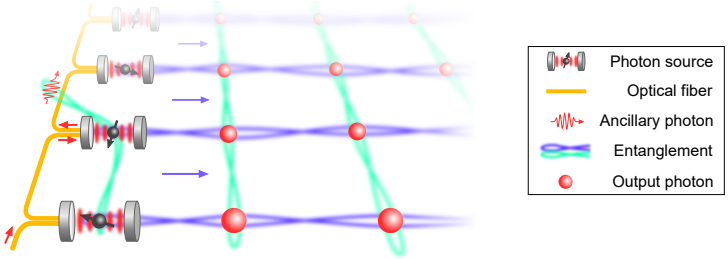

Figure 6.1.: Envisioned architecture for photonic graph state generation. Several atom-cavity systems are connected by an optical channel, through which two-qubit quantum logic is implemented using an ancillary photon [78]. Each atom emits a string of photons in a 1D cluster state. CZ gates are executed on neighbouring pairs of emitters in between photon emissions. This weaves the 1D chains into a 2D cluster state of photons, serving as a resource for one-way quantum computing [54]. Figure adapted from Ref. [124].

Applications

The perspective of scaling up to a larger number of emitters, as previously discussed, opens the door to harnessing graph state entanglement in a number of different applications. Amongst these, one-way quantum computation and other MBQC protocols belong to the

quantum technology proposals that currently attract the most attention. The primary challenge towards this goal is the generation of a 2D cluster state. Several theoretical works have already outlined how this can be achieved with quantum dots [67, 163–165]. As demonstrated in this thesis, this concept also applies to other types of emitters, like atoms in cavities. Once the generation of a 2D cluster state becomes feasible, we can use it to implement elementary computational algorithms, similar to experiments based on SPDC [59, 60, 166], trapped ions [167] or superconducting qubits [168].

An interesting perspective on this path is the realisation of adaptive measurements and active feedforward, making the computation deterministic. Such computations have been demonstrated with SPDC-based sources [169], but the parallel preparation of the photonic resource state requires very fast electronic and optical operations to carry out the feedforward. In emitter-based schemes, the photon emission occurs sequentially, which significantly relaxes the time-scale at which these operations have to be executed. The adaptive setting of the detection basis can then be achieved with a polarisation EOM, similar to the ones used in our detection setup (chapter 2.1.6).

Quantum communication using graph states, such as repeater graph states [55, 56] or tree graph states [57, 73], presents another fascinating direction to explore. Tree graph states, for instance, have been demonstrated in chapter 5 using the fusion mechanism. In our experiments we have produced a small tree state of depth 2, that is two layers in addition to the root qubit. In principle, this state allows to collectively encode a logical qubit on the entire multi-qubit state. Subsequently, one could show that the encoded qubit can withstand the loss of certain subsets of physical qubits. The ultimate goal is to demonstrate an advantage of this method compared to simply encoding a qubit on a single photon. A tree of depth 3 would be sufficient to achieve this, given that the source-to-detector efficiency surpasses a certain threshold.

A. List of abbreviations

AC alternating current. 27

AOD acousto-optic deflector. 13, 14, 66

AOM acousto-optic modulator. 21

BSM Bell state measurement. 37, 38

cavity QED cavity quantum electrodynamics. 3, 5, 7, 10, 11, 58, 62, 76

CZ gate controlled Z gate. 33, 37, 76

DDS direct digital synthesizer. 21

EMCCD electron-multiplying charge-coupled device. 13, 14

EOM electro-optic modulator. 15, 16, 21, 22, 24, 42, 53, 57, 77

FF feedforward. 27–30

MBQC measurement-based quantum computation. 3, 4, 36, 76

MOT magneto-optical trap. 3, 7, 11

MW microwave. 21

NPBS non-polarising beam splitter. 13, 24

PBS polarising beam splitter. 14, 15, 21, 42

PD photodiode. 13

QIP quantum information processing. 2, 3, 7, 18, 36

QKD quantum key distribution. 2, 3

QST quantum state tomography. 38, 39

RF radio frequency. 14, 21

RGS repeater graph state. 37, 38

SNSPD superconducting nanowire single-photon detector. 15, 42

SPDC spontaneous parametric down-conversion. 4, 41, 51, 57, 58, 77

SQL standard quantum limit. 50, 51

STIRAP stimulated Raman adiabatic passage. 19

TTL transistor-transistor logic. 14

vSTIRAP vacuum-stimulated Raman adiabatic passage. 8, 18–20, 24–26, 42, 43, 53, 54, 56, 57, 62, 63, 66, 69, 73, 75

B. GHZ/linear cluster protocol

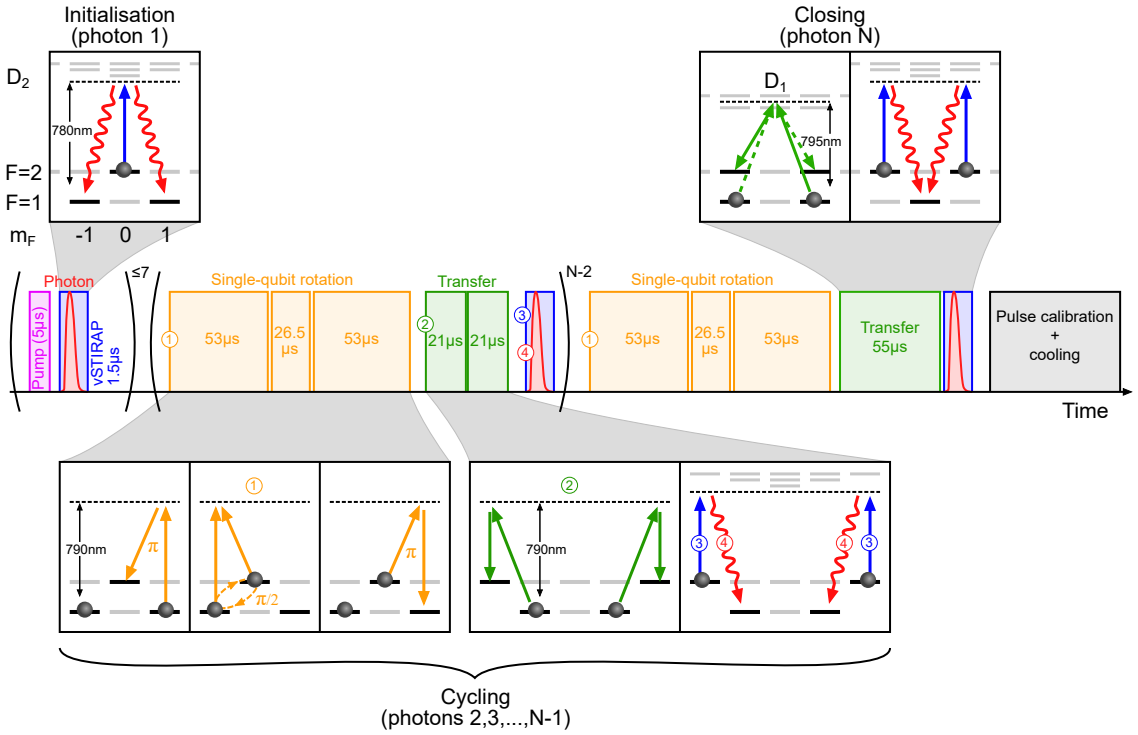

Figure B.1.: Detailed protocol for GHZ and linear cluster state generation. The individual steps shown correspond to the protocol as described in chapter 4.1. The initialisation step, consisting of optical pumping and photon production, is repeated until success for a maximum of seven attempts. The cycling steps (1-4) are carried out for $N-2$ cycles. The protocol ends with the Nth photon being generated in the closing step. Afterwards, the experiment proceeds with pulse calibration and cooling. If at any point a photon generation attempt fails and we do not obtain a detection events from the detector, the protocol ends prematurely and goes directly to pulse calibration and cooling.

C. Box graph state protocol

In the following we will use the box graph state as an example to gain a more thorough understanding of the generation protocol. This includes a derivation of explicit expressions of the multi-qubit state at different stages of the protocol.

In step 1 we use the fusion gate to obtain

$$\left|\Psi^{+}\right\rangle = \frac{1}{\sqrt{2}}\left(|01\rangle_s + |10\rangle_s\right) . \tag{C.1}$$

Next, we perform a Raman transfer from $|1, \pm 1\rangle$ to $|2, \pm 2\rangle$ and generate a photon. We then have a state consisting of two atoms and two photons of the form

$$|0\rangle_s |01\rangle |1\rangle_s + |1\rangle_s |10\rangle |0\rangle_s , \tag{C.2}$$

where for simplicity we omit the normalisation constant. As for the atomic qubits, we have written the photonic qubit in the computational basis defined by $|0\rangle \equiv |R\rangle$ and $|1\rangle \equiv |L\rangle$. We then apply a Raman $\pi/2$ pulse to both atomic qubits and get

$$|+\rangle_s |01\rangle |-\rangle_s + |-\rangle_s |10\rangle |+\rangle_s \tag{C.3}$$

The protocol proceeds with the second cycle. Here, were first apply a Z rotation to both emitters before generating a photon to get

$$\begin{aligned} &\Big(|0\rangle_s |0\rangle - |1\rangle_s |1\rangle\Big) |01\rangle \Big(|0\rangle |0\rangle_s + |1\rangle |1\rangle_s\Big) \\ +&\Big(|0\rangle_s |0\rangle + |1\rangle_s |1\rangle\Big) |10\rangle \Big(|0\rangle |0\rangle_s - |1\rangle |1\rangle_s\Big) , \end{aligned} \tag{C.4}$$

followed by a Raman $\pi/2$ pulse

$$\begin{aligned} &\Big(|+\rangle_s |0\rangle - |-\rangle_s |1\rangle\Big) |01\rangle \Big(|0\rangle |+\rangle_s + |1\rangle |-\rangle_s\Big) \\ +&\Big(|+\rangle_s |0\rangle + |-\rangle_s |1\rangle\Big) |10\rangle \Big(|0\rangle |+\rangle_s - |1\rangle |-\rangle_s\Big) . \end{aligned} \tag{C.5}$$

Up to a local Z gate on qubit 5, the above expression is equivalent to a 5-qubit linear cluster state with qubits 3 and 4 forming a redundantly encoded qubit. We then perform the fusion operation on the two emitters. This corresponds to applying the fusion projector P_F (equation 5.4) to the expression above.

$$\begin{aligned} \longrightarrow &|0\rangle_s \Big(|0010\rangle - |0011\rangle - |1010\rangle + |1011\rangle + |0100\rangle + |0101\rangle + |1100\rangle + |1101\rangle\Big) |1\rangle_s \\ &+ |1\rangle_s \Big(|0010\rangle + |0011\rangle + |1010\rangle + |1011\rangle + |0100\rangle - |0101\rangle - |1100\rangle + |1101\rangle\Big) |0\rangle_s , \end{aligned} \tag{C.6}$$

With some simple transformations using $|\pm\rangle = |0\rangle \pm |1\rangle$ we obtain

$$|0\rangle_s \left(|-01-\rangle + |+10+\rangle\right) |1\rangle_s + |1\rangle_s \left(|+01+\rangle + |-10-\rangle\right) |0\rangle_s . \tag{C.7}$$

Finally, we reorder the qubits to be consistent with the graph shown in Fig. 5.5a and get

$$|\psi_{\text{box}}\rangle = \Big(|01--\rangle |10++\rangle\Big) |01\rangle_s + \Big(|01++\rangle + |10--\rangle\Big) |10\rangle_s \tag{C.8}$$

D. Coincidence rate for ring and tree graph states

	Box	Pentagon	Hexagon	Tree
Number of events	628	392	219	227
Measurement time (h)	4.5	3.3	8.7	4.8
Rate (events/min)	2.3	2.0	0.4	0.8

Table D.1.: Coincidence rate. Number of events, measurement time and the resulting coincidence rate for the box, pentagon, hexagon and tree graph states presented in chapter 5.

Bibliography

[1] Max Planck, Ueber das Gesetz der Energieverteilung im Normalspectrum. *Annalen der Physik* **309**, 553–563 (1901).

[2] A. Einstein, Über einen die Erzeugung und Verwandlung des Lichtes betreffenden heuristischen Gesichtspunkt. *Annalen der Physik* **322**, 132–148 (1905).

[3] N. Bohr, I. On the constitution of atoms and molecules. *The London, Edinburgh, and Dublin Philosophical Magazine and Journal of Science* **26**, 1–25 (1913).

[4] Louis De Broglie, Recherches sur la théorie des Quanta. *Annales de Physique* **10**, 22–128 (1925).

[5] E. Schrödinger, An Undulatory Theory of the Mechanics of Atoms and Molecules. *Phys. Rev.* **28**, 1049–1070 (1926).

[6] A. Einstein, B. Podolsky, and N. Rosen, Can Quantum-Mechanical Description of Physical Reality Be Considered Complete? *Phys. Rev.* **47**, 777–780 (1935).

[7] J. S. Bell, On the Einstein Podolsky Rosen paradox. *Physics Physique Fizika* **1**, 195–200 (1964).

[8] Stuart J. Freedman and John F. Clauser, Experimental Test of Local Hidden-Variable Theories. *Phys. Rev. Lett.* **28**, 938–941 (1972).

[9] Alain Aspect, Philippe Grangier, and Gérard Roger, Experimental Tests of Realistic Local Theories via Bell's Theorem. *Phys. Rev. Lett.* **47**, 460–463 (1981).

[10] Alain Aspect, Philippe Grangier, and Gérard Roger, Experimental Realization of Einstein-Podolsky-Rosen-Bohm Gedankenexperiment: A New Violation of Bell's Inequalities. *Phys. Rev. Lett.* **49**, 91–94 (1982).

[11] Alain Aspect, Jean Dalibard, and Gérard Roger, Experimental Test of Bell's Inequalities Using Time-Varying Analyzers. *Phys. Rev. Lett.* **49**, 1804–1807 (1982).

[12] Gregor Weihs et al., Violation of Bell's Inequality under Strict Einstein Locality Conditions. *Phys. Rev. Lett.* **81**, 5039–5043 (1998).

[13] M. A. Rowe et al., Experimental violation of a Bell's inequality with efficient detection. *Nature* **409**, 791–794 (2001).

[14] W. Tittel et al., Violation of Bell Inequalities by Photons More Than 10 km Apart. *Phys. Rev. Lett.* **81**, 3563–3566 (1998).

[15] B. Hensen et al., Loophole-free Bell inequality violation using electron spins separated by 1.3 kilometres. *Nature* **526**, 682–686 (2015).

[16] Marissa Giustina et al., Significant-Loophole-Free Test of Bell's Theorem with Entangled Photons. *Phys. Rev. Lett.* **115**, 250401 (2015).

[17] Lynden K. Shalm et al., Strong Loophole-Free Test of Local Realism. *Phys. Rev. Lett.* **115**, 250402 (2015).

[18] Wenjamin Rosenfeld et al., Event-Ready Bell Test Using Entangled Atoms Simultaneously Closing Detection and Locality Loopholes. *Phys. Rev. Lett.* **119**, 010402 (2017).

[19] Ming-Han Li et al., Test of Local Realism into the Past without Detection and Locality Loopholes. *Phys. Rev. Lett.* **121**, 080404 (2018).

[20] Simon Storz et al., Loophole-free Bell inequality violation with superconducting circuits. *Nature* **617**, 265–270 (2023).

[21] Richard P. Feynman, Simulating physics with computers. *International Journal of Theoretical Physics* **21**, 467–488 (1982).

[22] David Deutsch and Richard Jozsa, *Proceedings of the Royal Society of London. Series A: Mathematical and Physical Sciences* **439**, 553–558 (1992).

[23] P.W. Shor. "Algorithms for quantum computation: discrete logarithms and factoring". In: *Proceedings 35th Annual Symposium on Foundations of Computer Science*. SFCS-94. IEEE Comput. Soc. Press. DOI: 10.1109/sfcs.1994.365700. URL: http://dx.doi.org/10.1109/SFCS.1994.365700.

[24] Peter W. Shor, Polynomial-Time Algorithms for Prime Factorization and Discrete Logarithms on a Quantum Computer. *SIAM Journal on Computing* **26**, 1484–1509 (1997).

[25] Lov K. Grover. "A fast quantum mechanical algorithm for database search". In: *Proceedings of the twenty-eighth annual ACM symposium on Theory of computing - STOC '96*. STOC '96. ACM Press, 1996. DOI: 10.1145/237814.237866. URL: http://dx.doi.org/10.1145/237814.237866.

[26] Charles H. Bennett and Gilles Brassard, Quantum cryptography: Public key distribution and coin tossing. *Theoretical Computer Science* **560**, 7–11 (2014).

[27] W. K. Wootters and W. H. Zurek, A single quantum cannot be cloned. *Nature* **299**, 802–803 (1982).

[28] Artur K. Ekert, Quantum cryptography based on Bell's theorem. *Phys. Rev. Lett.* **67**, 661–663 (1991).

[29] W. Neuhauser et al., Localized visible Ba^+ mono-ion oscillator. *Phys. Rev. A* **22**, 1137–1140 (1980).

[30] D.J. Wineland and Wayne M. Itano, Spectroscopy of a single Mg+ ion. *Physics Letters A* **82**, 75–78 (1981).

[31] Claude N. Cohen-Tannoudji, Nobel Lecture: Manipulating atoms with photons. *Rev. Mod. Phys.* **70**, 707–719 (1998).

[32] Steven Chu, Nobel Lecture: The manipulation of neutral particles. *Rev. Mod. Phys.* **70**, 685–706 (1998).

[33] William D. Phillips, Nobel Lecture: Laser cooling and trapping of neutral atoms. *Rev. Mod. Phys.* **70**, 721–741 (1998).

[34] Harold J. Metcalf and Peter van der Straten. *Laser Cooling and Trapping*. Springer New York, 1999. ISBN: 9781461214700. DOI: 10.1007/978-1-4612-1470-0. URL: http://dx.doi.org/10.1007/978-1-4612-1470-0.

[35] D. M. Meekhof et al., Generation of Nonclassical Motional States of a Trapped Atom. *Phys. Rev. Lett.* **76**, 1796–1799 (1996).

[36] David J. Wineland, Nobel Lecture: Superposition, entanglement, and raising Schrödinger's cat. *Rev. Mod. Phys.* **85**, 1103–1114 (2013).

[37] Serge Haroche, Nobel Lecture: Controlling photons in a box and exploring the quantum to classical boundary. *Rev. Mod. Phys.* **85**, 1083–1102 (2013).

[38] M. Brune et al., Realization of a two-photon maser oscillator. *Phys. Rev. Lett.* **59**, 1899–1902 (1987).

[39] M. Brune et al., Quantum Rabi Oscillation: A Direct Test of Field Quantization in a Cavity. *Phys. Rev. Lett.* **76**, 1800–1803 (1996).

[40] D. Meschede, H. Walther, and G. Müller, One-Atom Maser. *Phys. Rev. Lett.* **54**, 551–554 (1985).

[41] Gerhard Rempe, Herbert Walther, and Norbert Klein, Observation of quantum collapse and revival in a one-atom maser. *Phys. Rev. Lett.* **58**, 353–356 (1987).

[42] R. J. Thompson, G. Rempe, and H. J. Kimble, Observation of normal-mode splitting for an atom in an optical cavity. *Phys. Rev. Lett.* **68**, 1132–1135 (1992).

[43] J. Ye, D. W. Vernooy, and H. J. Kimble, Trapping of Single Atoms in Cavity QED. *Phys. Rev. Lett.* **83**, 4987–4990 (1999).

[44] P. W. H. Pinkse et al., Trapping an atom with single photons. *Nature* **404**, 365–368 (2000).

[45] J. McKeever et al., State-Insensitive Cooling and Trapping of Single Atoms in an Optical Cavity. *Phys. Rev. Lett.* **90**, 133602 (2003).

[46] P. Maunz et al., Cavity cooling of a single atom. *Nature* **428**, 50–52 (2004).

[47] P. Maunz et al., Normal-Mode Spectroscopy of a Single-Bound-Atom–Cavity System. *Phys. Rev. Lett.* **94**, 033002 (2005).

[48] J. I. Cirac and P. Zoller, Quantum Computations with Cold Trapped Ions. *Phys. Rev. Lett.* **74**, 4091–4094 (1995).

[49] Anders Sørensen and Klaus Mølmer, Quantum Computation with Ions in Thermal Motion. *Phys. Rev. Lett.* **82**, 1971–1974 (1999).

[50] H.-J. Briegel et al., Quantum Repeaters: The Role of Imperfect Local Operations in Quantum Communication. *Phys. Rev. Lett.* **81**, 5932–5935 (1998).

[51] H. J. Kimble, The quantum internet. *Nature* **453**, 1023–1030 (2008).

[52] Hein M. et al., Entanglement in graph states and its applications. *Proceedings of the International School of Physics "Enrico Fermi"* **162**, 115–218 (2006).

[53] Hans J. Briegel and Robert Raussendorf, Persistent Entanglement in Arrays of Interacting Particles. *Phys. Rev. Lett.* **86**, 910–913 (2001).

[54] Robert Raussendorf and Hans J. Briegel, A One-Way Quantum Computer. *Phys. Rev. Lett.* **86**, 5188–5191 (2001).

[55] Koji Azuma, Kiyoshi Tamaki, and Hoi-Kwong Lo, All-photonic quantum repeaters. *Nature Communications* **6**, (2015).

[56] Donovan Buterakos, Edwin Barnes, and Sophia E. Economou, Deterministic Generation of All-Photonic Quantum Repeaters from Solid-State Emitters. *Phys. Rev. X* **7**, 041023 (2017).

[57] Johannes Borregaard et al., One-Way Quantum Repeater Based on Near-Deterministic Photon-Emitter Interfaces. *Phys. Rev. X* **10**, 021071 (2020).

[58] Chao Zhang et al., Spontaneous Parametric Down-Conversion Sources for Multiphoton Experiments. *Advanced Quantum Technologies* **4**, (2021).

[59] P. Walther et al., Experimental one-way quantum computing. *Nature* **434**, 169–176 (2005).

[60] Xing-Can Yao et al., Experimental demonstration of topological error correction. *Nature* **482**, 489–494 (2012).

[61] Jian-Wei Pan et al., Experimental test of quantum nonlocality in three-photon Greenberger–Horne–Zeilinger entanglement. *Nature* **403**, 515–519 (2000).

[62] Dik Bouwmeester et al., Experimental quantum teleportation. *Nature* **390**, 575–579 (1997).

[63] Han-Sen Zhong et al., 12-Photon Entanglement and Scalable Scattershot Boson Sampling with Optimal Entangled-Photon Pairs from Parametric Down-Conversion. *Phys. Rev. Lett.* **121**, 250505 (2018).

[64] Rupert Ursin et al., Quantum teleportation across the Danube. *Nature* **430**, 849–849 (2004).

[65] C. Schön and et al., Sequential generation of entangled multiqubit states. *Phys. Rev. Lett.* **95**, 110503 (2005).

[66] T. Wilk. "Quantum interface between an atom and a photon". TUM/MPQ thesis. 2008. URL: http://mediatum.ub.tum.de/node?id=637078.

[67] N. H. Lindner and T. Rudolph, Proposal for pulsed on-demand sources of photonic cluster state strings. *Phys. Rev. Lett.* **103**, 113602 (2009).

[68] I. Schwartz et al., Deterministic generation of a cluster state of entangled photons. *Science* **354**, 434–437 (2016).

[69] Natasha Tomm et al., A bright and fast source of coherent single photons. *Nature Nanotechnology* **16**, 399–403 (2021).

[70] O. Morin et al., Deterministic Shaping and Reshaping of Single-Photon Temporal Wave Functions. *Phys. Rev. Lett.* **123**, 133602 (2019).

[71] J. Schupp et al., Interface between Trapped-Ion Qubits and Traveling Photons with Close-to-Optimal Efficiency. *PRX Quantum* **2**, 020331 (2021).

[72] Xing Ding et al., High-efficiency single-photon source above the loss-tolerant threshold for efficient linear optical quantum computing. (2023).

[73] Michael Varnava, Daniel E. Browne, and Terry Rudolph, Loss Tolerance in One-Way Quantum Computation via Counterfactual Error Correction. *Phys. Rev. Lett.* **97**, 120501 (2006).

[74] Michael Varnava, Daniel E. Browne, and Terry Rudolph, How Good Must Single Photon Sources and Detectors Be for Efficient Linear Optical Quantum Computation? *Phys. Rev. Lett.* **100**, 060502 (2008).

[75] S. D. Barrett and T. M. Stace, Fault tolerant quantum computation with very high threshold for loss errors. *Physical Review Letters* **105**, 200502 (2010).

[76] Jörg Bochmann. "Coherent Dynamics and State Detection of Single Atoms in a Cavity". PhD thesis. Max-Planck-Institut für Quantenoptik/Technische Universität München, 2010. URL: http://mediatum.ub.tum.de/node?id=981224.

[77] Stephan Ritter et al., An elementary quantum network of single atoms in optical cavities. *Nature* **484**, 195–200 (2012).

[78] Severin Daiss et al., A quantum-logic gate between distant quantum-network modules. *Science* **371**, 614–617 (2021).

[79] M. H. Anderson et al., Observation of Bose-Einstein Condensation in a Dilute Atomic Vapor. *Science* **269**, 198–201 (1995).

[80] Andreas Neuzner. "Resonance Fluorescence of an Atom Pair in an Optical Resonator". PhD thesis. Max-Planck-Institut für Quantenoptik/Technische Universität München, 2018. URL: http://mediatum.ub.tum.de/node?id=1286880.

[81] A. Reiserer and G. Rempe, Cavity-based quantum networks with single atoms and optical photons. *Rev. Mod. Phys.* **87**, 1379 (2015).

[82] R. W. P. Drever et al., Laser phase and frequency stabilization using an optical resonator. *Applied Physics B Photophysics and Laser Chemistry* **31**, 97–105 (1983).

[83] J. Dalibard and C. Cohen-Tannoudji, Laser cooling below the Doppler limit by polarization gradients: simple theoretical models. *Journal of the Optical Society of America B* **6**, 2023 (1989).

[84] André Kochanke. "A High Resolution Optical System for Imaging and Addressing of Single Atoms". MA thesis. Max-Planck-Institut für Quantenoptik/Ludwig-Maximilians-Universität, München, 2012.

[85] Stefan Langenfeld. "Quantum Communication with a Two-Atoms Network Node". PhD thesis. Max-Planck-Institut für Quantenoptik/Technische Universität München, 2021. URL: http://mediatum.ub.tum.de/node?id=1584276.

[86] Alfred Kastler, Quelques suggestions concernant la production optique et la détection optique d'une inégalité de population des niveaux de quantifigation spatiale des atomes. Application à l'expérience de Stern et Gerlach et à la résonance magnétique. *Journal de Physique et le Radium* **11**, 255–265 (1950).

[87] William Happer, Optical Pumping. *Rev. Mod. Phys.* **44**, 169–249 (1972).

[88] S. Langenfeld et al., Quantum Repeater Node Demonstrating Unconditionally Secure Key Distribution. *Phys. Rev. Lett.* **126**, 230506 (2021).

[89] Pascale Senellart, Glenn Solomon, and Andrew White, High-performance semiconductor quantum-dot single-photon sources. *Nature Nanotechnology* **12**, 1026–1039 (2017).

[90] Edward Mills Purcell, Spontaneous Emission Probabilities at Radio Frequencies. *Phys. Rev.* **69**, 681 (1946).

[91] P. Goy et al., Observation of Cavity-Enhanced Single-Atom Spontaneous Emission. *Phys. Rev. Lett.* **50**, 1903–1906 (1983).

[92] D. J. Heinzen et al., Enhanced and inhibited visible spontaneous emission by atoms in a confocal resonator. *Phys. Rev. Lett.* **58**, 1320–1323 (1987).

[93] Alexey V. Gorshkov et al., Universal Approach to Optimal Photon Storage in Atomic Media. *Phys. Rev. Lett.* **98**, 123601 (2007).

[94] M. Fleischhauer and M. D. Lukin, Dark-State Polaritons in Electromagnetically Induced Transparency. *Phys. Rev. Lett.* **84**, 5094–5097 (2000).

[95] M. Fleischhauer, S.F. Yelin, and M.D. Lukin, How to trap photons? Storing single-photon quantum states in collective atomic excitations. *Optics Communications* **179**, 395–410 (2000).

[96] A. E. Kozhekin, K. Mølmer, and E. Polzik, Quantum memory for light. *Phys. Rev. A* **62**, 033809 (2000).

[97] S. A. Moiseev and S. Kröll, Complete Reconstruction of the Quantum State of a Single-Photon Wave Packet Absorbed by a Doppler-Broadened Transition. *Phys. Rev. Lett.* **87**, 173601 (2001).

[98] Alexey V. Gorshkov et al., Photon storage in Λ-type optically dense atomic media. I. Cavity model. *Phys. Rev. A* **76**, 033804 (2007).

[99] Luigi Giannelli et al., Optimal storage of a single photon by a single intra-cavity atom. *New Journal of Physics* **20**, 105009 (2018).

[100] Jerome Dilley et al., Single-photon absorption in coupled atom-cavity systems. *Phys. Rev. A* **85**, 023834 (2012).

[101] Matthias Körber. "Long-lived and Efficient Qubit Memory for Photonic Quantum Networks". PhD thesis. Max-Planck-Institut für Quantenoptik/Technische Universität München, 2020. URL: http://mediatum.ub.tum.de/node?id=1544910.

[102] Martin Mücke et al., Generation of single photons from an atom-cavity system. *Phys. Rev. A* **87**, 063805 (2013).

[103] Matthias Kreis. "Magnetfeldstabilisierung für Hochpräzise Einzelatom Spektroskopie". PhD thesis. Universität des Saarlandes, 2014.

[104] Michael A. Nielsen and Isaac L. Chuang. *Quantum Computation and Quantum Information: 10th Anniversary Edition*. Cambridge University Press, 2012. ISBN: 9780511976667. DOI: 10.1017/cbo9780511976667. URL: http://dx.doi.org/10.1017/CBO9780511976667.

[105] D. M. Greenberger, M. A. Horne, and A. Zeilinger. "Bell's Theorem, Quantum Theory, and Conceptions of the Universe". In: ed. by M. Kafatos. Kluwer Academic, 1989, pp. 73–76.

[106] Daniel Gottesman, Class of quantum error-correcting codes saturating the quantum Hamming bound. *Phys. Rev. A* **54**, 1862–1868 (1996).

[107] Daniel E. Browne and Terry Rudolph, Resource-Efficient Linear Optical Quantum Computation. *Phys. Rev. Lett.* **95**, 010501 (2005).

[108] Paul Hilaire et al., Near-deterministic hybrid generation of arbitrary photonic graph states using a single quantum emitter and linear optics. *Quantum* **7**, 992 (2023).

[109] H. J. Briegel et al., Measurement-based quantum computation. *Nature Physics* **5**, 19–26 (2009).

[110] M. Zwerger, H. J. Briegel, and W. Dür, Measurement-based quantum communication. *Applied Physics B* **122**, (2016).

[111] Koji Azuma et al., Quantum repeaters: From quantum networks to the quantum internet. *Rev. Mod. Phys.* **95**, 045006 (2023).

[112] Daniel Gottesman and Isaac L. Chuang, Demonstrating the viability of universal quantum computation using teleportation and single-qubit operations. *Nature* **402**, 390–393 (1999).

[113] David Elieser Deutsch, Quantum computational networks. *Proceedings of the Royal Society of London. A. Mathematical and Physical Sciences* **425**, 73–90 (1989).

[114] Adriano Barenco et al., Elementary gates for quantum computation. *Phys. Rev. A* **52**, 3457–3467 (1995).

[115] Michał Horodecki, Paweł Horodecki, and Ryszard Horodecki, Separability of mixed states: necessary and sufficient conditions. *Physics Letters A* **223**, 1–8 (1996).

[116] Dagmar Bruß et al., Reflections upon separability and distillability. *Journal of Modern Optics* **49**, 1399–1418 (2002).

[117] Barbara M. Terhal, Bell inequalities and the separability criterion. *Physics Letters A* **271**, 319–326 (2000).

[118] M. Lewenstein et al., Optimization of entanglement witnesses. *Phys. Rev. A* **62**, 052310 (2000).

[119] Géza Tóth and Otfried Gühne, Entanglement detection in the stabilizer formalism. *Phys. Rev. A* **72**, 022340 (2005).

[120] Géza Tóth and Otfried Gühne, Detecting Genuine Multipartite Entanglement with Two Local Measurements. *Phys. Rev. Lett.* **94**, 060501 (2005).

[121] Otfried Gühne and Géza Tóth, Entanglement detection. *Physics Reports* **474**, 1–75 (2009).

[122] Philip Thomas et al., Fusion of deterministically generated photonic graph states. *Nature* **629**, 567–572 (2024).

[123] M. Hein, J. Eisert, and H. J. Briegel, Multiparty entanglement in graph states. *Phys. Rev. A* **69**, 062311 (2004).

[124] Philip Thomas et al., Efficient generation of entangled multiphoton graph states from a single atom. *Nature* **608**, 677–681 (2022).

[125] D. Istrati et al., Sequential generation of linear cluster states from a single photon emitter. *Nature Communications* **11**, (2020).

[126] Dan Cogan et al., Deterministic generation of indistinguishable photons in a cluster state. *Nature Photonics* **17**, 324–329 (2023).

[127] N. Coste et al., High-rate entanglement between a semiconductor spin and indistinguishable photons. *Nature Photonics* **17**, 582–587 (2023).

[128] Chao-Wei Yang et al., Sequential generation of multiphoton entanglement with a Rydberg superatom. *Nature Photonics* **16**, 658–661 (2022).

[129] Otfried Gühne et al., Toolbox for entanglement detection and fidelity estimation. *Phys. Rev. A* **76**, 030305 (2007).

[130] Vittorio Giovannetti, Seth Lloyd, and Lorenzo Maccone, Advances in quantum metrology. *Nature Photonics* **5**, 222–229 (2011).

[131] A. Buikema et al., Sensitivity and performance of the Advanced LIGO detectors in the third observing run. *Phys. Rev. D* **102**, 062003 (2020).

[132] Hwang Lee, Pieter Kok, and Jonathan P. Dowling, A quantum Rosetta stone for interferometry. *Journal of Modern Optics* **49**, 2325–2338 (2002).

[133] J. J . Bollinger et al., Optimal frequency measurements with maximally correlated states. *Phys. Rev. A* **54**, R4649–R4652 (1996).

[134] Géza Tóth and Iagoba Apellaniz, Quantum metrology from a quantum information science perspective. *Journal of Physics A: Mathematical and Theoretical* **47**, 424006 (2014).

[135] K. J. Resch et al., Time-Reversal and Super-Resolving Phase Measurements. *Phys. Rev. Lett.* **98**, 223601 (2007).

[136] Tomohisa Nagata et al., Beating the Standard Quantum Limit with Four-Entangled Photons. *Science* **316**, 726–729 (2007).

[137] M. W. Mitchell, J. S. Lundeen, and A. M. Steinberg, Super-resolving phase measurements with a multiphoton entangled state. *Nature* **429**, 161–164 (2004).

[138] Sergei Slussarenko et al., Unconditional violation of the shot-noise limit in photonic quantum metrology. *Nature Photonics* **11**, 700–703 (2017).

[139] G. Peniakov et al., Towards supersensitive optical phase measurement using a deterministic source of entangled multiphoton states. *Physical Review B* **101**, (2020).

[140] Konstantin Tiurev and Anders S. Sørensen, Fidelity measurement of a multiqubit cluster state with minimal effort. *Phys. Rev. Res.* **4**, 033162 (2022).

[141] Steven T. Flammia and Yi-Kai Liu, Direct Fidelity Estimation from Few Pauli Measurements. *Phys. Rev. Lett.* **106**, 230501 (2011).

[142] Thomas J. Bell, Love A. Pettersson, and Stefano Paesani, Optimizing Graph Codes for Measurement-Based Loss Tolerance. *PRX Quantum* **4**, 020328 (2023).

[143] D. Jaksch et al., Fast Quantum Gates for Neutral Atoms. *Phys. Rev. Lett.* **85**, 2208–2211 (2000).

[144] Harry Levine et al., Parallel Implementation of High-Fidelity Multiqubit Gates with Neutral Atoms. *Phys. Rev. Lett.* **123**, 170503 (2019).

[145] E. Urban et al., Observation of Rydberg blockade between two atoms. *Nature Physics* **5**, 110–114 (2009).

[146] Dolev Bluvstein et al., A quantum processor based on coherent transport of entangled atom arrays. *Nature* **604**, 451–456 (2022).

[147] Simon J. Evered et al., High-fidelity parallel entangling gates on a neutral-atom quantum computer. *Nature* **622**, 268–272 (2023).

[148] Dolev Bluvstein et al., Logical quantum processor based on reconfigurable atom arrays. *Nature* **626**, 58–65 (2023).

[149] Paloma L. Ocola et al., Control and Entanglement of Individual Rydberg Atoms Near a Nanoscale Device. arXiv:2210.12879v1 (2022).

[150] Andreas Reiserer et al., A quantum gate between a flying optical photon and a single trapped atom. *Nature* **508**, 237–240 (2014).

[151] Bastian Hacker et al., A photon–photon quantum gate based on a single atom in an optical resonator. *Nature* **536**, 193–196 (2016).

[152] Stephan Welte et al., Photon-Mediated Quantum Gate between Two Neutral Atoms in an Optical Cavity. *Phys. Rev. X* **8**, 011018 (2018).

[153] C. K. Hong, Z. Y. Ou, and L. Mandel, Measurement of subpicosecond time intervals between two photons by interference. *Phys. Rev. Lett.* **59**, 2044–2046 (1987).

[154] D. Boschi et al., Experimental Realization of Teleporting an Unknown Pure Quantum State via Dual Classical and Einstein-Podolsky-Rosen Channels. *Phys. Rev. Lett.* **80**, 1121–1125 (1998).

[155] D. L. Moehring et al., Entanglement of single-atom quantum bits at a distance. *Nature* **449**, 68–71 (2007).

[156] Julian Hofmann et al., Heralded Entanglement Between Widely Separated Atoms. *Science* **337**, 72–75 (2012).

[157] H. Bernien et al., Heralded entanglement between solid-state qubits separated by three metres. *Nature* **497**, 86–90 (2013).

[158] B. Casabone et al., Heralded Entanglement of Two Ions in an Optical Cavity. *Phys. Rev. Lett.* **111**, 100505 (2013).

[159] Sara Bartolucci et al., Fusion-based quantum computation. *Nature Communications* **14**, (2023).

[160] Derya Taray. "Towards Increasing Atomic Coherence Times with a Standing Wave Dipole Trap". MA thesis. Ludwig-Maximilians-Universität, München, 2020. URL: https://xqp.physik.uni-muenchen.de/publications/files/theses_master/master_taray1.pdf.

[161] W. Dür and H.-J. Briegel, Stability of Macroscopic Entanglement under Decoherence. *Phys. Rev. Lett.* **92**, 180403 (2004).

[162] Daniel Barredo et al., An atom-by-atom assembler of defect-free arbitrary two-dimensional atomic arrays. *Science* **354**, 1021–1023 (2016).

[163] Sophia E. Economou, Netanel Lindner, and Terry Rudolph, Optically Generated 2-Dimensional Photonic Cluster State from Coupled Quantum Dots. *Phys. Rev. Lett.* **105**, 093601 (2010).

[164] Mercedes Gimeno-Segovia, Terry Rudolph, and Sophia E. Economou, Deterministic Generation of Large-Scale Entangled Photonic Cluster State from Interacting Solid State Emitters. *Phys. Rev. Lett.* **123**, 070501 (2019).

[165] Antonio Russo, Edwin Barnes, and Sophia E Economou, Generation of arbitrary all-photonic graph states from quantum emitters. *New Journal of Physics* **21**, 055002 (2019).

[166] Stefanie Barz et al., Demonstration of Blind Quantum Computing. *Science* **335**, 303–308 (2012).

[167] B. P. Lanyon et al., Measurement-Based Quantum Computation with Trapped Ions. *Phys. Rev. Lett.* **111**, 210501 (2013).

[168] F. Albarrán-Arriagada et al., One-way quantum computing in superconducting circuits. *Phys. Rev. A* **97**, 032320 (2018).

[169] Robert Prevedel et al., High-speed linear optics quantum computing using active feed-forward. *Nature* **445**, 65–69 (2007).

Acknowledgements

The completion of this PhD thesis marks a personal milestone, one that could not have been achieved without the guidance, support, and encouragement of numerous individuals, both within and outside of our fantastic group.

First and foremost, I owe my profound gratitude to my supervisor, Gerhard Rempe, whose expertise has been the foundation of my academic journey. While his guidance provided direction, he also gave our team the freedom to explore unknown territory. This allowed enough room for my curiosity to flourish, ultimately resulting in what I am immensely proud to present as the fruit of my research endeavours.

I am equally indebted to the members of the Pistol team, with whom I spent countless hours in the lab. When I started working in the group, I was fortunate to be mentored by my senior PhD student Stefan Langenfeld, who has passed on a wealth of knowledge to me. My gratitude also extends to my colleagues Olivier Morin and Leonardo Ruscio. I am extremely proud of what we have achieved as a team. Additionally, I would like to thank all former members of the Pistol experiment, whose contributions ensured the reliability of the apparatus I had the pleasure to work with.

I am also grateful to our twin experiment, the QGates, for the connection experiments we have carried out together. Our collaboration was been extremely fruitful and an invaluable experience for me. My thanks go to Stephan Welte, Emanuele Distante, Severin Daiß, Lukas Hartung and Bastian Hacker.

Operating the complex machines in our lab would not have been possible without the support from our technicians. Many thanks to Tobias Urban, Florian Furchtsam, Johannes Siegl and Thomas Wiesmeier! For their indispensable support outside the lab, I would like to thank our assistants Iris Anneser and Annika Scherer, as well as all the administrative staff of our institute.

Last but not least, I would like to thank my family. I am especially grateful to my parents for their constant support throughout my studies. I also thank my brother Max for proofreading this thesis and providing valuable input. Finally, I would like to express my deepest gratitude to my partner Tuuli for her unwavering support during rough times.